PHOTOMETRIC AND INTERFEROMETRIC INVESTIGATIONS OF THE THERMOSPHERE IN MID-LATITUDE

（測光器および干渉分光計を用いた中緯度における熱圏の研究）

by

SHOICHI OKANO

A dissertation submitted in partial fulfillment of
the requirements for the degree of
DOCTOR OF SCIENCE
TOHOKU UNIVERSITY

1986

Acknowledgement

I wish to express heartfelt thanks to Professor Hiroshi Oya for his guidance and advice throughout the preparation of this dissertation, and to Professor J. S. Kim of the State University of New York at Albany for his encouragement throughout this research. I also extend my deep gratitude to Professor T. Ichikawa of the Asahi University for his assistance in constructing the instrument.

Special thanks are due to Professor D. A. Graham of the State University College at Plattsburgh, who participated in the collection of the data presented in Chapter 9.

TABLE OF CONTENTS

List of Figures

List of Tables

CHAPTER I

Introduction

Thermosphere

The earth's thermosphere is the region of the upper atmosphere above the mesopause (80-90 km) where the neutral gas temperature begins a steep increase with height. The temperature may reach values as high as 2000° K in the isothermal regime above 200 km. The upper boundary of the thermosphere is customarily associated with the exobase (500-600 km), where the tenuous particle population becomes collisionless. The most important energy source on a global scale for the thermosphere above 150 km is heating due to the absorption of the extreme ultraviolet (EUV) radiation from the sun, which is highly dependent on solar activity [e.g., Roble and Dickinson, 1973; Torr et al., 1980 a, b].

The thermosphere also receives solar energy through the magnetosphere in the form of heating by precipitating particles and the heating due to Joule dissipation of electric fields. The local heating rate due to this energy input, which is highly structured both spatially and temporally, is at times comparable to or even exceeds that from solar EUV absorption. The energy input at high latitudes in this form is the source of auroral processes and causes profound perturbations in the thermosphere. Intensification of magnetospheric convection at high latitudes during periods of geomagnetic disturbances causes the expansion of the auroral oval to lower latitudes as auroral activity increases.

The mid-latitude thermosphere thus comes under the influence of the large energy input that generally occurs at high latitude. When intense aurora occurs at high latitude, the thermospheric perturbations extend even to low latitudes and finally cause global redistribution of dynamic properties of the thermosphere.

Geomagnetic Storm Effects

It was already suggested in early studies of auroral phenomena and of ionospheric perturbations that the neutral thermosphere might be heated during geomagnetic storms [e.g., Petersen, 1927; Appleton and Ingram, 1935; Kirby et al., 1935; Chapman, 1937]. However, direct evidence was only obtained many years later when Jacchia [1959] detected magnetic storm-associated changes in the orbital decay rate of artificial satellites. Since then, magnetic storm-associated perturbations of the thermosphere remain one of the most challenging subjects of aeronomy. This is because these perturbations not only have a significant influence on the global morphology of the upper atmoshpere, but also constitute an important link in the complex chain of solar-terrestrial relations, since the energy is ultimately supplied by the solar wind.

Geomagnetic storm-associated perturbations of the thermosphere at F-region heights have been investigated using a variety of techniques. From the observational side, the methods include ground based optical and incoherent scatter radar measurements; direct and remote satellite measurements of winds, temperature, and composition; and indirect measurements from inferences of measured ionospheric properties.

As observational knowledge was accumulated, theoretical studies have also been developed to create and improve various empirical or numerical models of the thermosphere. However, we are still far from a comprehensive understanding of the problem. A recent review of this subject is given by Roble [1983].

There are two other possible mechanisms of energy flow into the thermosphere from the magnetosphere which take place at mid-latitudes during a period of geomagnetic storms. One is the precipitation of energetic O^+ ions. Observations of energetic O^+ fluxes at mid-latitudes have been reported during several magnetic storms [Shelley et al., 1972, 1974; Sharp et al., 1974, 1976 a, b]. The atmospheric effects to be expected from the precipitation of these fluxes were investigated by Torr et al. [1974], and Torr and Torr [1979]. According to these sources the fast O^+ ion produces fast O atoms (peak production at 500 km altitude) through charge exchange and momentum transfer, yielding atomic oxygen emissions of 630.0 nm that may be as bright as 200 R. Recently, Torr et al. [1982] reported a refined study of the dynamic response of the thermosphere to the energy influx resulting from energetic O^+ ions. The results of a time-dependent calculation by Torr et al. [1982] showed that heating due to precipitating energetic O^+ ions produces a significant perturbation to the thermospheric structure above about 300 km. In addition, Yee et al. [1980] reported the existence of an atomic oxygen corona overlying the thermosphere during the solar maximum period, from a series of twilight interferometric observations of the near infrared $O^+(^2P)$ doublets at 732 and 733 nm.

They detected excessive amounts of emission at shadow heights above 550 km and the scale height deduced from the vertical brightness profile showed a marked increase above 550 km, estimating the equivalent temperature as being 4000° K or higher.

It is apparent from these reports that nonthermal O atoms exist in the 500 km altitude region. However, ground-based observations of these non-thermal O atoms have not yet been reported in the literature.

SAR Arcs

The other form of energy coupling between the magnetosphere and the thermosphere is manifested as a distinct optical phenomenon; that is the stable auroral red arc (SAR arc). Numerous observations of the SAR arcs spanning more than two decades after the initial report of their existence by Barbier [1958] have provided the characteristic properties of the phenomena. They include (a) nearly monochromatic emission at 630.0 nm [$O(^1D)$]; (b) occurrence predominantly within the latitude interval $2 \lesssim L \lesssim 4$ [Marovich and Roach, 1963; Roach and Roach, 1963; Hoch and Smith, 1971], and at rather hight altitude (~400 km) [Roach and Roach, 1963; Tohmatsu and Roach, 1962]; (c) wide longitudinal extent, at laeast over the entire night-side of the earth, along nearly the same L shell [Roach and Roach, 1963; Craven et al., 1982]; and (d) occurrence during periods of large geomagnetic storms [Rees and Roble, 1975]. Rees and Akasofu [1963] found that SAR arc intensities have strong positive correlation with the D_{st} index. This finding directed attention to the ring current as the likely energy source for maintenance of the arcs. On the other hand, observations made from satellites revealed that the SAR arc is generally located in L value near

the position of the plasmapause [Carpenter, 1971; Chappell et al., 1971].

To explain these observed SAR arc properties, Cole [1965] originally suggested a heat conduction model in which energy transferred from energetic ring current ions to plasmaspheric electrons at the equatorial region through Coulomb collisions is conducted downward along geomagnetic field lines in the form of heat in the electron gas. The electron temperatures at ionospheric altitudes are in turn enhanced so that the preferential excitation of atomic oxygen to the ^1D state (excitation threshold is 1.96 eV) by electrons in the high energy tail of a Maxwellian energy distribution takes place. Later, Cornwall et al. [1971] proposed another energy transfer mechanism which relies on generation of ion cyclotron waves at the equatorial plasmapause-ring current interaction region followed by absorption of the wave energy by plasmaspheric electrons via Landau damping. Another approach was madeby Hasegawa and Mima [1978]. They suggested that the production of kinetic Alfvén waves at the plasmapause followed by precipitation of suprathermal electrons is capable of generating the SAR arc. It still appears that the actual physical process(es) responsible for the production and maintenance of the SAR arc has (have) yet to be firmly established (e.g., see Gurgiolo et al. [1982]). Good reviews on all aspects of SAR arcs have been presented by Roach and Roach [1963], Nagy et al. [1970], Hoch [1973], and Rees and Roble [1975].

Objectives and Outline of the Dissertation

Thermospheric response to the above-mentioned energy couplings between the magnetosphere and the thermosphere can be monitored from the ground by optical means during periods of geomagnetic distrubances. One of

most useful methods is the measurement of thermospheric temperatures and winds by a high resolution Fabry-Perot interferometer. The neutral gas temperature at F-region heights (~250 km) can be determined from the Doppler broadened line profiles of the oxygen 630.0 nm emission in the aurora and airglow. This technique has been widely used for more than two decades. A good review on the application of high resolution Fabry-Perot interferometers to the study of the upper atmosphere is presented by Hernandez and Roble [1979].

Locations at mid-latitudes are suitable for optical observations from the ground for studies of the thermosphere during periods of geomagnetic disturbance, because the heating effect caused by auroral processes is expected to reach this region and the precipitation of energetic O^+ ions and the SAR arcs are supposed to appear overhead.

The author of the present study had an opportunity to carry out such observations at Albany, New York (geographic latitude 42.68° N, longitude 286.18° E; geomagnetic latitude 54.3°) from May 1978 through September 1979. This period, which was very close to the maximum of solar cycle 21, was favorable to make SAR arc observations since the occurrence frequency of the arcs follows the solar activity. During the preceding year, efforts were concentrated on constructing and testing the instrument: a 15-cm aperture high resolution Fabry-Perot interferometer which utilizes a multiple zone aperture for increasing the throughput.

The line of logic of this dissertation consists as follows. The description of instrumentation and the method used for determination of the neutral gas temperature is given in Chapter 2; it is followed by the

observational results divided into two parts.

In Part I, the focus of the study is placed on the thermospheric temperature response to heating associated with geomagnetic disturbances. The temperatures measured during geomagnetically quiet periods are shown in Chapter 3 as a basis for reference to heating effects. In Chapter 4, a typical temperature response of the thermosphere which was obtained during a period in which an isolated substorm occurred is presented. The temperatures obtained during five geomagnetically disturbed periods are given in Chapter 5 and the observed heating effects are discussed in terms of the longitudinal location of the most intense portion of the auroral electrojet current. Significant temperature enhancement obtained during the July 5, 1978 storm period suggested the possible existence of the nonthermal atomic oxygen due to the precipitation of energetic O^+ ions and the results are presented in Chapter 6.

Part II is concentrated on observational results of the SAR arcs. Chapter 7 presents the observed temperature enhancement within an SAR arc. In Chapter 8, close correlation between the intensity of a SAR arc and that of the westward auroral electrojet, which was determined from magnetograms obtained from stations along a geomagnetic meridian close to the site of optical observation, is given. A remarkable coincidence of the onset of a SAR arc and that of an isolated substorm, which has not been reported hitherto, is shown in Chapter 9. In Chapter 10, satellite measurements of the soft electron flux during an SAR arc event are given.

Finally, the conclusions drawn through these observational results are summarized in Chapter 11.

CHAPTER II

Instrumentation and Method of Analysis

As has been described in the previous chapter, the Fabry-Perot (F.P.) interferometer is a very useful tool for remote measurements of temperatures and winds in the upper atmosphere through emission lines in the airglow and aurora. However, the primary difficulty in those studies where the line emission is quite low is that the available signal is extremely feeble, even with the rather large throughput of the F.P. interferometer, thereby requiring long integration times. The one feasible method for increasing the throughput is the use of the multiple zone aperture (MZA) through which passes the radiation of successive interference fringes, while the conventional pin-hole aperture utilizes only a portion of the radiation constituting the central fringe. To date few studies with such an MZA have been reported [Meaburn, 1968; Biondi et al., 1985].

In this chapter, the design of an MZA with optimized aperture width for Doppler temperature measurements is given first along with a discussion on the effects caused by its imperfections.

A 15-cm Fabry-Perot interferometer which utilizes an MZA has been constructed and tested. A successful experimental result will be described. Description of a multicolor meridian-scanning photmeter which was used for photometric measurements in the present research is given also in this chapter. The analysis method used for determination of Doppler temperatures from an observed interferometric fringe follows the description of instrumentation.

Design of Zone Aperture

Let us now consider the case in which radiation having the wavenumber σ_0 gives a fringe peak on the optical axis. If the fringe peak of the same order appears at the angle χ due to radiation of wavenumber σ, the order of interference is given by

$$n = 2\mu t\sigma_0 = 2\mu t\sigma\cos\chi \qquad (2\text{-}1)$$

where μ is the index of refraction of the gas between the etalon plates and t is the etalon spacing.

It is possible to increase the solid angle subtended by the sky, hence the throughput, by inserting a liquid having high refractive index μ [Meaburn, 1968]. In such a case, χ should be replaced by arcsin $(\sin\phi/\mu)$, where ϕ is an extreme angle of field of view on the sky. However, this effect can be neglected for a conventional gas-spaced etalon. Therefore, the difference in wavenumber $2f = \sigma-\sigma_0$ can be related to the geometry by th following equation:

$$f = \frac{1}{2}\left(\frac{n}{2\mu t\cos\chi} - \frac{n}{2\mu t}\right)$$

$$= \frac{\sigma_0}{2}\left(\frac{1}{\cos\chi} - 1\right) \qquad (2\text{-}2)$$

The latter is often approximated by $\sigma_0\ (r_0/L)^2/4$, where L is the focal length of the objective lens and r_0 is the aperture radius measured from the optical axis on the focal plane; the approximation results from $r_0 << L$. Here f gives half-width at half-height of the aperture function for a conventional pinhole aperture. If we consider a jth fringe off-axis, provided that the angle between this fringe peak and the axis is χ_j, the order of

interference m is given as

$$m = n-j = 2\mu t\sigma_0 \cos\chi_j = n\cos\chi_j \tag{2-3}$$

When we utilize the jth zone aperture having a half-width $f = (\sigma-\sigma_0)/2$ (σ_0 and σ are the wavenumbers which correspond to the inner and outer edge of the zone, respectively), the following equation will apply:

$$m = n-j = 2\mu t\sigma_0 \cos\chi_j^{in} \tag{2-4}$$

$$= 2\mu t\sigma \cos\chi_j^{out} \tag{2-5}$$

where χ_j^{in} and χ_j^{out} are the angles between the inner or outer edge and axis respectively. Then we can again obtain the relationship between the broadening in wavenumbers and the geometry as

$$\cos\chi_j^{in} = (n-j)/n \tag{2-6}$$

$$\cos\chi_j^{out} = (n-j)/(n+2nf/\sigma_0) \tag{2-7}$$

From equations (2-2), (2-6), and (2-7) we can determine r_0, r_j^{in}, and r_j^{out}, the radius of the central hole and inner and outer radii of the zone, respectively.

$$r_0 = 2L \frac{[f(f+\sigma_0)]^{1/2}}{\sigma_0} \tag{2-8}$$

$$r_j^{in} = L \frac{[2j/n-(j/n)^2]^{1/2}}{1-j/n} \tag{2-9}$$

$$r_j^{out} = L \frac{[(2-j/n+2f/\sigma_0)\ (j/n+2f/\sigma_0)]^{1/2}}{1-j/n} \qquad (2\text{-}10)$$

Let us now consider solid angles subtended by the central hole and the jth zone. For the central hole,

$$\Omega_0 = \frac{4\pi f}{\sigma_0(1+2f/\sigma_0)} \qquad (2\text{-}11)$$

For the jth zone,

$$\Omega_j = \frac{4\pi f(1-j/n)}{\sigma_0(1+2f/\sigma_0)} \qquad (2\text{-}12)$$

Since f/σ_0 is usually negligible compared to unity, when j is negligible compared to n, then both solid angles described above are almost the same constant value

$$\Omega \simeq \frac{4\pi f}{\sigma_0} \qquad (2\text{-}13)$$

Therefore, if we can use an MZA consisting of J zones besides the usual central hole, the gain of throughput will be J+1 times greater than that of the central hole alone. Practically, the gain may be somewhat reduced because of the relatively large incident angles to an interference filter, which is usually used as a premonochromator, and the transmittance of the substrate of the MZA.

Optimum Width of Aperture

Since the throughput of the F.P. interferometer is proportional to the solid angle Ω subtended by the aperture, it is obvious that the wider the aperture, the more intense the resulting signal becomes. However, wide aperture reduces resolving power simultaneously. Therefore, we have to find the optimum value of aperture width which gives the best results for

temperature measurements. Chabbal [1953] found that, when the source function is completely monochromatic, an aperture having a width which is almost the same as that of the etalon function gives the maximum value of the product of luminosity and resolution. In the case where the source function has a definite width, he suggested that an aperture which has a width equal to that of the function which is a convolution of the etalon function and the source function gives the maximum value of the product of luminosity and resolution. However, he did not report an analytic method which relates the aperture width to the product of luminosity and resolution for the general case where etalon characteristics and the width of the source function are given a priori.

Furthermore, it is by no means clear that a maximum luminosity-resolution product corresponds to the optimum experimental situation in terms of final error in temperature measurements. In the interest of finding the best experimental arrangement, we have adopted the approach of finding a relationship between the temperature error and the aperture width for particular experimental conditions (etalon parameters and source region temperature) when the measurements are to be made with the photon counting method.

The instrument response function S(x,T), which is obtained through a MZA, of a Gaussian temperature-broadened source line is given here by the following equation according to expression (2-11) of Hays and Roble [1971].

$$S(x,T) = I_0[A_0 + \sum_{m=1}^{\infty} A_m \exp\left(-\frac{m^2}{4}\gamma T\right)\cos mx] + C \qquad (2\text{-}14)$$

where

$$A_0 = \frac{1}{2\pi}$$

$$A_m = \pi^{-1} R^m \exp\left(-\frac{m^2}{4} D^2\right) \operatorname{sinc}\left(\frac{m}{N_{D_f}}\right) \operatorname{sinc}\left(\frac{2mf}{\Delta\sigma}\right)$$

$$D = \frac{\pi}{N_{D_g} (1n2)^{1/2}}$$

$$\gamma = 7.3 \times 10^{-12} \frac{1}{M} \left(\frac{\sigma_0}{\Delta\sigma}\right)^2$$

$$I_0 = 5x10^5 A\left(\sum_{j=0}^{J} \Omega_j\right) R_Y \tau_a T_t P_e (1-R) (1+R)^{-1} \qquad (2\text{-}15)$$

$$\operatorname{sinc}(\beta) = \sin(\pi\beta)/(\pi\beta)$$

Here $x = 4\pi\mu t\sigma\cos\chi$ is related to the phase difference between the various rays emerging from the etalon, R is the reflectivity of the etalon coating, N_{D_g} is the finesse representing the microscopic roughness defect of the etalon, N_{D_f} is the finesse representing the spherical defect, $\Delta\sigma = (2\mu t\cos\chi)^{-1}$ is the free spectral range, M is the molecular weight of the light-emitting atom, T is the gas kinetic temperature, A is the effective collecting area of the interferometer, R_Y is the brightness of the source in rayleighs, τ_a is the transmission coefficient that includes the effects of absorption and scattering of the etalon coatings, T_t is the transmission of various optical surfaces of the interferometer and premonochromator, P_e is the quantum efficiency of the photomultiplier and C is the continuum background. This formulation of the final response function is described in detail in the works by Hays and Roble [1971] and Hernandez [1966].

The function of equation (2-14) can be expressed in the form which excludes the nomalizing factor and continuum background as

$$Y(x,T) = 1+2 \sum_{m=1}^{\infty} A'_m \exp\left(-\frac{m^2}{4}\gamma T\right) \cos mx \qquad (2\text{-}16)$$

where $A'_m = \pi A_m$.

The actual recorded signal with a photon counting method contains inevitable noise superimposed on the function expressed by equation (2-14). When the standard deviation of the noise is the square root of the counting rate of the signal, the mean square temperature error, which we will use in our analysis, is given by the following equation according to the expression (2-21) of Hays and Robel [1971].

$$\overline{\Delta T} = \left[\frac{\alpha}{NI_0} \left(1 + \frac{\beta}{\alpha} \frac{C}{I_0}\right) \right]^{1/2} \qquad (2\text{-}17)$$

Here N is the number of data points over one free spectral range, and α and β are expressed as

$$\alpha = \frac{1}{\pi^2} \sum_{i=1}^{N-1} \frac{S(x_i,T)}{I_0} \psi(x_i)\, \delta x$$

$$\beta = \frac{1}{\pi^2} \sum_{i=1}^{N-1} \psi(x_i)\, \delta x$$

$$\psi(x_i) = \frac{32\pi}{\gamma^2} \sum_{m=1}^{M} \cos^2(mx_i)$$

$$x \left[\frac{\dfrac{A_m \exp\left(-\frac{m^2}{4}\gamma T\right)}{\{A_m^2\}} - \dfrac{m^2 A_m \exp\left(-\frac{m^2}{4}\gamma T\right)}{\{m^2 A_m^2\}}}{\dfrac{\{m^4 A_m^2\}}{\{m^2 A_m^2\}} - \dfrac{\{m^2 A_m^2\}}{\{A_m^2\}}} \right]^2$$

where $\delta x = \dfrac{2\pi}{N-1}$

$$x_i = 2\pi \frac{i-1}{N-1}$$

$$\{Q_m\} = \sum_{m=1}^{M} Q_m \exp\left(-\frac{m^2}{2}\gamma T\right)$$

As seen from equation (2-15), I_0 contains Ω_j which is related to the half-width of the aperture function f through the equation (2-13). Therefore, the mean square temperature error can be written in a form containing f as follows:

$$\overline{\Delta T} = \left[\frac{\alpha}{NK_0 f}\left(1 + \frac{\beta}{\alpha}\frac{C}{K_0 f}\right)\right]^{1/2} \qquad (2\text{-}18)$$

where

$$K_0 = \frac{4\,(1-R)}{\sigma_0 (1+R)} B_0$$

$$B_0 = 5 \times 10^5 \, A \, R_Y \, \tau_a \, T_t \, P_e \, (J+1)$$

The mean square temperature error calculated for the etalon whose characteristics are given in Table 2-1 is plotted in Figure 2-1 as a function of the half-width of the aperture function. The calculations were made for three different temperatures, 700° K, 1000° K, and 1500° K, and for $B_0 = 1 \times 10^9$ (counts . sec^{-1} . $sterad^{-1}$) and N = 100. The results are given here for the two cases where there is no continuum background, and where 20 counts of continuum background exists. In Figure 2-1, counting rates of the peak signal for three different temperatures and the overall instrumental finesse are also given as a function of the aperture width. As can be seen in Figure 2-1, a certain definite width of aperture gives the lowest value of temperature error for a given temperature. It is seen in Figure 2-1 that the optimum aperture width, which gives minimum temperature error, increases with increasing temperature. Considering the highest possible value obtained from the Doppler temperature measurements of 630.0 nm emission (~1500° K), we designed the half-width of the aperture function of our MZA to be 30 mk. The higher the temperature is, the more the source line profile is broadened and its peak lowered. Thus the lower peak signal and the greater temperature error are resulting from the higher temperature, as seen in Figure 2-1. The change in B_0, which in turn relates linearly to the change in source intensity, affects little the value of the optimum aperture width. For example, using the etalon parameters given in Table 2-1 and N = 100, T = 1500° K, the optimum aperture width stays at 30 mk over the range of B_0 of 1×10^8~1×10^{10} with no background continuum. When 20 counts of background continuum are introduced, the optimum aperture width varies

TABLE 2-1

The Operating Parameters for the Fabry-Perot Interferometer

Etalon Plates	
Effective diameter	14.6 cm
Flatness	$\lambda/120$
Roughness defect finesse, N_{D_g}	30
Reflectivity	0.96 at 6300 Å
Reflective finesse, N_R	77
Spherical defect finesse, N_{D_f}	20
Spacing	1.504 cm
Collimator	
Focal length	73.31 cm
Multiple Zone Aperture	
Number of zones	10
Half-width	0.030 cm^{-1}
Interference Filter	
Diameter	7.62 cm
Half-width at half-height	7.6 cm^{-1}
Peak transmission	53%
Peak wavelength	6303 Å
Wavelength of Airglow Line	6300 Å

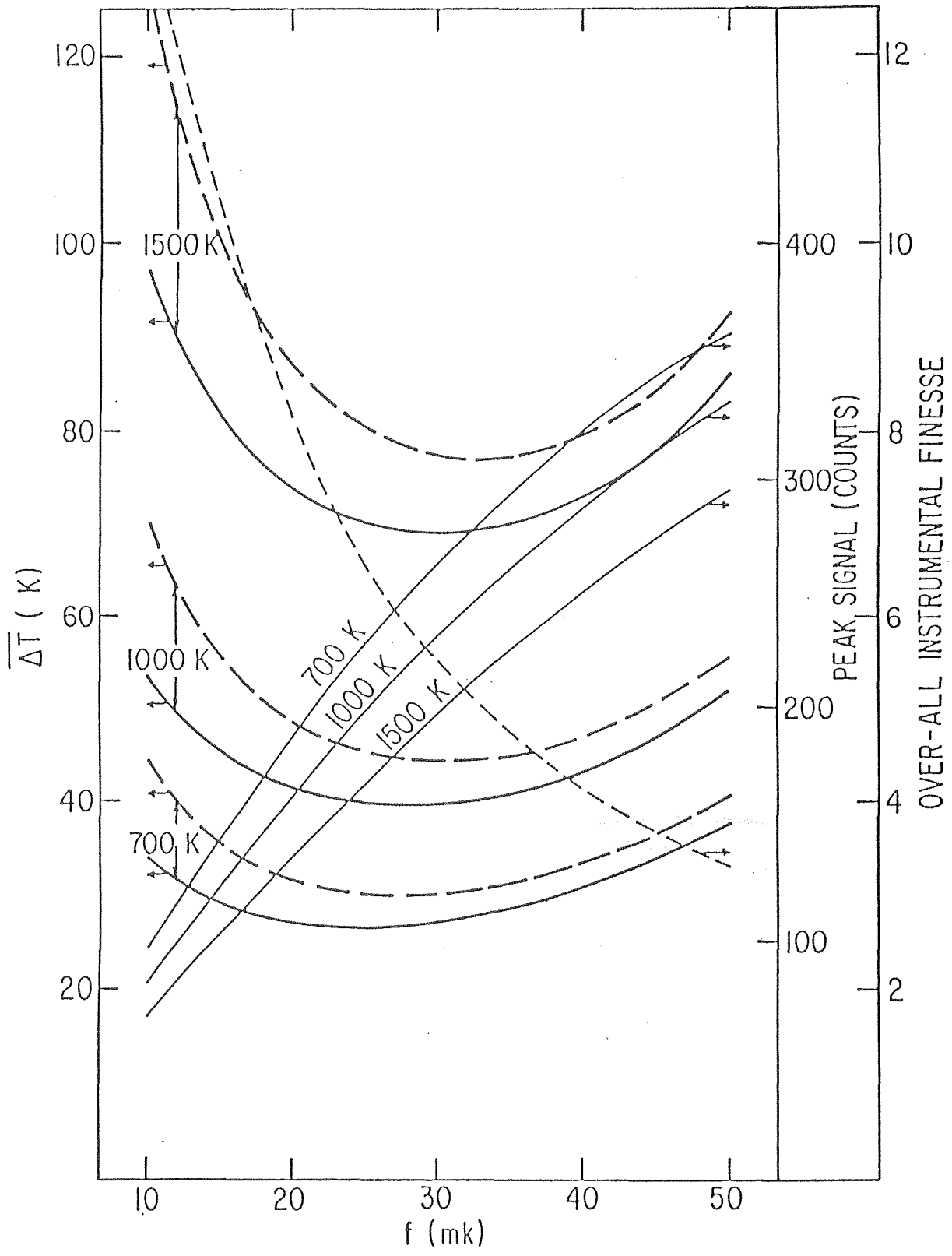

Figure 2-1 Mean square temperature error as a function of an aperture half-width. These values are calculated for temperatures of 700° K, 1000° K, and 1500° K. Solid lines are for zero and dashed lines are for 20 counts of continuum background, respectively. Also plotted are the peak counting rates of a recorded signal (fine solid lines) for the three different temperatures, and the over-all instrumental finesses. The instrumental parameters used are given in Table 2-1.

from 38 mk at $B_0 = 1 \times 10^8$ to 30 mk at $B_0 = 1 \times 10^{10}$.

Effects of Defects of the MZA

The MZA could be fabricated by several methods. Recent developments of the semiconductor industry make the photographic reduction process the most suitable for our purpose. The first step is making an enlarged drawing of a single zone aperture which can be done using an automatic plotting machine. The next step is a photographic reduction of the original artwork to generate the desired dimensions on a photographic plate. The defects in fabricating the zone aperture are inevitable; therefore the effects arising from such defects have to be estimated. These defects may be classified into two groups according to their characteristics. The defect of the first type is a systematic error in the radii of the zones. For example, this may be caused by errors of the photographic reduction, or by errors in measurements of the focal length of the objective lens or etalon spacing. The defect of the second type is a random error of the radius of the zone. This may be caused by an error in drawing the original artwork, by the roughness of the grain of the photographic plate, etc. This error is considered to have normal distribution and leads to a Gaussian broadening function.

At first, let us consider the defect of the first type, which we may call systematic defect. Here, let us assume that the inner and outer radius of every zone (including the central hole) is multiplied by the same factor, $1 + k$, from the designed value. When we take the discrepancy in radii from their designed value to be Δr_j^{in} and Δr_j^{out}, we can express $r_j^{in} + \Delta r_j^{in} =$

$(1+k)r_j^{in}$ and $r_j^{out} + \Delta r_j^{out} = (1+k)r_j^{out}$. When discrepancies in order of interference are α_j^{in} and α_j^{out} corresponding to inner and outer radius of jth zone respectively, the following equation will hold from equation (2-9) and (2-10):

$$[2(j+\alpha_j^{in})/n-\{(j+\alpha_j^{in})/n\}^2]^{1/2}/\{1-(j+\alpha_j^{in})/n\} =$$

$$(1+k)\ \{j/n-(j/n)^2\}/(1-j/n) \tag{2-19}$$

$$[\{2-(j+\alpha_j^{out})/n+2f/\sigma_0\}\{(j+\alpha_j^{out})/n+2f/\sigma_0\}]^{1/2}/\{1-(j+\alpha_j^{out})/n\}=$$

$$(1+k)\ \{(2-j/n+2f/\sigma_0)(j/n+2f/\sigma_0)\}^{1/2}/(1-j/n) \tag{2-20}$$

Taking into consideration that j/n, f/σ_0, and k are very small compared to unity, we can neglect their square terms. Thus, α_j^{in} and α_j^{out} can be obtained in the form as following:

$$\alpha_j^{in} \simeq 2kj(1-j/n) \tag{2-21}$$

$$\alpha_j^{out} \simeq 2k(j+2nf/\sigma_0)(1-j/n) \tag{2-22}$$

The discrepancies in order, α_j^{in} and α_j^{out}, are related to the discrepancies in phase, δ_j^{in} and δ_j^{out}, by the equation

$$\delta_j^{in} = 2\pi\alpha_j^{in} \simeq 4\pi kj(1-j/n) \tag{2-23}$$

$$\delta_j^{out} = 2\pi\alpha_j^{out} \simeq 4\pi k(j+2nf/\sigma_0)(1-j/n) \tag{2-24}$$

If we take the average value between α_j^{in} and α_j^{out}, and that between δ_j^{in} and δ_j^{out}, they are expressed as:

$$\alpha_j^{av} \simeq 2k(j+nf/\sigma_0)(1-j/n) \tag{2-25}$$

$$\delta_j^{av} = 2\pi\alpha_j^{av} \simeq 4\pi k(j+nf/\sigma_0)(1-j/n) \tag{2-26}$$

Here the values of $(\alpha_j^{av}-\alpha_j^{in})/\alpha_j^{in}$ and $(\alpha_j^{out}-\alpha_j^{av})/\alpha_j^{out}$ ranges from 9×10^{-2} and 8×10^{-2} for j = 1 to 9×10^{-3} and 9×10^{-3} for j = 10, respectively, using the parameters given in Table 2-1. Such small amounts of these values mean that the average values, α_j^{av} and δ_j^{av}, can be regarded as representative values of α_j^{in} and α_j^{out}, and δ_j^{in} and δ_j^{out}, respectively.

Now, let us consider the change in aperture width of jth zone arising from the systematic change in the inner and outer radius of the zone. The designed values of inner and outer radii of the zone correspond to the wavenumbers σ_0 and $\sigma_0 + 2f$, respectively. When the inner and outer radii of the jth zone are displaced amounting to α_j^{in} and α_j^{out} in order of interference respectively, the corresponding displacements in wavenumber are $\sigma' = \alpha_j^{in}\,\Delta\sigma$ for inner radius and $\sigma'' = \alpha_j^{out}\Delta\sigma$ for outer radius. Therefore, the designed aperture full width, 2f, changes to $2f + (\sigma'' - \sigma')$. The ratio of the changed amount in full aperture width to the designed full aperture width is obtained through equations (2-21) and (2-22) as follows:

$$\frac{\sigma'' - \sigma'}{2f} = 2k\,\frac{\Delta\sigma}{\sigma_0}\,(n-j) \tag{2-27}$$

Using the instrumental parameters listed in Table 2-1, the value of equation (2-27) is 2×10^{-3} for $k = 1 \times 10^{-3}$ over the range of j from 1 to 10. Therefore, the variation of the half-width at half-height of the aperture function can be neglected. Thus the output profile of the jth zone having a defect of the first type, excluding the normalizing factor and continuum background, can be obtained by replacing x in equation (2-16) with $x - \delta_j^{av}$. When the MZA consists of J zones besides the central hole, the output profile is expressed by the sum of the contribution of each zone. In the following discussion all of the contributions of each zone are assumed to be the same unless stated otherwise. Thus, the resulting profile is expressed as follows:

$$Y_a(x,T) = \sum_{j=0}^{J} [1+2 \sum_{m=1}^{\infty} A'_m \exp(-\frac{m^2}{4}\gamma T) \cos m (x-\delta_j^{av})] \qquad (2\text{-}28)$$

For the defect of the second type, that is the defect arising from the random error of the radius of the zone, provided that Δr_j^{in} and Δr_j^{out} are distributed around zero in a nomal distribution with standard deviation β, the probability functions are

$$M(\Delta r_j^{in}) = \frac{1}{\beta\sqrt{2\pi}} \exp [-\frac{(\Delta r_j^{in})^2}{2\beta^2}] \qquad (2\text{-}29)$$

$$N(\Delta r_j^{out}) = \frac{1}{\beta\sqrt{2\pi}} \exp [-\frac{(\Delta r_j^{out})^2}{2\beta^2}] \qquad (2\text{-}30)$$

These functions are expressed in terms of x as:

$$M(x) = \frac{1}{B_j^{in}\sqrt{\pi}} \exp [-\frac{x^2}{(B_j^{in})^2}] \qquad (2\text{-}31)$$

$$N(x) = \frac{1}{B_j^{out}\sqrt{\pi}} \exp\left[-\frac{x^2}{(B_j^{out})^2}\right] \tag{2-32}$$

where

$$B_j^{in} = \frac{4\sqrt{2}\ \pi\ j(n-j)}{nr_j^{in}}\ \beta \tag{2-33}$$

$$B_j^{out} = \frac{4\sqrt{2}\ \pi\ (j+2nf/\sigma_0)(n-j)}{nr_j^{out}}\ \beta \tag{2-34}$$

Here, when the average value, B_j^{av}, between B_j^{in} and B_j^{out}

$$B_j^{av} = \frac{B_j^{in} + B_j^{out}}{2} \tag{2-35}$$

is introduced, the values of $(B_j^{av} - B_j^{in})/B_j^{in}$ and $(B_j^{out} - B_j^{av})/B_j^{out}$ range from 4×10^{-2} for $j = 1$ to 4×10^{-3} for $j=10$, using the parameters given in Table 2-1. Such small amounts of these values permit us to use the average value, B_j^{av}, as the representative value of both B_j^{in} and B_j^{out}. Therefore, the probablility function in terms of x denoting the defect of the second type is expressed as:

$$O(x) = \frac{1}{B_j^{av}\sqrt{\pi}} \exp\left[-\frac{x^2}{(B_j^{av})^2}\right] \tag{2-36}$$

The output profile of an MZA having the defect of the second type can be obtained now as a convolution of equation (2-14) and (2-36). When expressed, excluding the normalizing factor and continuum background, this function is

$$Y_b(x,T) = \sum_{j=0}^{J} \left[1+2\sum_{m=1}^{\infty} A_m' \exp\left(-\frac{m^2}{4}\gamma T\right) \exp\left\{-\frac{m^2}{4}(B_j^{av})^2\right\}\cos mx\right] \tag{2-37}$$

It is now possible to estimate the degree to which these defects cause a temperature error in the determination of the Doppler temperature. When the output profile (again excluding the normalizing factor and continuum background) is recorded with the defect-free MZA consisting of J zones, the integral over one free spectral range of the square of the difference between the output profile for temperature T (equation (2-16)) and that for temperature T + ΔT is expressed as

$$P(\Delta T) = \int_0^{2\pi} [(J+1)Y(x,T+\Delta T)-(J+1)Y(x,T)]^2 dx =$$

$$4\,(J+1)^2 \sum_{m=1}^{\infty} A'^2_m \exp\left(-\frac{m^2}{2}\gamma T\right)\left[1-\exp\left(-\frac{m^2}{4}\gamma\Delta T\right)\right]^2 \qquad (2\text{-}38)$$

The values of $P(\Delta T)$ are calculated for the instrumental parameters given in Table 2-1 and for T = 1000° K and plotted in Figure 2-2.

On the other hand, the integral over one free spectral range of the square of the difference between the defect-free output profile and the output profile given in equation (2-28) is

$$Q(k) = \int_0^{2\pi} \left[\sum_{j=0}^{J} Y(x,T) - \sum_{j=0}^{J} Y_a(x,T)\right]^2 dx$$

$$= 4\pi \sum_{m=1}^{\infty} \left[\left\{(J+1)A'_m \exp\left(-\frac{m^2}{4}\gamma T\right)\cos m\delta' - \sum_{j=0}^{J} A'_m \exp\left(-\frac{m^2}{4}\gamma T\right)\cos m\delta_j{}^{av}\right\}^2\right.$$

$$\left. + \left\{(J+1)A'_m \exp\left(-\frac{m^2}{4}\gamma T\right)\sin m\delta' - \sum_{j=0}^{J} A'_m \exp\left(-\frac{m^2}{4}\gamma T\right)\sin m\delta_j{}^{av}\right\}^2\right] \qquad (2\text{-}39)$$

Here, the difference between the peaks of these two profiles, Y(x,T) and $Y_a(x,T)$ is adjusted to coincide by $\delta' = \delta_J{}^{av}/2$.

The integral over one free spectral range of the square of the difference between the defect-free output profile and the output profile

given in equation (2-37) is

$$R(\beta)=\int_0^{2\pi}\left[\sum_{j=0}^{J} Y(x,T) - \sum_{j=0}^{J} Y_b(x,T)\right]^2 dx$$

$$= 4\pi \sum_{m=1}^{\infty} A'^2_m \exp\left(-\frac{m^2}{2}\gamma T\right)\left[(J+1)-\sum_{j=0}^{J}\exp\left\{-\frac{m^2}{4}(B_j^{av})^2\right\}\right]^2 \qquad (2\text{-}40)$$

The values of Q(k) and R (β) are calculated for the instrumental parameters given in Table 2-1 and for T = 1000° K and plotted in Figure 2-3. At the top of Figure 2-3, k, which is obtained through $k = \Delta r_{10}^{out}/r_{10}^{out}$, where r_{10}^{out} is calculated using the parameters given in Table 2-1, is also scaled.

From Figures 2-2 and 2-3 it can be concluded that if the errors in manufacturing a MZA are within the tolerances of about Δr_{10}^{out} = 30μm, or $k=2\times10^{-3}$ for the defect of the first type and about β=10 μm for the defect of the second type, the apparent increases in temperature are substantially lower than 20° K and are comparable or smaller than the usual observantional error caused by the statistical noise. This value of tolerance is quite attainable in the fabrication of the MZA. It is obvious that the greater the j value, the greater the need for accuracy. The linear thermal expansion coefficient of a glass substrate (10^{-3} /°K) gives the defects of the first type well below the tolerance mentioned above, $k = 2\times10^{-3}$, for expected temperature variations.

The Actual Use of the MZA

An MZA consisting of 10 zones besides the central pin-hole was constructed with photographic reduction techniques. The half-width is designed to be 30 mk for the optimum condition described before for the

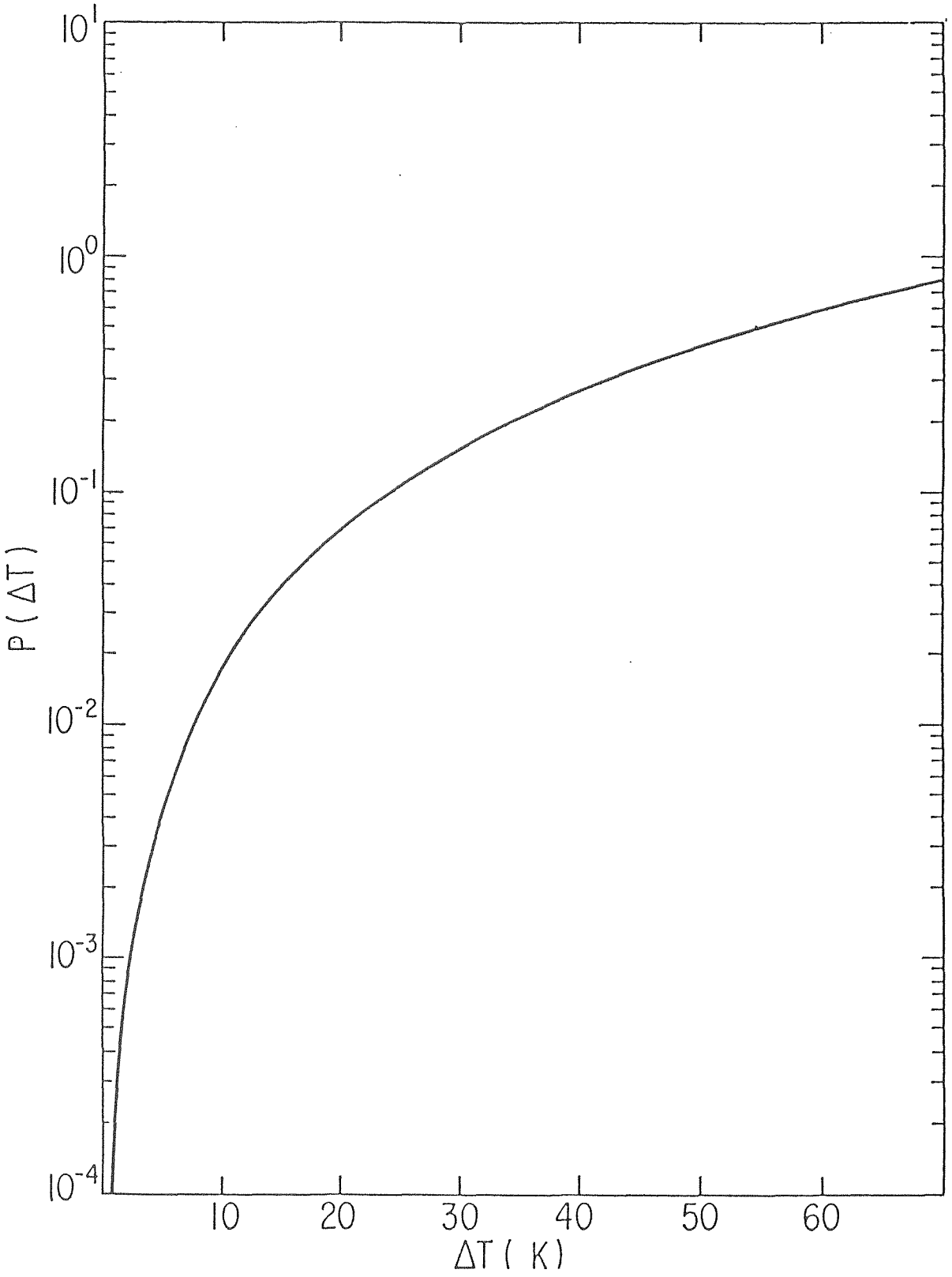

Figure 2-2 The sum over one free spectral range of the square of the difference between the defect free output profile for temperature T = 1000° K and that for temperature T + ΔT as a function of ΔT. The instrumental parameters used are given in Table 2-1.

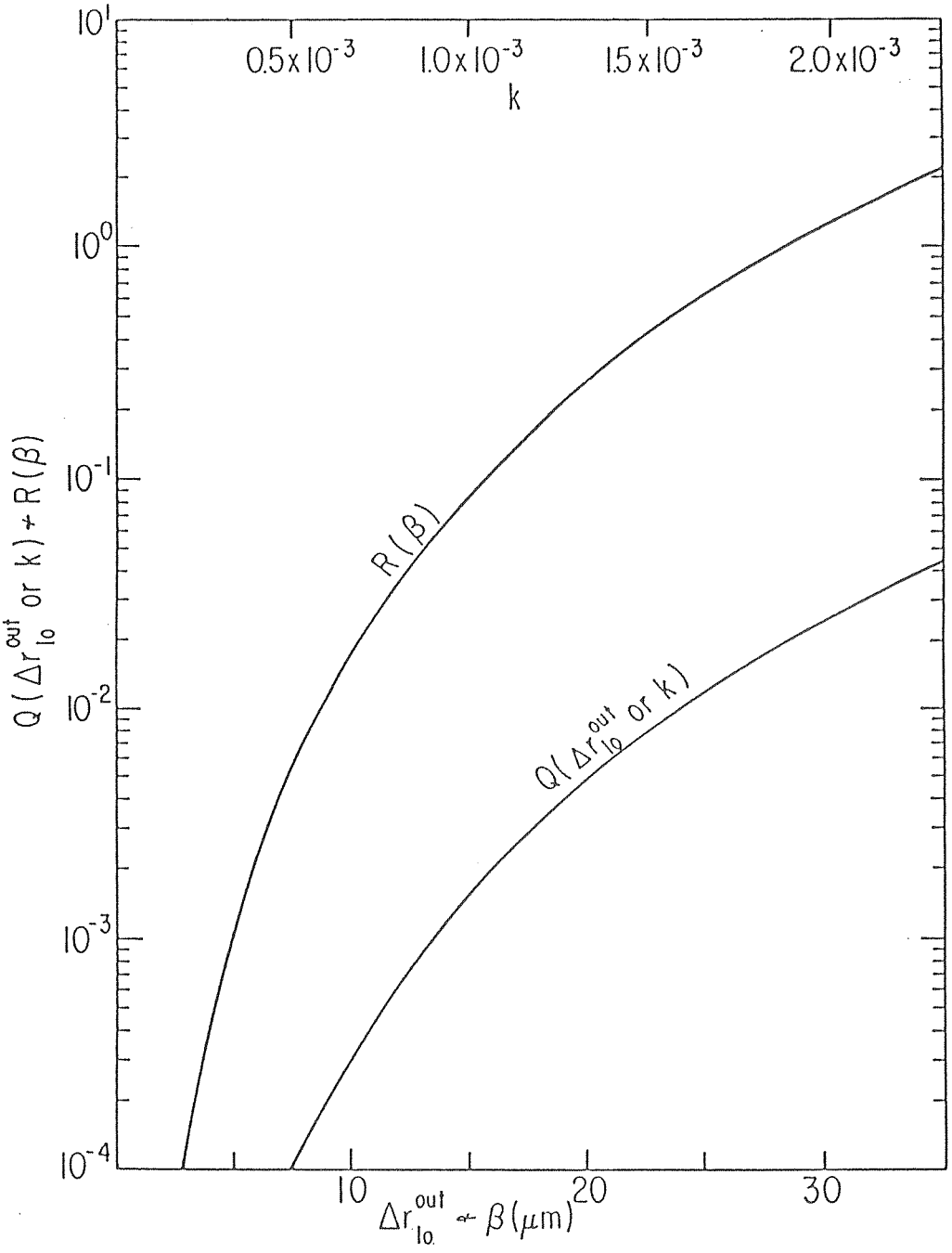

Figure 2-3 The sum over one free spectral range of the square of the difference between the defect-free output profile and the output profile having a defect plotted as a function of the error in making the MZA. The curve Q is for a systematic error in the radii of each zone. The curve R is for a random error in the radius of the zone. Δr_{10}^{out} is a measure of the first type defect, and represents the error of the radius for 10th zone. The radii of other zones are assumed to vary with the same rate k, which is also scaled at the top, from its designed value. β is the standard deviation of the second type defect. The temperature T = 1000° K is assumed. The instru-

measurements of the airglow OI 630.0 nm line. The Fabry-Perot interferometer for these measurements is characterized by its Newtonian telescope-type collimator optics and the use of a Maksutov lens which reduces the aberration. These optics are employed for easy adjustment of the MZA and for gaining compactness and rigidity which is necessary for field use. The total acceptance half-angle for these optics combined with the MZA described above is 1.18°. The MZA is mounted on a 3 axis stage and its position can be adjusted with micrometers so the reflected image of the illuminated MZA can be made to coincide with the actual MZA. The scanning of wavelength is accomplished by changing the pressure of dry air in the etalon chamber. The temperature of the etalon chamber, together with the whole collimator optics and scanning gas, is kept constant by circulating a constant temperature liquid in a water jacket surrounding them. The accuracy of the temperature is ± 0.1° C at 30° C. Vibration absorbing rubber mountings are installed to the platform.

An interference filter having 7.6 K half-width at half height and centered at 15862 K is used as a prefilter. The half-angle of the field of view at the filter is 2.4°. The effects of tilt and field of view on an interference filter were discussed by Hernandez [1974 b], and were estimated for our case. The filter was tilted by 2.2° in order to be centered at 15867 K, the wavenumber of the OI 630.0 nm emission. This caused the half-width of the filter to be broadened to 9.2 K and the peak transmission to be lowered from 54% which is the value for the collimated light parallel to the axis, to 48%.

The photomultiplier is a cooled ITT FW130 tube which has a 0.35 inch diameter photocathode. The Fabry-Perot interferometer system is placed in a trailer which has a steerable mirror system on its roof. The schematic drawing of the system is shown in Figure 2-4. Its operating parameters are given in Table 2-1.

Figures 2-5 a and 2-5 b show, respectively, the signals from the photomultiplier for a scan using the central hole of the MZA alone and for a scan using the whole MZA. The light source for these scans is the 632.8 nm line of a frequency-stabilized He-Ne laser. The conditions other than the apertures are exactly the same for these two scans.

From this comparison it can be seen that the throughput of the instrument using the MZA is increased about 10 times compared to the case in which only the central hole is used, while the finesse remained unchanged. The gain of throughput is slightly below the expected 11 times is primarily due to the transmission loss.

In Figure 2-6, sample records of a weak airglow and of an aurora are shown. The integration times for each data point of these observations are 5 seconds and 1 second, respectively.

A usual single scan of the interferometer for the sky observation covers about 2 interference orders (starting at a minimum). One order of interference consists of about 120 data points. The integration time for each data point varied from 1 second to 10 seconds, depending upon the emission rate so that the difference of the signal between the peak and the background was at least 1000 counts. During the time of aurora,

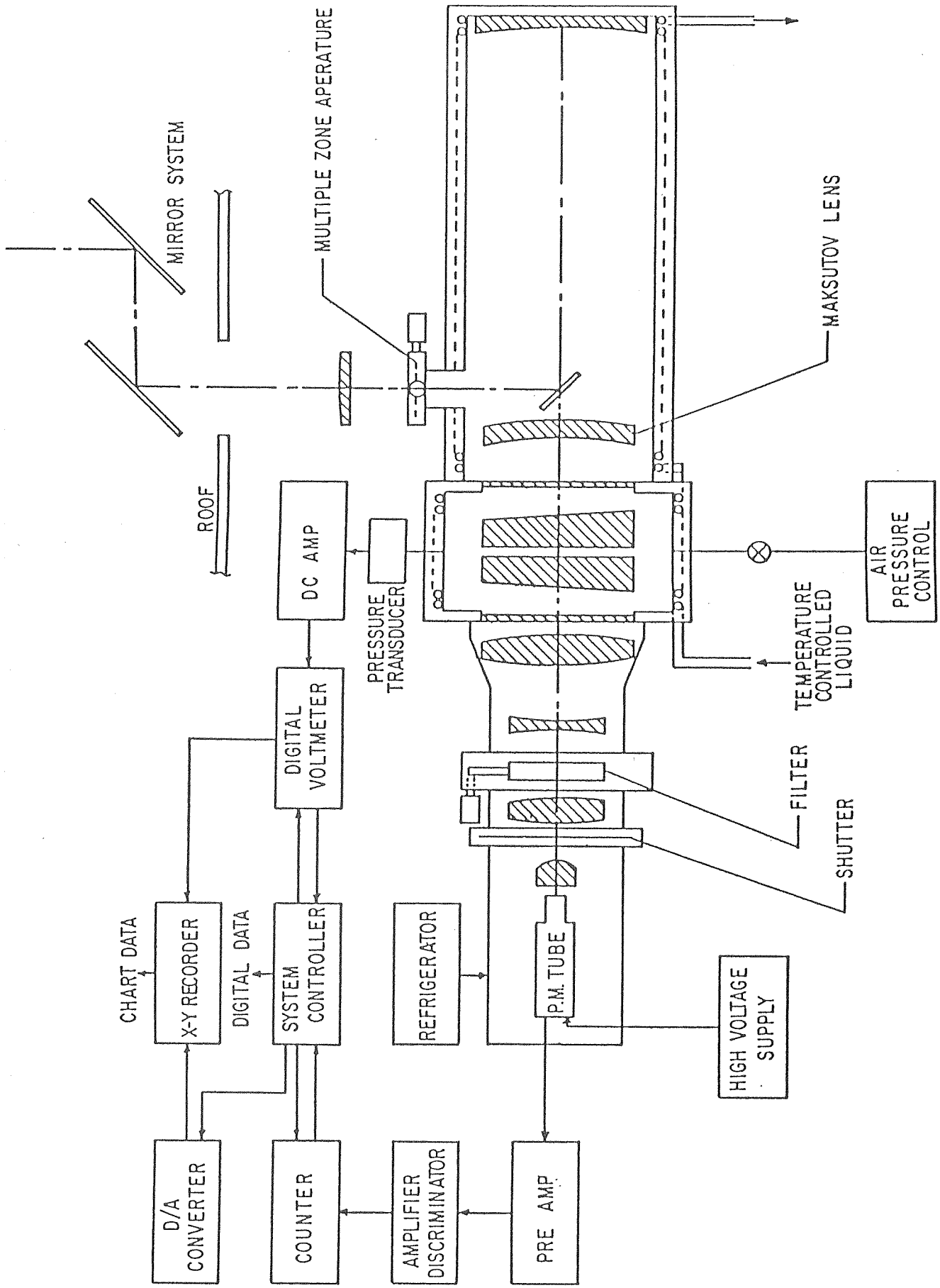

Figure 2-4 The schematic drawing of the Fabry-Perot interferometer system which utilizes the MZA.

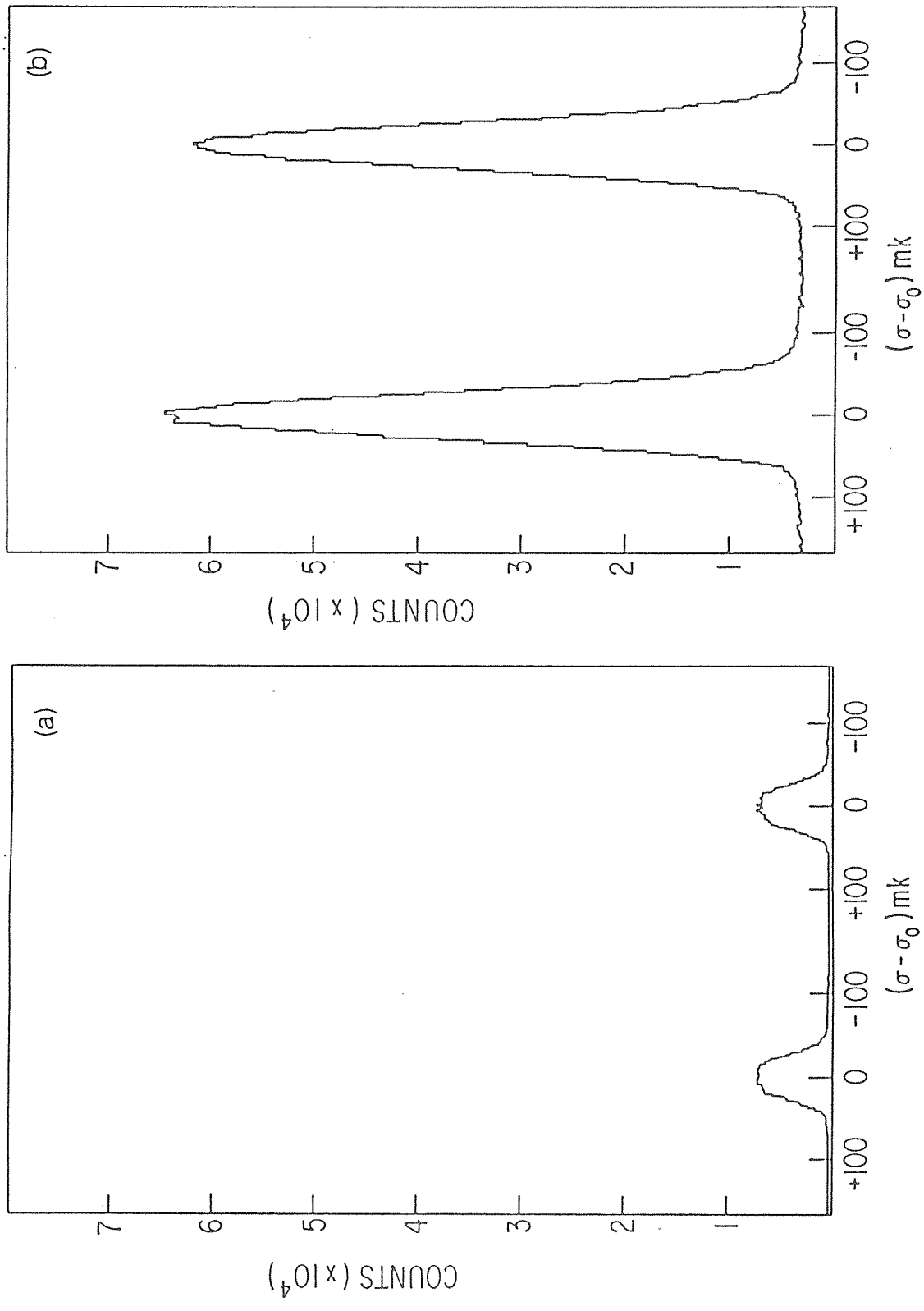

Figure 2-5 The output profiles representing the gain of throughput. The curve (a) was taken through the central hole of MZA alone. The curve (b) was taken through the 10 zones besides central hole. The light source is a diffused 632.8 nm line of a frequency stabilized He-Ne laser.

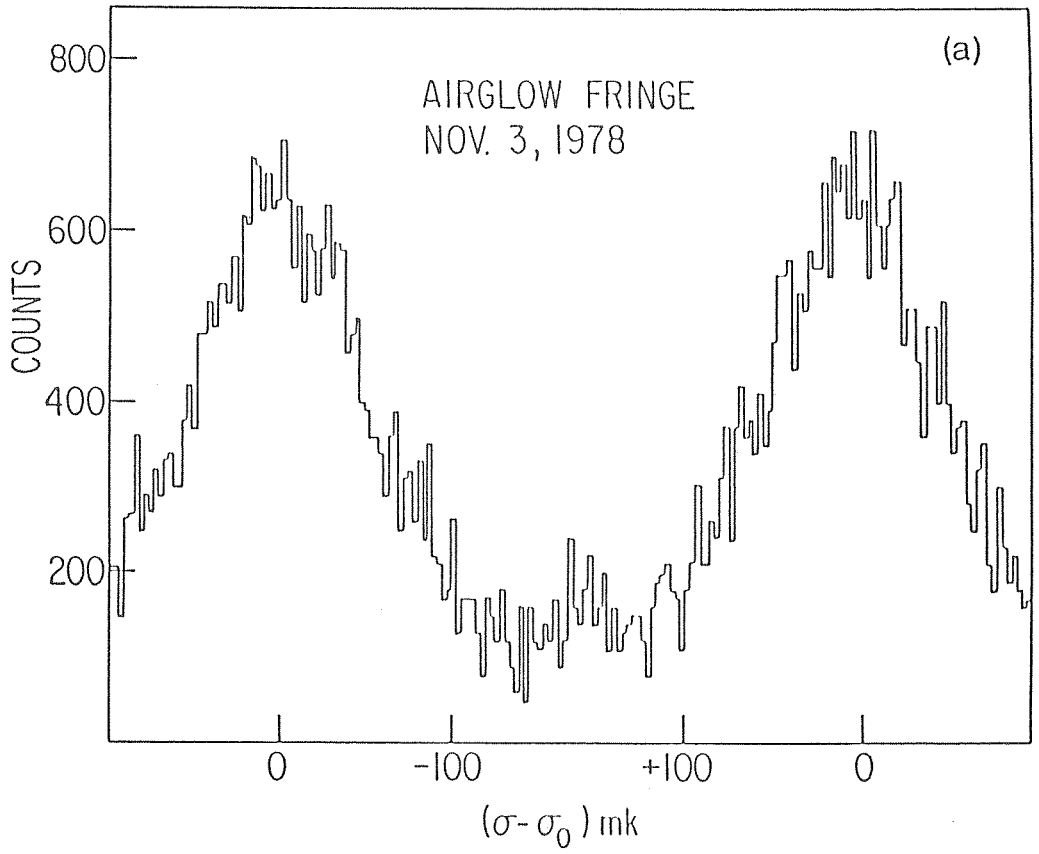
(a)
AIRGLOW FRINGE
NOV. 3, 1978
800
600
400
200
COUNTS
0
-100
+100
0
(σ-σ0) mk

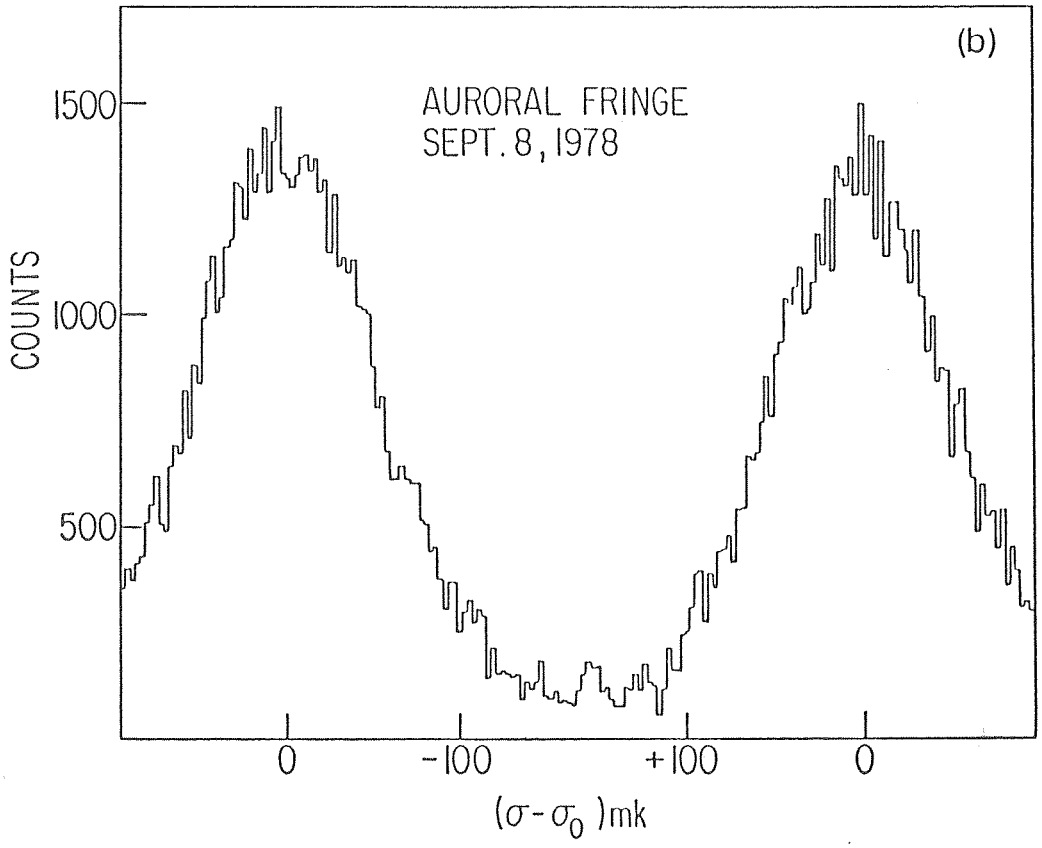
(b)
AURORAL FRINGE
SEPT. 8, 1978
1500
1000
500
COUNTS
0
-100
+100
0
(σ-σ0) mk

intensity variations were sometimes so rapid that the recorded profiles were distorted. For this reason, observed profiles were subjected to a visual inspection to reject the profiles which were asymmetric or showed too large a variation in peak intensities due to large intensity changes during a scan period.

About every three hours during the night, the interferometer was calibrated for instrumental broadening with an evenly diffused 632.8 nm line of a fequency stabilized He-Ne laser which provides illumination over the full aperture of the interferometer.

A Multicolor Meridian-Scanning Photometer

A multicolor meridian-scanning photometer was used along with the interferometer to monitor the north-south distributions of the intensity of the 630.0 nm and 557.7 nm lines and that of the OH lines which may interfere with the interferometric observations [HERNANDEZ, 1974 a].

The photometer scans the sky every 5.5 minutes in a vertical circle along the geomagnetic meridian between 75° north and 75° south in zenith angle and records the emissions at 630.0 nm, 557.7 nm, 610.0 nm, 530.0 nm, and near 800 nm. The field of view of the photometer is 4.7°.

Determination of Doppler Temperature

The following method was used in this research to derive a temperature from an observed fringe.

An observed profile was first transformed into Fourier series, which can be expressed as

$$Y(x) = \frac{Y_{co}}{2} + \sum_{m=1}^{4} Y_m \cos (mx-\alpha_m) \qquad (2\text{-}41)$$

where $Y_m = (Y_{cm}^2 + Y_{sm}^2)^{\frac{1}{2}}$, $\alpha_m = \tan^{-1}(Y_{sm}/Y_{cm})$, and Y_{cm} and Y_{sm} are the Fourier cosine and sine transform of the observed profile for one free spectral rang, respectively.

The first four Fourier transforms (including both cosine and sine transform) were calculated for each fringe to filter out the noise superimposed on the raw data. These low order Fourier coefficients which contribute to the fringe profile were subjected to a non-linear least squares fit with the Fourier decomposition of a theoretical profile. The theoretical profile, which was already given by equation (2-14), has also a form of series expansion and is presented here again with the orders up to four.

$$S(x,T) = I_o[A_o + \sum_{m=1}^{4} A_m \exp\left(-\frac{m^2}{4}\gamma T\right) \cos mx] + C \qquad (2\text{-}14)$$

The Doppler temperature T is then obtained in a least squares sense by minimizing the equation,

$$R(T) = \int_{-\pi}^{\pi} [Y(x)-S(x,T)]^2 dx \qquad (2\text{-}42)$$

Choosing the values of I_o and C that minimize R(T) and evaluating (2-42) we obtain

$$R(T) = \sum_{m=1}^{4} Y_m^2 - \left[\sum_{m=1}^{4} A_m Y_m \exp\left(-\frac{m^2}{4}\gamma T\right)\right]^2 / \sum_{m=1}^{4} A_m^2 \exp\left(-\frac{m^2}{2}\gamma T\right) \qquad (2\text{-}43)$$

and

$$I_o = \sum_{m=1}^{4} A_m Y_m \exp\left(-\frac{m^2}{4}\gamma T\right) \left[\sum_{m=1}^{4} A_m^2 \exp\left(-\frac{m^2}{2}\gamma T\right)\right]^{-1}$$

$$\text{and } C = \frac{Y_{co}}{2} - A_o I_o$$

Therefore, we can obtain the Doppler temperature which minimize R(T) by evaluating the equation (2-43), and at the same time the values of I_o, which is proportional to the emission rate; and C, the counting rate due to continuum background and the dark current counting rate are calculated. The technique for deriving a temperature described above was based on the method given by Hays and Roble [1971]. This technique also provides the background and the 630.0 nm line intensities simultaneously with the temperature.

The instrumental parameters related to the adjustment and the condition of the etalon at the time of each observation were determined by interpolating the values obtained by calibration scans made before, during, and after the entire observation using a stabilized He-Ne laser emission as a source. However, the stability of the etalon was usually good and the defect parameters remain almost constant throughout the night.

The error analysis of temperature was made for each fringe also based on the technique described by Hays and Roble [1971]. The errors calculated by this method using equation (2-18) represent statistical error. The other possibility exists for systematic error arising from instrumental drift. The temperature T_a and T_b were calculated to estimate such systematic error by using the sets of instrumental parameters obtained from the calibration scans made before and after the observation, respectively. The greater value of $|T_a-T_n|$ and $|T_b-T_n|$ was taken to be the largest possible systematic temperature error. The error bars shown in the figures of temperature data represent the greater value of the statistical error and the systematic error for each point.

PART I Thermospheric Temperatures

CHAPTER III

Thermospheric Temperatures during Geomagnetically Quiet Periods

The temperatures measured during geomagnetically quiet periods in May, June and July, 1978 when $K_p \leq 2$ plotted as a function of time in Figure 3-1. The dashed curves shown in the figure give the highest (May 8, 1978) and the lowest (July 2, 1978) exospheric temperatures over one night among those calculated from the MSIS model [Hedin et al., 1977] for the corresponding quiet nights. The solar 10.7 cm flux, the planetary geomagnetic index A_p, the day count from January 1, and the latitude where our measurements were made were taken into account for the calculation of the model temperatures.

The height of the nighttime 630.0 nm emission for normal airglow is peaked slightly below the F2 peak at altitudes above about 250 km [Greer and Best, 1967]. Since the temperature gradient at these heights is quite small, it has been shown both theoretically [Roble et al., 1968] and experimentally [Hernandez et al., 1975; Hays et al., 1970] that temperatures obtained from Doppler profile measurements of 630.0 nm nightglow emission follow closely the exospheric temperature variation. Our quiet time temperature data appear to be consistent within the range of experimental errors with the exospheric temperatures calculated from the MSIS model, which is primarily a magnetically quiet model.

The solid line given in Figure 3-1 represents the least squares fit of the measured temperature for the quiet time.

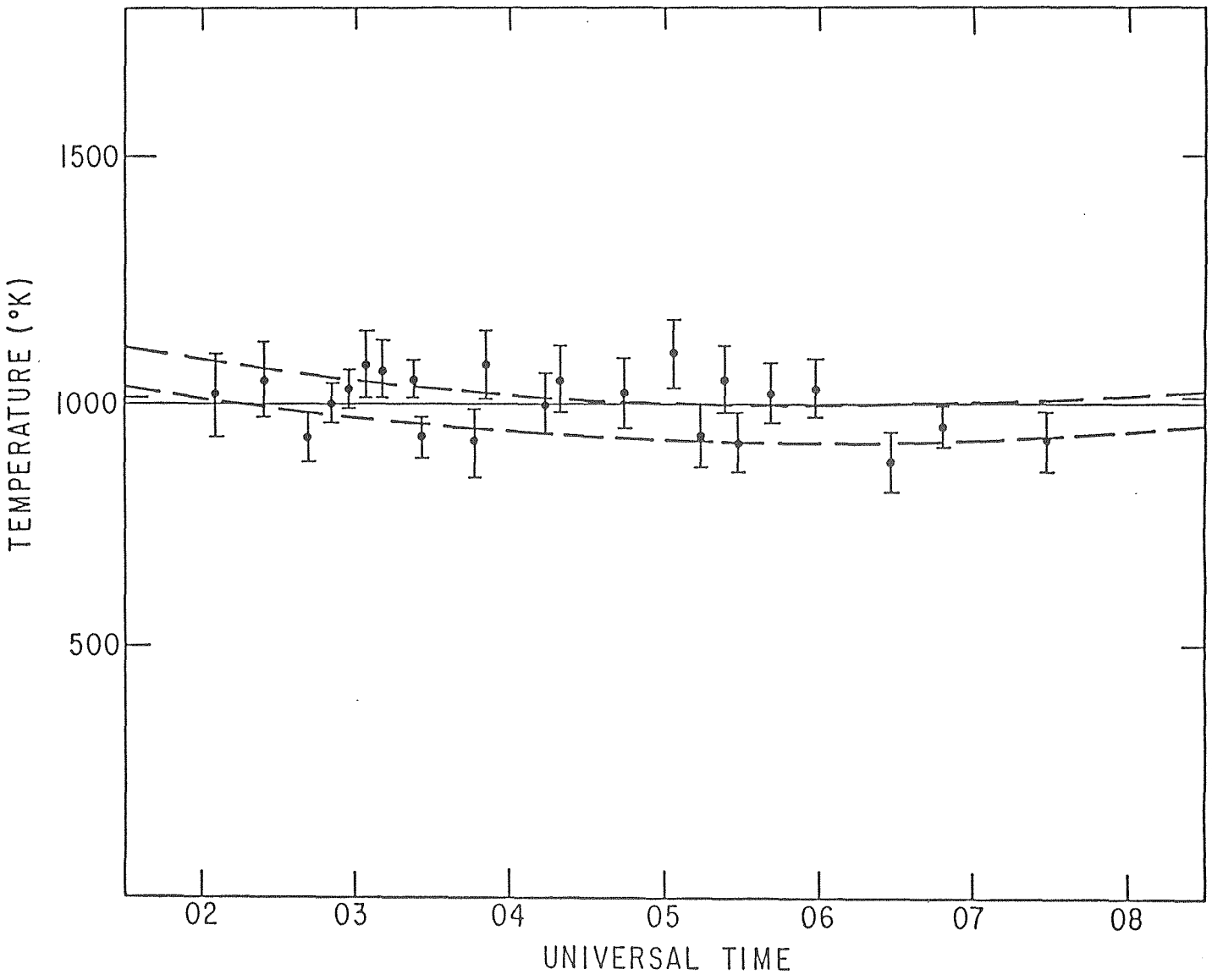

Figure 3-1 Temperatures derived from [OI] 630.0 nm Doppler line profiles during magnetically quiet periods in May, June and July, 1978 when $K_p \leq 2$ as a function of universal time. The solid curve is the least squares fit of our temperature values. The dashed curves give the highest (May 8, 1978) and lowest (July 2, 1978) temperatures calculated from the MSIS model for latitude 42.6° N where our measurements were made.

CHAPTER IV

Thermospheric Temperature Response to an Isolated Substorm

The Joule heating produced by auroral electrojets and its thermospheric response can be studied by monitoring the thermospheric temperatures by means of optical methods; simultaneously investigating the concurrent auroral electrojet activities using geomagnetic records obtained from stations along a meridian close to the observation site of optical measurements.

Cole [1971] originally suggested that the Joule heating input into the thermosphere, which are produced by auroral electrojets, could be estimated by the use of ground-based magnetometers. Indeed, the Joule heating input and the subsequent thermosphere response can be studied by monitoring the thermopheric temperatures by means of optical methods, and simultaneously investigating the concurrent auroral electrojet activities using geomagnetic records obtained at stations along a meridian close to the observing site of optical measurements.

In this Chapter, the measurements of thermospheric response to auroral activities which were made on the night of September 1/2, 1978 (EST) when an isolated substorm occurred, are presented. The intensities and latitudinal positions of auroral electrojets were obtained by the analysis of magnetograms from the IMS Fort Churchill meridian stations.

Magnetometer Data and Method of Analysis

Magnetic data used in this study are the three-component magnetic records of 1-min averages from the IMS Fort Churchill meridian chain stations listed in Table 4-1. Locations of magnetic observatories and

TABLE 4-1

Names, Code Names, and Locations of the Stations

Station	Code Name	Geographic		Geomagnetic	
		Latitude(°N)	Longtitude(°E)	Latitude(°N)	Longitude(°E)
Pelly Bay	PEB	68.53	270.49	78.65	321.06
Rankin Inlet	RIT	62.80	267.67	72.84	323.51
Eskimo Point	EKP	61.10	265.93	70.98	322.38
Back	BKC	57.69	265.77	67.65	324.39
Gillam	GIM	56.35	265.58	66.32	324.87
Island Lake	ISL	53.88	265.32	63.87	325.67
Whiteshell	WHS	49.75	264.75	59.90	325.70

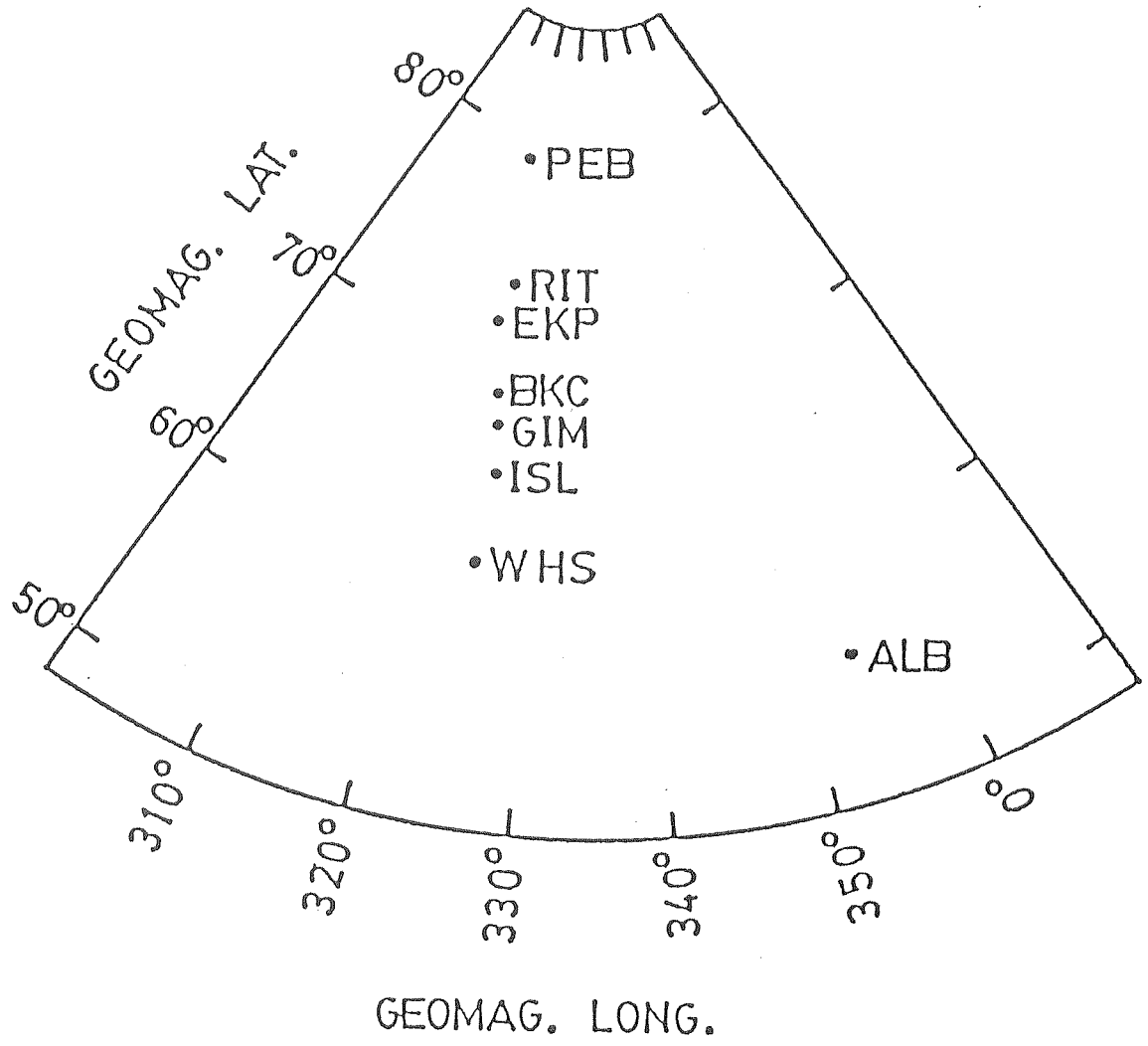

Figure 4-1 Locations of magnetic stations and Albany, New York in geomagnetic coordinates. Also see Table 4-1 for names and coordinates of the stations.

Albany are shown in Figure 4-1. Baseline for these magnetic data were determined by choosing the quietest period closest to the onset of the substorm, using published AE index [Kamei and Maeda, 1981]. The selected time is 0210 UT on September 2, 1978.

The three component data were transformed into X_m (magnetic north), Y_m (magnetic east), and Z (downward) components using magnetic dipole coordinates; stuck-up magnetograms on September 2, 1978 (UT) were then constructed (Figure 4-2). From Figure 4-2 we can see that a westward electrojet was flowing between Back and Island Lake at 0720 UT. This is inferred from the positive ΔZ variations recorded at Back and at higher latitudes and from the negative ΔZ variations recorded at Island Lake and at lower latitudes. In order to determine the position and intensity of the westward electrojet at 0720 UT on September 2, 1978, when the substorm activity had reached its maximum, ΔX_m and ΔZ values at 0720 UT from each station were plotted in Figure 4-3. The best-fitted curves were drawn through ΔX_m and ΔZ data, respectively. The position of the westward electrojet was located at the point where ΔZ values changed from positive to negative and the corresponding intensity of ΔX_m at that location was determined by measuring the maximum negative excursion of ΔX_m on the curve drawn through ΔX_m data. In this manner, the positions and intensities of auroral electrojet at the Fort Churchill meridian were determined every 10 minutes whenever it was possible.

As seen in Figure 4-1, magnetic local time differences between the Fort Churchill meridian and Albany is approximately 2 hours. Since optical observations at Albany were made along the meridian, we employed analytical auroral oval distributions presented by Meng et al. [1977] to correct the electrojet position. The center of this auroral circle is 4.2° colatitude off the geomagnetic pole along the 0015 magnetic local time meridian.

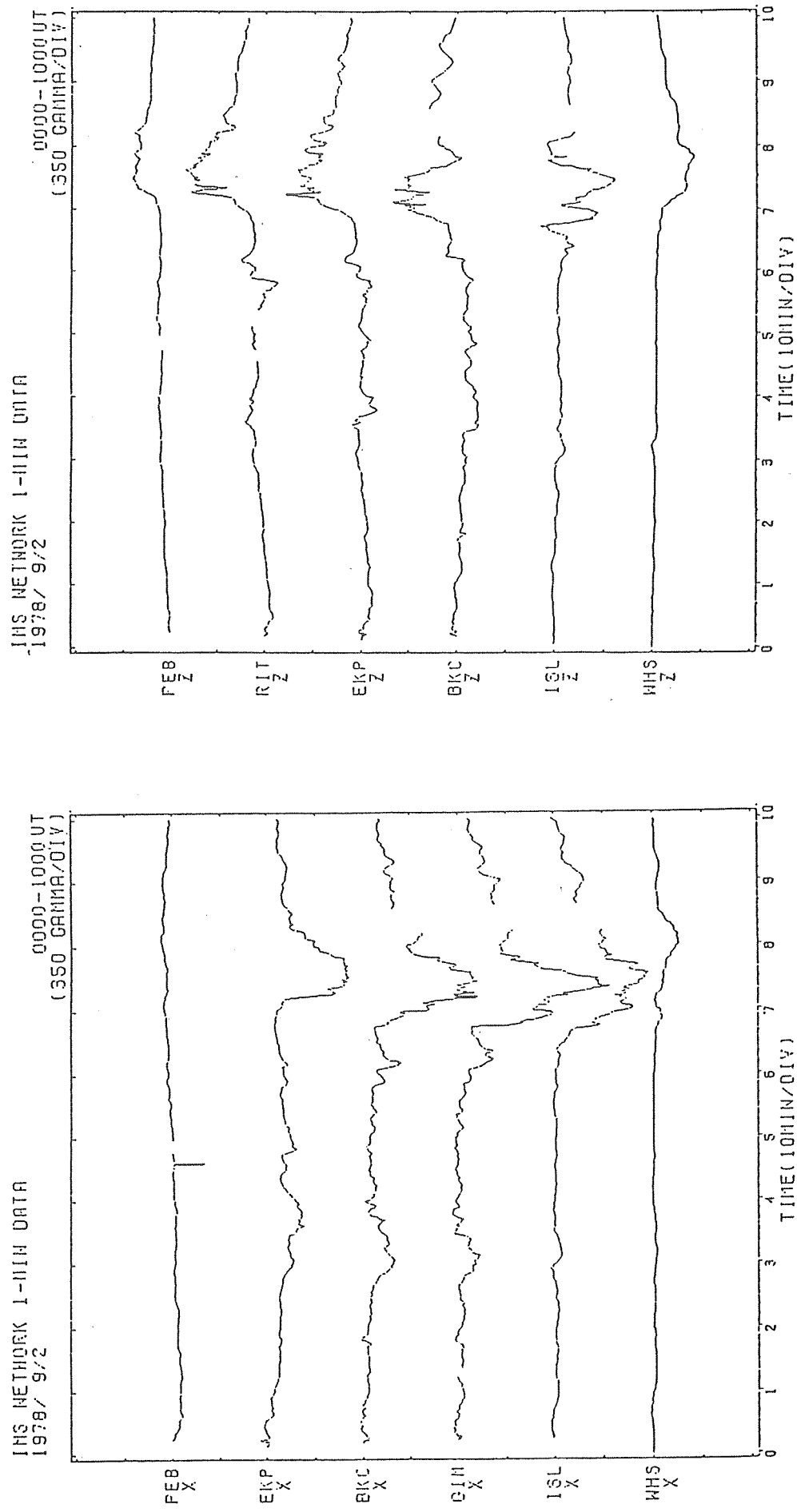

Figure 4-2 The plots of the one-minute averages of X_m (magnetic north) and Z (downward) components observed at stations in the Fort Churchill chain on September 2, 1978 (UT).

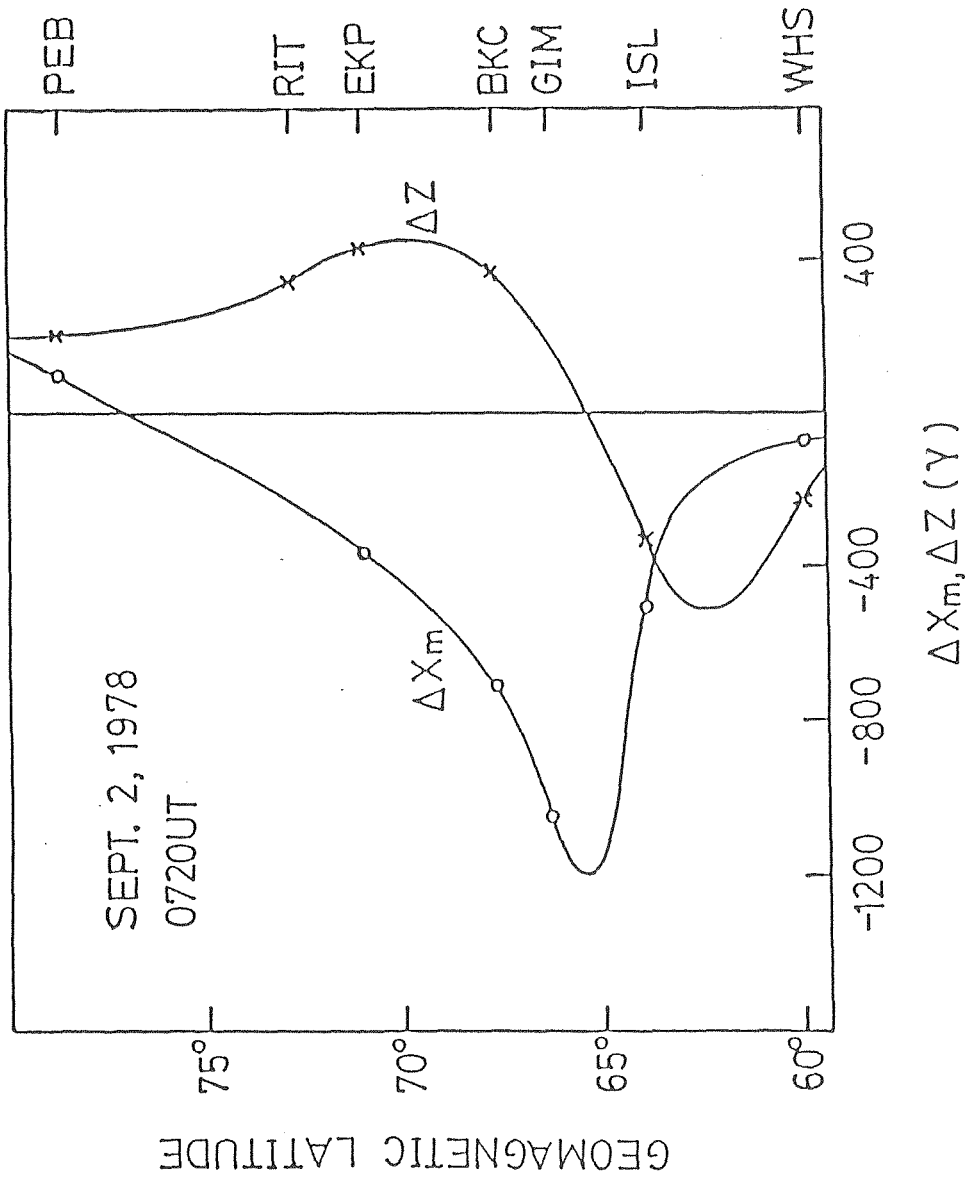

Figure 4-3 ΔX_m and ΔZ values at 0720 UT on September 2, 1978 from each station were plotted and the best-fitted curves were drawn through ΔX_m and ΔZ data, respectively, in order to determine the position and intensity of the westward electrojet.

The amount of this correction is less than 2 degrees in geomagnetic latitude for the time period 0000-1000 UT.

Results

The results of optical thermospheric measurements were compared to the position of the auroral electrojet and $(\Delta X_m^{max})^2$, where ΔX_m^{max} is maximum negative excursion of ΔX_m produced by a westward auroral electrojet. Since it is considered that ΔX_m^{max} represents the intensity of an auroral electrojet current, it would be reasonable to take $(\Delta X_m^{max})^2$ to be the measure of the Joule dissipation of auroral electrojet energy into the thermosphere.

On the night of September 1/2, 1978 (EST) an isolated substorm occurred during the optical measurements. Therefore, it is considered that the results for this night would provide information concerning a typical response to the thermospheric heating of an auroral substorm. Figure 4-4 shows the results for the night of September 1/2, 1978 (EST). The electrojet positions shown in the Figure 4-4 are the corrected values, with the two-hour difference in magnetic local time between the meridian of Fort Churchill and Albany being taken into account. Data gaps in the top and middle panels are due to missing original magnetometer data. It should be noted that the values of (ΔX_m^{max}) in the figure are for the Fort Churchill meridian. An increase in intensity of westward electrojet began at approximately 0640 UT. $(\Delta X_m^{max})^2$ reaches its maximum value of $1.44 \times 10^6 \gamma^2$ at 0720 UT. The westward electrojet, at its maximum intensity, was located approximately 66° in geomagnetic latitude.

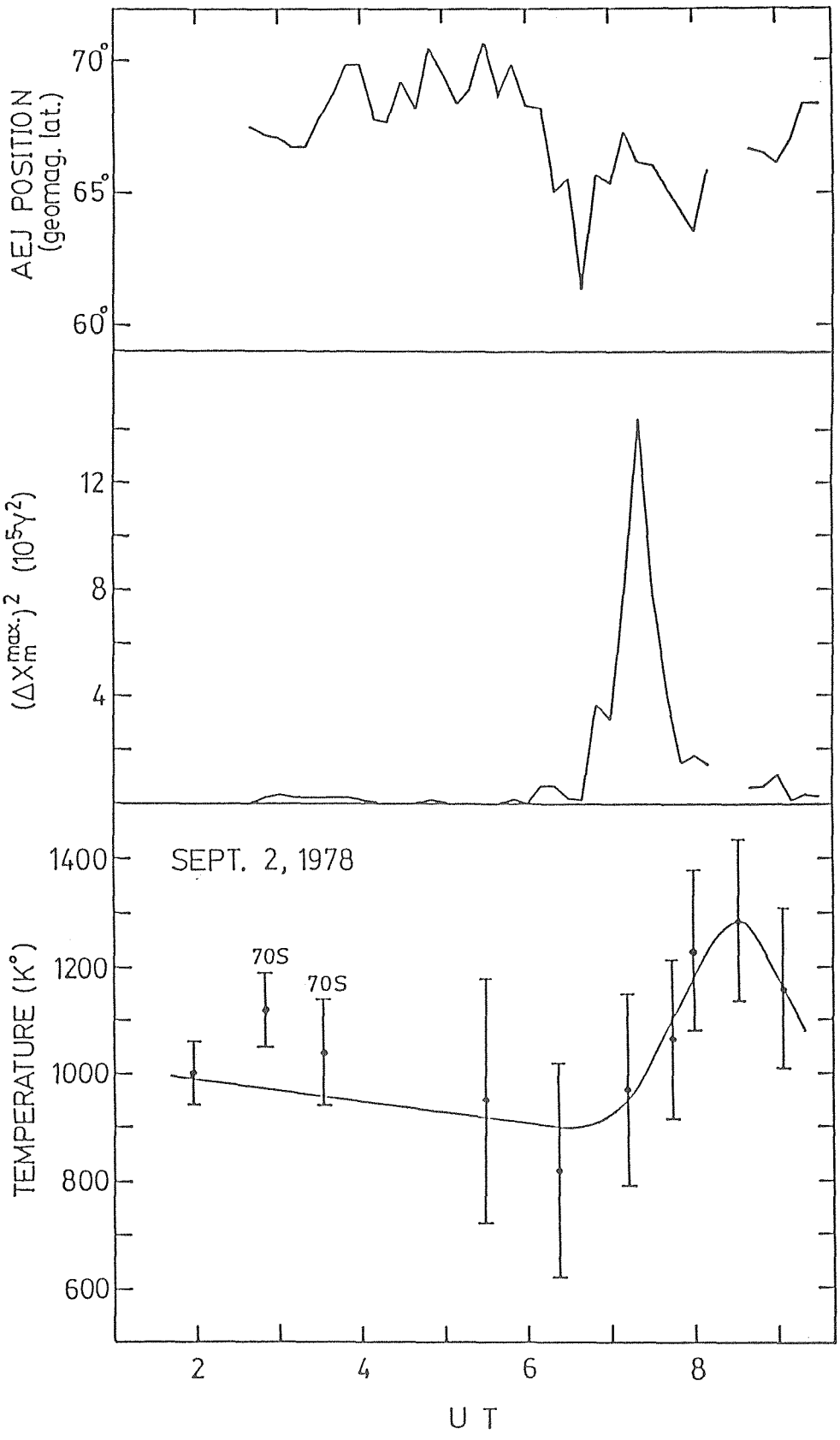

Figure 4-4 The position of electrojet and $(\Delta X_m^{max})^2$ value that were obtained by the analysis of magnetograms from the IMS Fort Churchill meridian chain stations and thermospheric temperature measured from Albany, New York are plotted as a function of universal time from top to bottom, respectively.

The temperatures data, shown in the bottom panel of Figure 4-4, were obtained at the zenith angle of 70° to the north. The data at 0250 UT and 0333 UT were obtained at the zenith angle of 70° to the south. The solid curve in the temperature data is a smoothed line connecting the north measurements. Assuming the height of [OI] 630.0 nm emission to be 250 km, the geomagnetic latitude of the intercept of the line-of-sight for the north measurements is about 59.6°. The increase of temperature measured to the north started about 0700 UT and reached its maximum at about 0830 UT. The amount of temperature increase is almost 400° k. The time history of the temperature measured to the north appears to correspond to the intensification of westward auroral electrojet.

In summary on the night of September 1/2, 1978 (EST) an isolated substorm occurred during the optical measurements. Therefore, the temperature results for this night would provide information concerning a typical response to thermospheric heating of an auroral substorm.

The results show that the intensity of a westward electrojet began to increase at approximately 0640 UT and reached its maximum value at 0720 UT. The intensification of a westward auroral electrojet, in turn, caused the temperature of the thermospheric region, approximately 6° latitude south of the electrojet, to rise as much as 400° K with a time-delay of approximately one hour.

CHAPTER V

Thermospheric Temperatures during Geomagnetically Distrubed Periods

In Chapter 4, the Joule heating input and the subsequent thermospheric temperature response was investigated when an isolated substorm occurred.

In this Chapter, measurements of thermospheric temperatures which were made during five geomagnetically disturbed periods will be given. The observed temperature enhancements are discussed in terms of AEJ activities inferred from the published daily graph of 1-min AE indices (AE, AL, and AU), and the plots of the contributing stations to AL and AU values [Kamei and Maeda, 1981]; from these values the longitudinal locations of the maximum intensity of an AEJ was determined.

Results

Within the period during which the temperatures of quiet time were obtained, several geomagnetic disturbances occurred. The temperatures were obtained for five geomagnetically disturbed periods on the nights of May 4, June 2, June 5, June 11, and June 30, 1978 (UT).

One of the fringes obtained at 0307 UT on June 5, 1978, which gives the value of the temperature close to the quiet time value, is shown by dots in Figure 5-1 as an example. The background continuum is subtracted from the raw data. The solid curve in the figure is the best-fit theoretical profile, which is a convolution of the instrument function and the Gaussian function corresponding to source temperature of 1090° K, while the dashed curve is the theoretical instrument function calculated

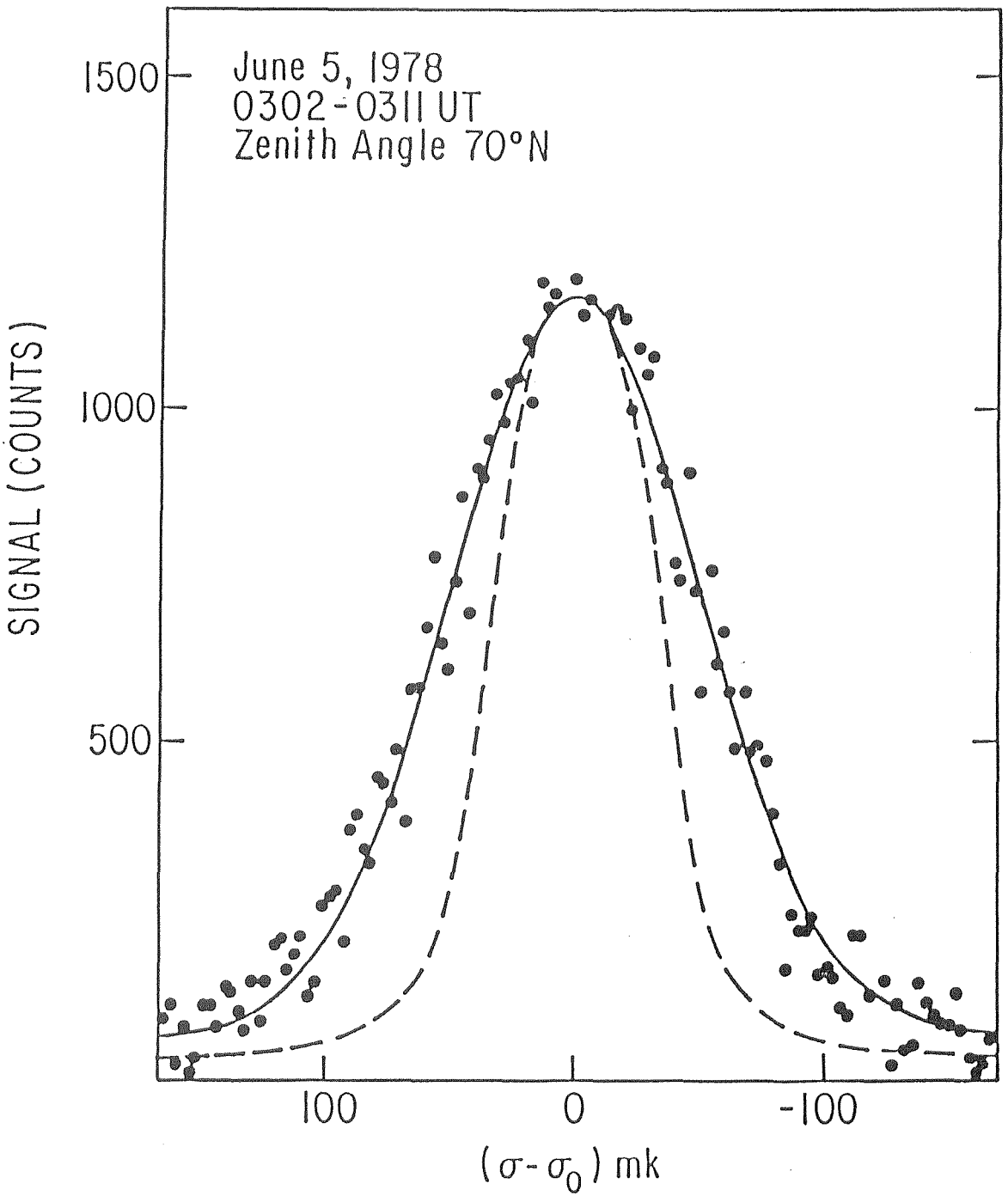

Figure 5-1 The observed 630.0 nm line profile at 0307 UT on June 5, 1978 is shown by dots. The dashed curve is the instrument function of the interferometer. The solid curve is the best-fit theoretical profile calculated from the convolution of the instrument function and the Gaussian function corresponding to a source temperature of 1090° K.

from the four instrumental parameters which were obtained from calibration scans made before and after the observation.

The temperatures obtained during these five periods are plotted as a function of time in Figures 5-2 a - 5-2 e (shown by circles), along with our temperature curve for magnetically quiet periods which is taken from Figure 3-1.

The emission rate derived from the analysis of the observed profiles are also given in Figures 5-2 a - 5-2 e (shown by triangles). Time variations of 1-min AE values are also given in the upper part of Figures 5-2 a - 5-2 e in order to see the degree of AEJ activity.

The distribution of twelve magnetic stations that contribute to the construction of AE indices as well as the location of Albany are shown in Figure 5-3 in geomagnetic coordinates. It should be noted that Great Whale River (GWC) is located in close proximity to the Albany (ALB) meridian. A list of AE (12) stations is given in Table 5-1.

The stations which contributed to AL and AU values and the ranges of AL and AU values for hourly intervals during the five disturbed periods were read from the published plots of the contributing stations and the daily graph of 1-min AL and AU indices [Kamei and Maeda, 1981] and tabulated in Table 5-2 a - 5-2 e.

A. May 4, 1978

The geomagnetic storm began with a sudden commencement at 0828 UT on May 1, 1978. The sky was overcast on the nights of May 2-3 but it was clear over Albany on the night of May 4 (UT). When observations began

TABLE 5-1

Locations of the AE (12) Stations

Stations	Abbreviations	Geographic Lat. (°N)	Geographic Long. (°E)	Geomagnetic Lat. (°N)	Geomagnetic Long. (°E)
Abisko	ABK	68.36	18.82	66.04	115.08
Dixon Island	DIK	73.55	80.57	63.02	161.57
Cape Chelyuskin	CCS	77.72	104.28	66.26	176.46
Tixie Bay	TIK	71.58	129.00	60.44	191.41
Cape Wellen	CWE	66.17	190.17	61.79	237.10
Barrow	BRW	71.30	203.25	68.54	241.15
College	CMO	64.87	212.17	64.63	256.52
Yellowknife	YKC	62.40	245.60	69.00	292.80
Fort Churchill	FCC	58.80	265.90	68.70	322.77
Great Whale River	GWC	55.27	282.22	66.58	347.36
Narssarssuaq	NAQ	61.20	314.16	71.21	36.79
Leirvogur	LRV	64.18	338.30	70.22	71.04

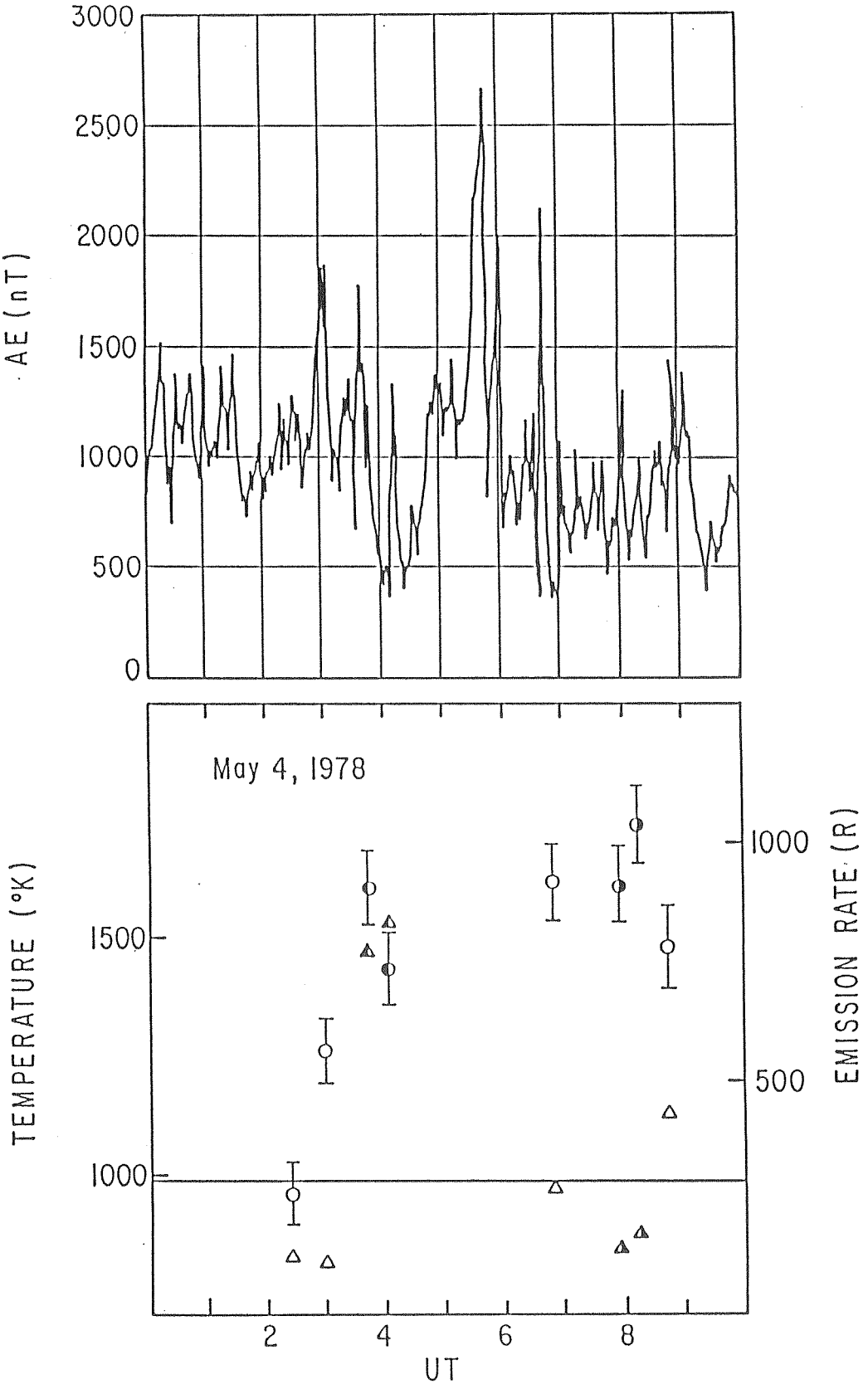

igure 5-2a Time variations of 1-min values of AE index for May 4, 1978 (UT) are shown in the upper panel. In the lower panel measured temperatures (indicated by circles) and 630.0 nm emission rates (indicated by triangles) are grouped into three categories according to the observation zenith angle; (●,▲:$\chi \geq 45°$N, ○,△:$45° \text{N} > \chi < 45°$S, ●,▲:$\chi \geq 45°$S). The solid curve is the least squares fit of the measured temperatures during the quiet periods.

TABLE 5-2a

The stations which contributed to AL and AU and the ranges of AL and AU for hourly intervals on May 4, 1978 (UT)

Time Period (UT)	AL contributing stations	AL range (nT)	AU contributing stations	AU range (nT)
0000-0100	LRV, ABK, TIK	-450~-1300	CMO, BRW	190~440
0100-0200	NAQ, LRV, ABK, YKC	-480~-1190	CMO, CWE	230~420
0200-0300	NAQ, LRV, ABK	-530~-1270	CWE	270~330
0300-0400	NAQ, LRV, ABK	-270~-1540	CWE	220~310
0400-0500	LRV, ABK, GWC, FCC, YKC, CMO, BRW	-200~-1070	DIK, CMO, CWE	150~480
0500-0600	NAQ, LRV, GWC, FCC, BRW	-700~-2500	DIK, CWE	160~310
0600-0700	NAQ, LRV, GWC, CMO, CCS	-240~-1370	DIK, LRV, CWE	0~460
0700-0800	NAQ, GWC, FCC, YKC, CMO, BRW, CWE	-230~-820	DIK, ABK	70~390
0800-0900	GWC, YKC, CMO, BRW, CWE, TIK	-390~-1280	ABK, LRV	50~180

at around 0200 UT on the night of May 4, brightening of the aurora was visible to the naked eye at low elevations in the northern sky. As the night progressed, the aurora became very active. Around local midnight the aurora covered even south of the zenith, and it remained until the end of the observation by morning twilight. The temperature measurements were made by looking north of the zenith before local midnight and by looking at the southern sky after midnight. As seen in Figure 5-2 a, the measured temperatures indicate a rapid increase around 0300 UT. The temperature increased from about 960°K, which is close to the quiet period value, at 0226 UT to about 1610° K at 0344 UT with a rate of about 8° K/min. During the latter half of the observation period, the values of the temperature remained above 1500° K until 0844 UT. The AE value shows quite disturbed conditions throughout the night as seen in Figure 5-2 a.

An examination of the AL index showed that, for the period between 0000 and 0100 UT, the primary contributing station to AL was ABK, which is located approximately 121° east of the ALB meridian. TIK and LRV were AL contributing stations only for a very short duration at the beginning of the period. For the period between 0100 and 0400 UT, the AL contributing station shifted mainly among ABK, LRV and NAO. YKC was also an AL contributing station but for a very short duration around 0130 UT. The first enhanced temperature (~1260° K) was obtained at 0301 UT. NAQ (which is located closest to the ALB meridian in the east, approximately 42° east of it) became an AL contributing station for the periods 0138-0140 UT, 0145-0155 UT, 0210-0211 UT, and 0240-0250 UT, with corresponding AL values

of -600 nT, -480∿-570 nT, -630 nT, and -600∿-800 nT, respectively. When an intensification of AL occurred around 0450 UT the AL contributing station was GWC (which is located closest to the ALB meridian in the west, only 7° west of it). For the period between 0500 and 0700 UT, the AL contributing station shifted mainly between LRV and GWC, east and west of the ALB meridian, respectively. Around 0540 UT, a quite large intensification of AL occurred. The Al contributing station at this time was LRV. FCC, CMO, BRW and CCS occasionally became AL contributing stations but only for a very short duration during this period (0500-0700 UT). For the period between 0700 and 0900 UT, the AL contributing stations shifted mainly between GWC and CWE. NAQ, FCC and TIK occasionally became AL contributing stations but for a very short duration.

The values of AL throughout the night were quite large. They occasionally exceeded 1500 nT, reaching as large as ∿2500 nT at 0545 UT. In summary, before local midnight at ALB the primary AL contributing station shifted from as far east as ABK to GWC, which is in close proximity to the Albany meridian. After local midnight, primary contributing stations were GWC and one of the stations located west of the Albany meridian. The intensity of the westward AEJ was considerably large throughout the night. The position and intensity of the westward AEJ thus appeared to be well reflected on the measured temperatures which showed substantial enhancement over the quiet time value.

The AU contributing station closest to the ALB meridian was CMO, which is still quite distant from it (98° west of it).

The AU values never exceeded 500 nT throughout the night. Therefore, eastward AEJ could not have significant effect in the heating .

B. June 2, 1978

As seen in Figure 5-2 b, the temperatures before 0408 UT did not show any significant enhancement from the quiet time value. The AE values were relatively small, indicating relatively calm condidions before ~0600 UT, and then they began to increase. The temperatures obtained during the period between 0655 and 0726 UT increased from about 1250° K to about 1440° K showing an enhancement amounting to ∿400° K over the quiet time value. Visible aurora was not observed from ALB throughout this night. Therefore, the cause of the temperature enhancements could not be the particle precipitation associated with visible aurora.

The AL value for the period between 0600 and 0800 UT are not so large ($|AL| \lesssim 450$ nT), but the AL contributing stations for this period were mainly GWC and NAQ (GWC for the periods 0600-0630 UT and 0731-0800 UT; NAQ for the period 0630-0727 UT; and YKC for the period 0727-0731 UT). This implies that the location of the maximum intensity of the westward AEJ was in close proximity to the ALB meridian, either in the near east or west of it.

During the same period (0600-0800 UT), the range of AU values was almost the same as that of AL, but the primary AU contributing station was BRW, which is located far west of the ALB meridian (113° west of it). Therefore, the cause of the observed temperature enhancement could not be the Joule heating arising from the the eastward AEJ.

C. June 5, 1978

Although the storm started with SSC at 1211 UT on June 4, the

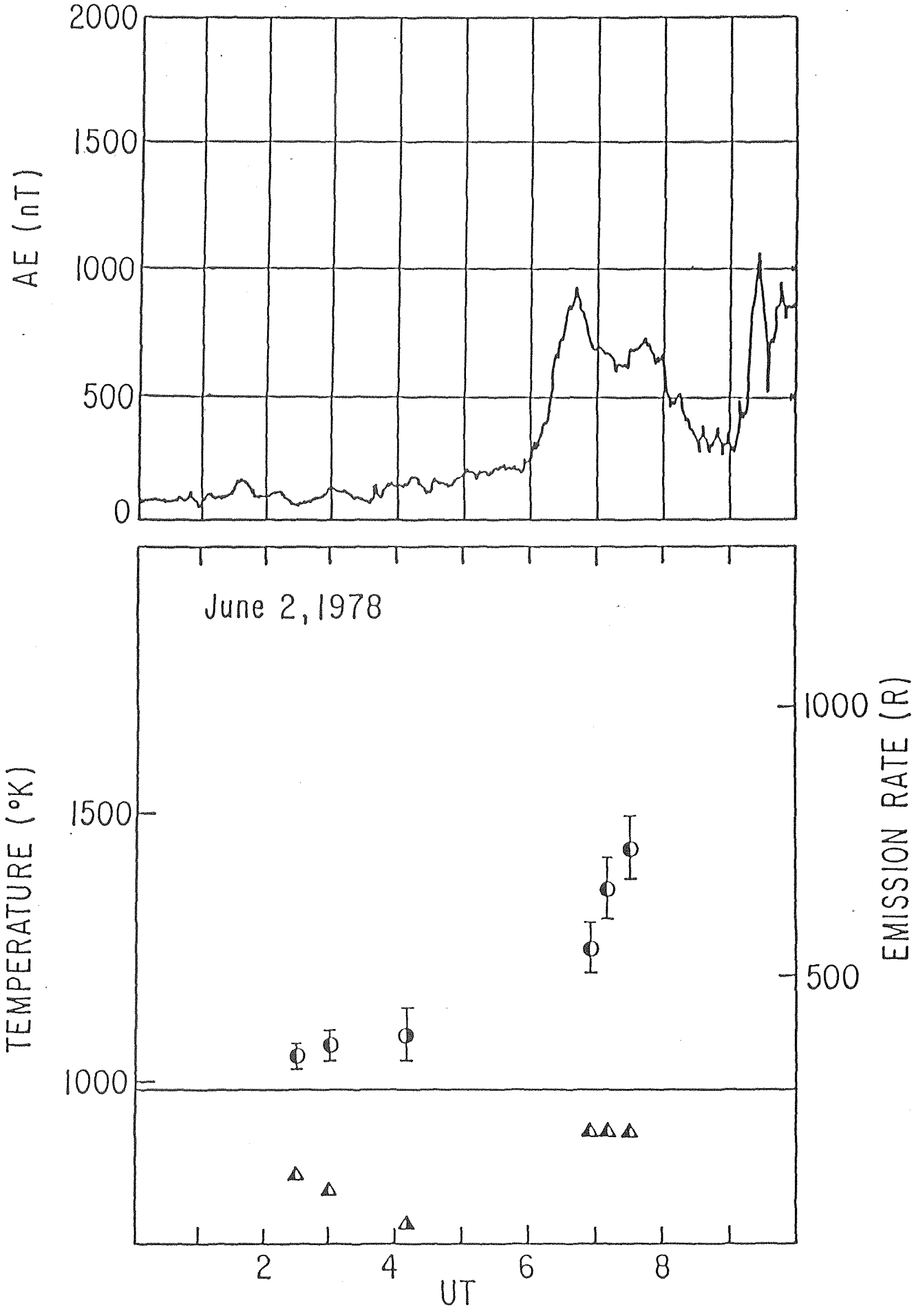

Figure 5-2b same as Figure 5-2a for June 2, 1978 (UT)

TABLE 5-2b

The stations which contributed to AL and AU and the ranges of AL and AU for hourly intervals on June 2, 1978 (UT)

Time period (UT)	AL contributing stations	AL range (nT)	AU contributing stations	AU range (nT)
0000-0100	LRV, BRW, CWE, CCS	- 20~- 30	DIK, NAQ, GWC, FFC, YKC	30~ 60
0100-0200	LRV, BRW, CCS	- 30~- 90	NAQ, LRV, FCC, YKC	30~ 60
0200-0300	LRV, BRW, CCS	- 20~- 60	NAQ, GWC, FCC, YKC, TIK	20~ 80
0300-0400	NAQ, LRV, GWC, BRW, CWE, CCS	- 10~- 90	GWC, FCC, YKC, TIK	40~ 80
0400-0500	DIK, NAQ, CCS	- 60~-130	YKC, BRW, TIK	20~130
0500-0600	NAQ, GWC, FCC	- 70~-130	YKC, BRW	80~130
0600-0700	NAQ, GWC	-120~-450	BRW	130~470
0700-0800	NAQ, GWC, YKC	-300~-430	BRW, CCS	220~340

disturbance was not as great as that of the storm of May 1-4. A faint diffuse aurora was visible in the northern sky around local midnight (0500 UT).

The results of temperature measurements on this night showed that temperatures were moderately enhanced. The temperature, measured in the southern sky at 0421 UT, was about 300° K above the quiet period value. The remainder of the temperature measurements did not show any enhancement greater than 150° K from the quiet period value, even for the measurement made in the middle of diffuse aurora around 0520 UT.

The AL contributing station for the period between 0200 and 0500 UT shifted among NAQ, LRV, and ABK; all of which are located in the east of the ALB meridian. LRV, which is located 77° east of the ALB meridian, contributed to AL for the most part of the period, and NAQ, which is located 42° east of the ALB meridian contributed to AL for the period between 0308 and 0319 UT with corresponding AL values from -570 nT to -670 nT. The temperature enhancement observed at 0421 UT appears to be a reflection of this shifting of the most intense portion of the westward AEJ to the proximity of the ALB meridian. The ranges of AL value were -630 to -930 nT, -530 to -1020 nT, and -520 to -1270 nT for the time intervals of 0200 to 0300 UT, 0300 to 0400 UT, and 0400 to 0500 UT, respectively. For the period between 0500 and 0600 UT, the AL contributing stations shifted widely in longitude from ABK at the easternmost to BRW at the westernmost. A sharp increase in AL around 0520 UT was due to contribution from YKC. The temperature obtained within the faint diffuse aurora at this time showed no enhancement from the quiet period value. GWC contributed to AL

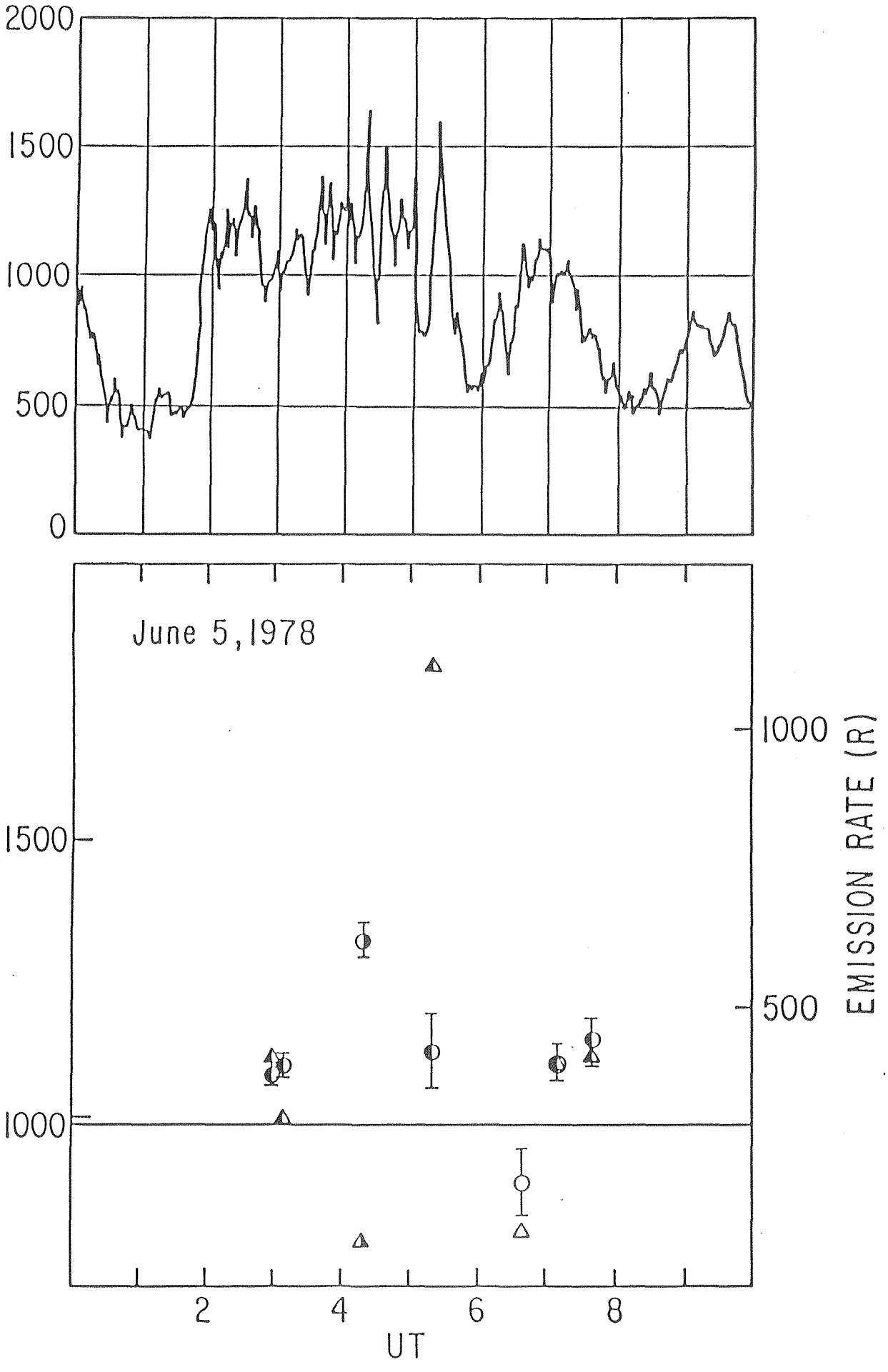

Figure 5-2c same as Figure 5-2a for June 5, 1978 (UT)

TABLE 5-2c

The stations which contributed to AL and AU and the ranges of AL and AU for hourly intervals on June 5, 1978 (UT)

Time period (UT)	AL contributing stations	AL range (nT)	AU contributing stations	AU range (nT)
0000-0100	DIK, ABK, CCS	-220~-600	YKC, CMO, BRW	120~330
0100-0200	NAQ, LRV, ABK FCC	-230~-940	YKC, CMO, BRW	120~320
0200-0300	LRV, ABK	-630~-930	CMO	310~410
0300-0400	NAQ, LRV, ABK	-530~-1020	CMO	310~520
0400-0500	LRV, ABK	-520~-1270	CMO, CWE	270~380
0500-0600	NAQ, LRV, ABK, GWC, FCC, YKC, BRW	-330~-1080	CWE, TIK, CCS	210~500
0600-0700	NAQ, LRV	-370~-870	CMO, CWE, TIK	200~400
0700-0800	NAQ, LRV	-310~-730	CWE, TIK, CCS	260~370

for a very short duration (0530-0535 UT). For the period between 0600 and 0800 UT, the AL contributing station shifted between NAQ and LRV. The values of |AL| during this period did not exceed ~870 nT.

The AU contributing station which was closest to the ALB meridian for the entire period (0200-0800 UT) was CMO, and the AU value never exceeded 520 nT during this period.

D. June 11, 1978

Visible aurora was not seen from ALB on this night. The observed temperatures showed a general decrease throughout the observation period from about 1160° K at 0247 UT. No significant enhancement was seen in the temperature data. The primary AL contributing station was LRV for the period between 0130 and 0525 UT, and NAQ for the period between 0525 and 0700 UT. The maximum value of |AL| for these periods were 570 nT and 180 nT, respectively. During the entire period (0130-0700 UT), the AL contribution station shifted, from time to time, to various locations for only short periods, as shown in Table 5-2 d. GWC became an AL contributing station only for a very short duration (0213-0215 UT). The AL value at this time was about ~-200 nT. Throughout the entire period, the intense portion of the westard AEJ was located far away in the east of the ALB meridian, and the value of AL was modest. These may be the reasons for the lack of significant heating effect in the temperature data. For the entire period, the closest AU contributing station to the ALB meridian was YKC and the value of AU never exceeded 380 nT throughout the period.

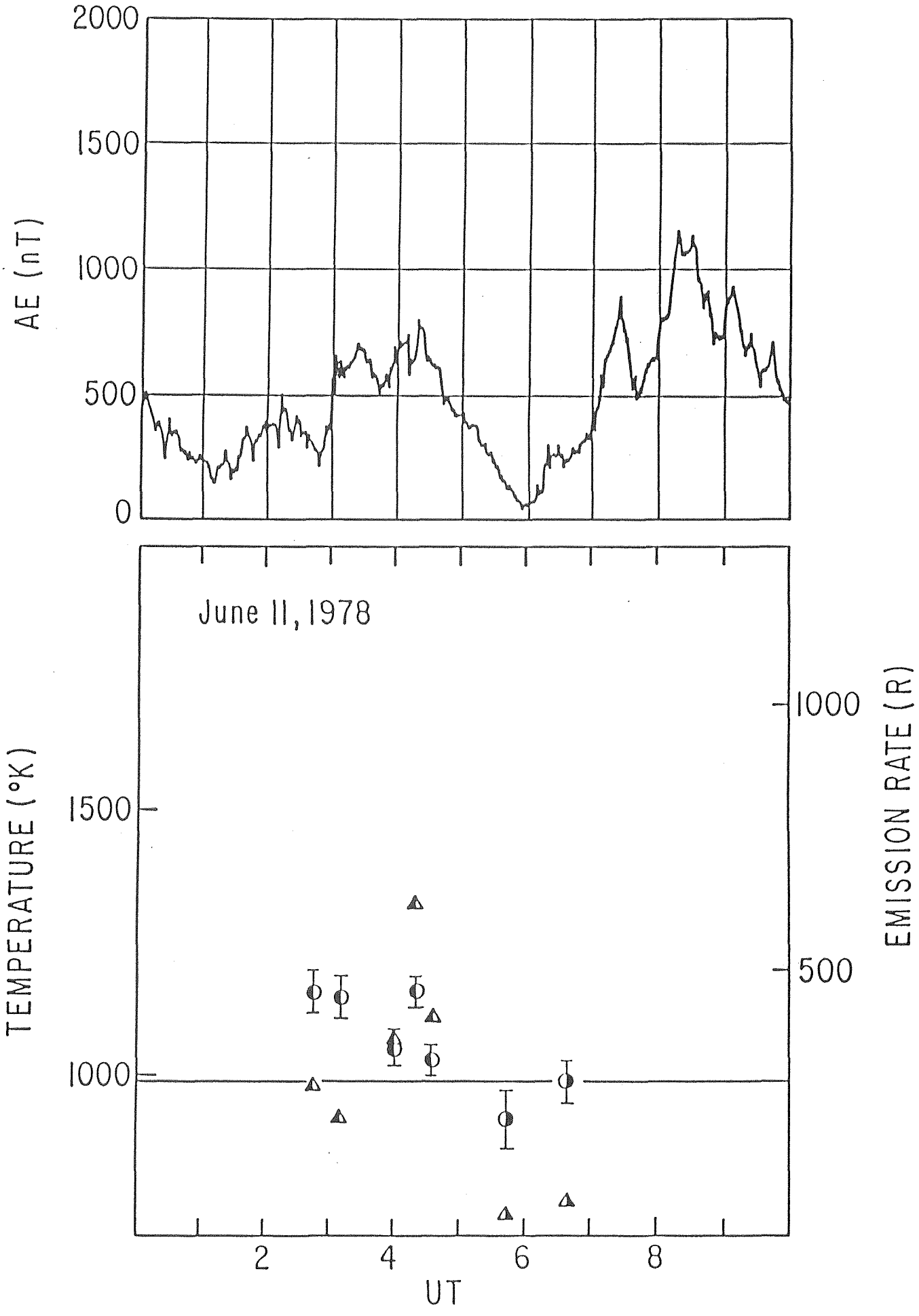

Figure 5-2d same as Figure 5-2a for June 11, 1978 (UT)

TABLE 5-2d

The stations which contributed to AL and AU and the ranges of AL and AU for hourly intervals on June 11, 1978 (UT)

Time period (UT)	AL contributing stations	AL range (nT)	AU contributing stations	AU range (nT)
0000-0100	LRV, ABK	- 90~-470	YKC, BRW	90~210
0100-0200	NAQ, LRV, ABK GWC	- 60~-240	FCC, YKC, CMO, BRW	90~200
0200-0300	NAQ, LRV, ABK, GWC	-160~-290	DIK, YKC, CMO, BRW	70~330
0300-0400	NAQ, LRV, FCC	-240~-430	CMO, BRW	170~380
0400-0500	NAQ, LRV	-320~-570	CMO	100~280
0500-0600	NAQ, LRV, DIK, CCS	- 30~-330	YKC, CMO, BRW	20~110
0600-0700	NAQ, LRV, CCS	- 20~-150	LRV, DIK, CMO, BRW, TIK, CCS	20~210

E. June 30, 1978

The AE indices were large (AE $\gtrsim$ 500 nT) during the period between 2100 UT on June 29 and 0100 UT on June 30 and then subsided. The AE indices began to increase again around 0545 UT, after when the diffuse aurora was seen from ALB in the northern sky. The temperatures measured in the southern sky at 0233 UT and 0247 UT were about 1010° K and 1120° K, respectively and did not show any significant heating effect.

There was an abrupt decrease in the AL value (intensification of the westward AEJ) around 0545 UT. The value of |AL| remained above 400 nT until 0730 UT; the value reached 620 nT around 0615 UT with the primary contributing station at that time being GWC. For the period after the onset of the AEJ intensification (0545-0730 UT), the AL contributing station shifted among LRV, NAQ, GWC, FCC, and YKC; indicating that the westward AEJ extended across the ALB meridian. GWC became the AL contributing station for the period 0440-0605 UT and 0612-0617 UT. The corresponding temperature measured in the northern sky at 0723 UT was substantially increased to 1380° K. However, the temperature obtained at 0609 UT was only about 1090° K. Although this was measured within the diffuse aurora, it was not significantly enhanced from the quiet time value. This implies that the heating effect produced by the AEJ is much more effective than that produced by particle precipitation and that there is a time lag between the intensification of the AEJ and the temperature enhancement observed from ALB, which is located equatorward of the AEJ.

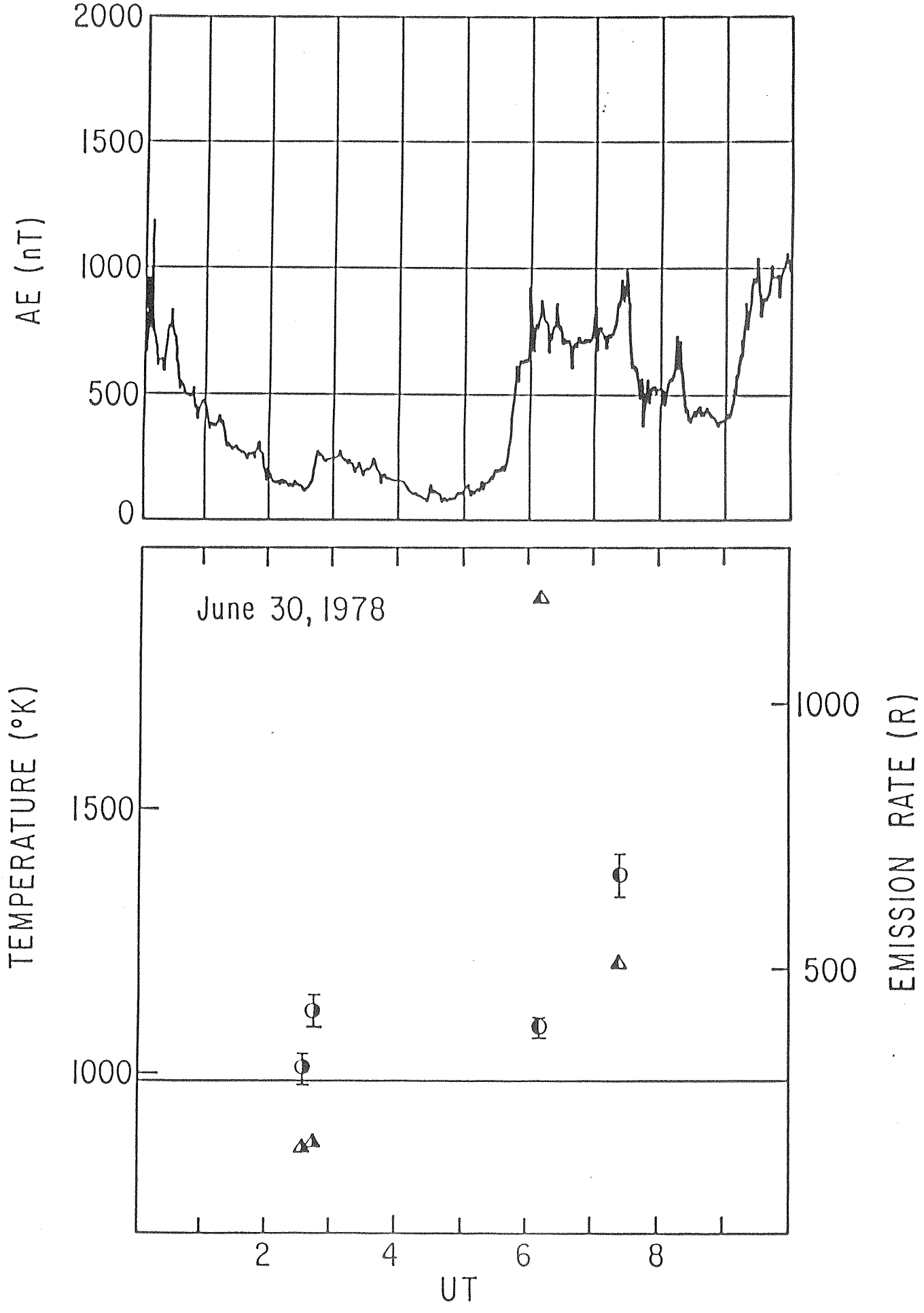
2000
1500
1000
500
0
AE (nT)
June 30, 1978
TEMPERATURE (°K)
1500
1000
1000
500
EMISSION RATE (R)
2
4
6
8
UT

TABLE 5-2e

The stations which contributed to AL and AU and the ranges of AL and AU for hourly intervals on June 30, 1978 (UT)

Time period (UT)	AL contributing stations	AL range (nT)	AU contributing stations	AU range (nT)
0000-0100	ABK, DIK, CCS, TIK	-190~-780	YKC	230~440
0100-0200	ABK, BRW, CCS	- 90~-230	YKC	90~200
0200-0300	LRV, ABK, FCC, CMO, BRW	- 70~-190	DIK, YKC	60~ 90
0300-0400	NAQ, LRV	-120~-190	GWC, YKC	30~ 90
0400-0500	NAQ, LRV, FCC, TIK, CCS	- 70~-120	ABK, DIK, YKC, CMO	10~ 40
0500-0600	NAQ, LRV, ABK, GWC, FCC	- 70~-450	CMO, CCS	20~260
0600-0700	NAQ, LRV, GWC, FCC, YKC	-400~-620	CMO, BRW, CCS	210~330
0700-0800	NAQ, GWC	-210~-590	CMO, BRW, CCS	180~390

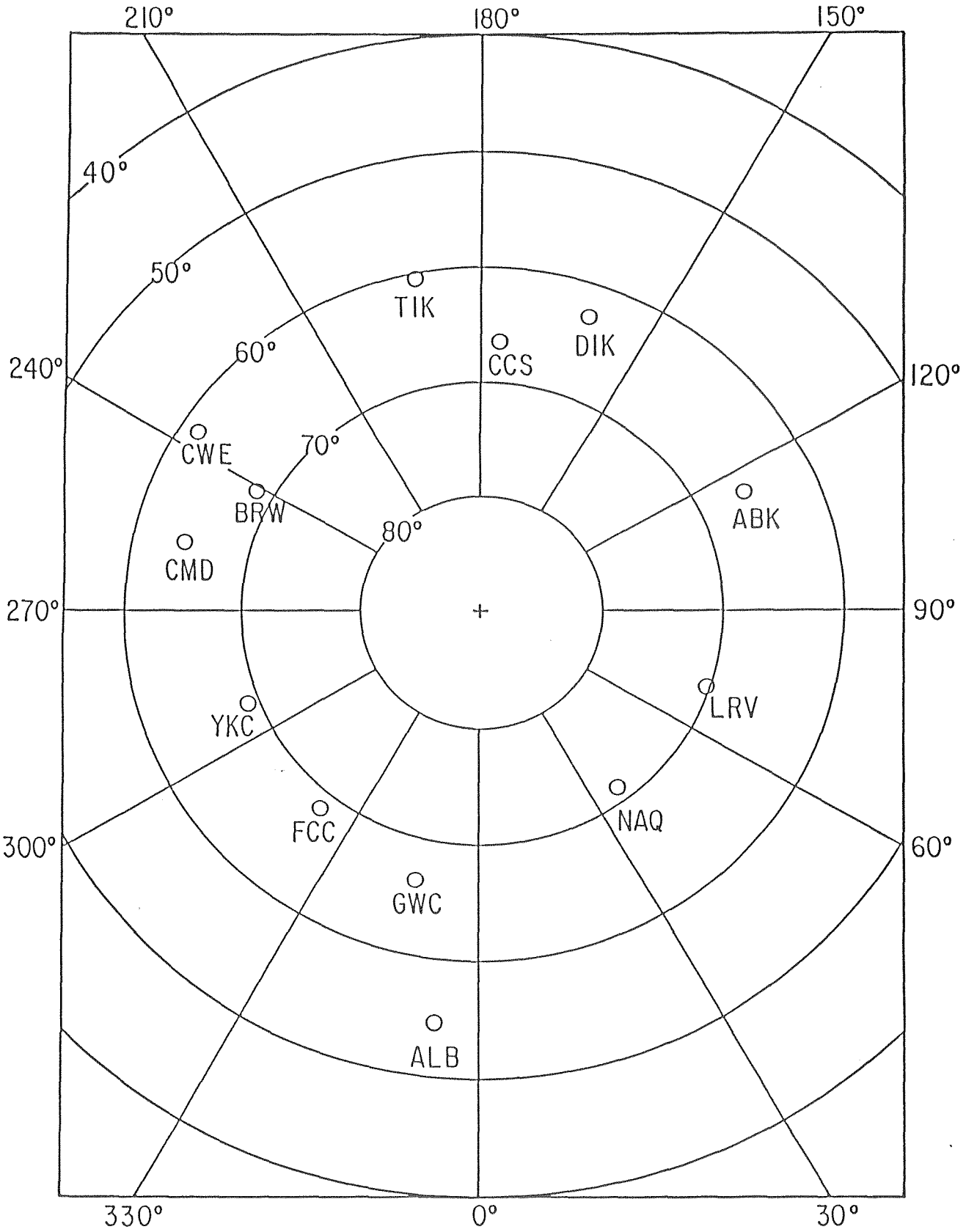

Figure 5-3 Locations of AE(12) stations and Albany in geomagnetic coordinates. Also see Table 5-1 for abbreviated names and coordinates of the stations.

GWC became an AU contributing station at 0319 UT but only for one minute. However, the AU value at that time was as low as 60 nT. Except for GWC, the AU contributing station which was closest to the ALB meridian for the period between 0545 to 0730 UT was CMO. The AU value never exceeded 400 nT for this period.

Discussion

The results of our measurements of the thermospheric response to AEJ activity made during the five geomagnetically disturbed periods can be categorized into the following two groups:

(A) GWC became the primary AL contributing station during the period preceding the temperature enhancement. This implies that the most intense portion of the westward AEJ was located in the close vicinity of the ALB meridian during this period. This group includes:

(a-1) After local midnight (0500 UT) on May 4, 1978, GWC was, from time to time, the primary AL contributing station and the values of |AL| occasionally exceeded 1500 nT, reaching ~2500 nT at one instance. The corresponding temperatures obtained between 0648 and 0844 UT showed significant enhancements ranging ~500- ~750° K over the quiet time value.

(a-2) During the period between 0600 and 0630 UT on June 2, 1978 GWC was the AL contributing station with the values of |AL| less than 450 nT. The corresponding temperatures obtained

between 0655 and 0726 UT showed substantial enhancements amounting to ~400° K over the quiet time value, even though the AL values were not very large.

(a-3) During the periods between 0550 and 0605 UT, and 0612 and 0617 UT on June 30, 1978, GWC was the AL contributing station with values of |AL| ranging 450-620 nT. The corresponding temperatures obtained at 0723 UT showed an enhancement of ~400° K over the quiet time value.

(B) GWC was not the primary AL contributing station. Instead, stations far away from the ALB meridian, such as NAQ or LRV, became the primary AL contributing stations during the period preceding the temperature enhancement. This implies that the most intense portion of the westward AEJ was located far away from the ALB meridian during this period. This group includes:

(b-1) During the period between 0138 and 0250 UT on May 4, 1978, NAQ became the AL contributing station four times with values of |AL| ranging 480-800 nT. The corresponding temperatures obtained between 0301 and 0403 UT showed enhancements ranging ~300- ~600 K over the quiet time value.

(b-2) During the period between 0308 and 0319 UT on June 5, 1978, NAQ became the AL contributing station with values of |AL| ranging 570-670 nT. The corresponding temperature obtained at 0421 UT showed an enhancement

of ~300° K over the quiet time value.

(b-3) During the period between 0130 and 0535 UT on June 11, 1978, LRV was the primary AL contributing station with the values of |AL| not exceeding ~570 nT. For the period between 0525 and 0700 UT, NAQ became the primary AL contributing station with the values of |AL| not exceeding ~180 nT. The temperatures obtained throughout this night did not show any significant enhancement.

From the results listed above, we can draw the following conclusions

(a) When the most intense portion of the westward AEJ is located at GWC, which is in close proximity to the ALB meridian, for a considerable duration, the Joule heating produces a temperature enhancement of at least 400° K of the thermospheric region in the field of view from ALB, even if the values of |AL| is as moderate as ~450 nT. When the intensity of the westward AEJ is quite large, the temperature enhancement becomes as high as ~750° K.

(b) The Joule heating effect observable in the field of view from ALB is not very large when the most intense portion of the westward AEJ is located at NAQ or LRV, which is far away from the ALB meridian. To produce a temperature enhancement of ~300° K, a value of |AL| greater than 500 nT is required for a considerable duration if NAQ is the primary contributing station. A value of |AL| greater than ~500 nT cannot produce any significant temperature enhancement if the primary AL contributing station is

LRV, which is located even further east of NAQ from the ALB meridian.

(c) There is a definite time lag of an order of one hour between the intensification of the westward AEJ and the measured temperature enhancement. Another interesting point of our observation is that the temperatures obtained within the aurora whose intensity of the 630.0 nm emission is greater than 1 KR, did not show any significant enhancements. This implies that the heating produced by particle precipitation is not as effective as the Joule heating.

CHAPTER VI

Thermospheric Temperatures during the July 5, 1978 Storm: A Possible Existence of the Nonthermal Atomic Oxygen

In this Chapter we describe the detailed results of the [OI] 630.0 nm line profiles which were observed during the magnetic storm of July 5, 1978.

The [OI] 630.0 nm profiles observed around 0700 UT which showed the most increased "apparent temperatures", could not be interpreted in terms of a single Gaussian source profile. Instead, a combination of two Gaussian source profiles satisfactorily explained the observed results. This, together with unusually high intensity at the time of the observation, suggests that the [OI] 630.0 nm emission consisted of two different components, each being originated from a different source.

Results

The storm began with an SSC at 2305 UT on July 3. The values of the K_p index during the measurements on the night of July 5 were 7 and 7- (Figure 6-1). When photometric observation began around 0200 UT, an auroral display was already visible to the naked eye in the northern sky. The beginning of the interferometric observation was delayed due to a power problem. The aurora became quite active during the course of the night. From approximately 0430 UT, the aurora showed a ray structure in the northern sky, stretching its visible limit even to south of zenith. The aurora on this night was very pronounced, and it did not weaken until the morning twilight.

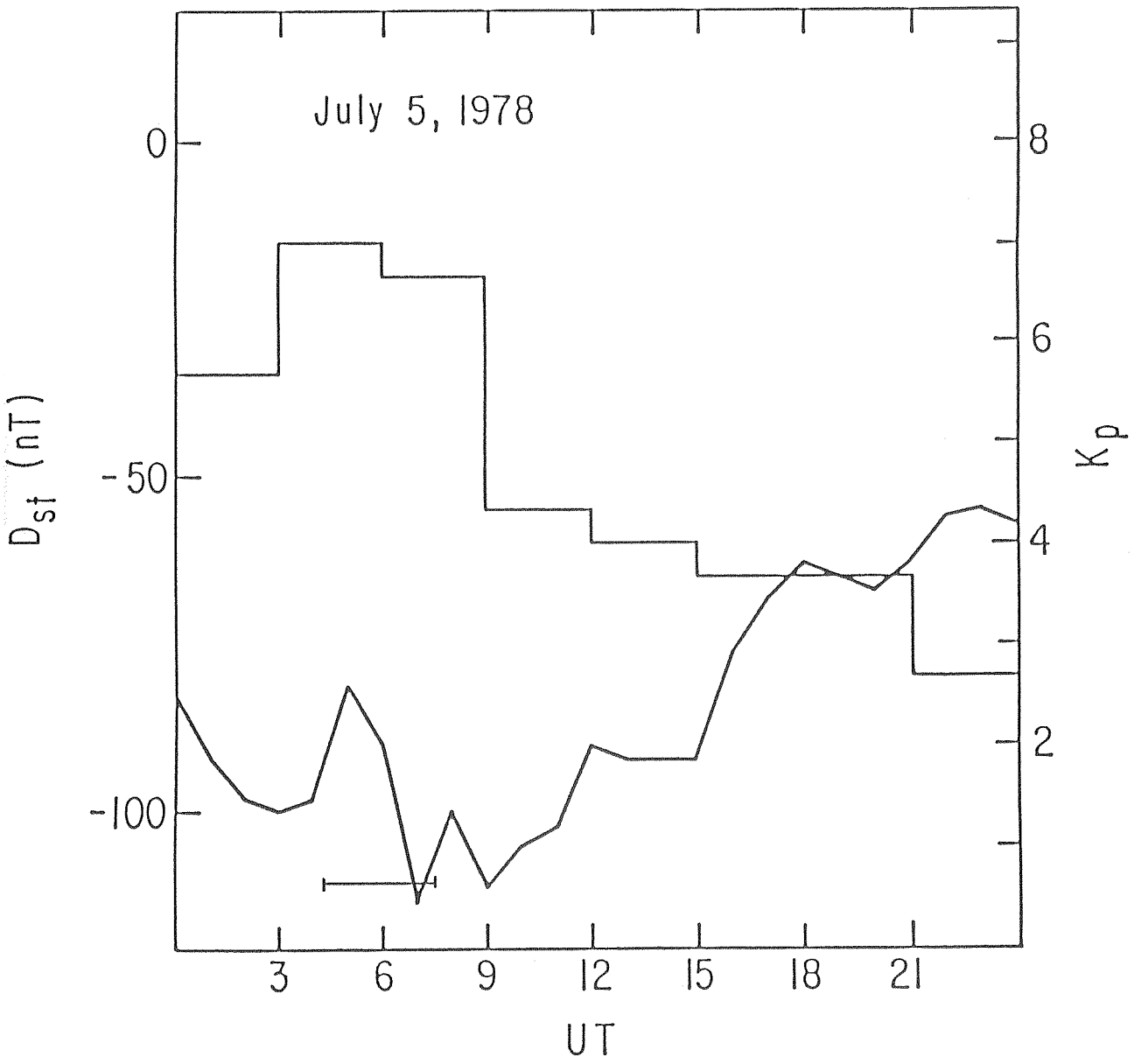

Figure 6-1 Three hourly planetary geomagnetic indices K_p and values of D_{st} for the geomagnetic storm on July 5, 1978. The observation period for temperature measurements are indicated by a horizontal bar.

The method of analysis described in Chapter 2, which provides the Doppler temperature as well as the 630.0 nm line intensity and the background continuum, was initially applied to the observed data. The first measured temperature looking south of zenith was about 1800° K around 0420 UT, which was enhanced as much as 800° K from the quiet period value. Eight additional temperatures were obtained during the period between 0500 and 0730 UT. During this period, the temperatue derived with the method of analysis mentioned above show values consistently greater than 2000° K, with the maximum value of 2610° K at 0710 UT. However, the data indicated by the asterisks shown in Figure 6-2 and 6-3, taken between 0710 and 0726 UT, give negative values of the background continuum, indicating that the analysis method is inadequate for these cases. As an example, the profile obtained at 0710 UT, from which the maximum "apparent temperature" was derived with the present analysis scheme, is shown in Figure 6-4 by dots.

The dashed curve drawn through the dots is the theoretical profile that is a convolution of the instrument function and the single Gaussian function having the source temperature of 2610° K; this theoretical profile provides the best fit to the observed fringe. The solid curve inside the theoretical curve is the theoretical instrument function calculated from the four instrumental parameters which were obtained from calibration scans made before and after the observation. As stated before, this analysis technique provides background continuum along with the temperature. The background continuum obtained for this theoretical profile is -54 counts (dashed line in the figure). Since the derived background continuum is negative for this

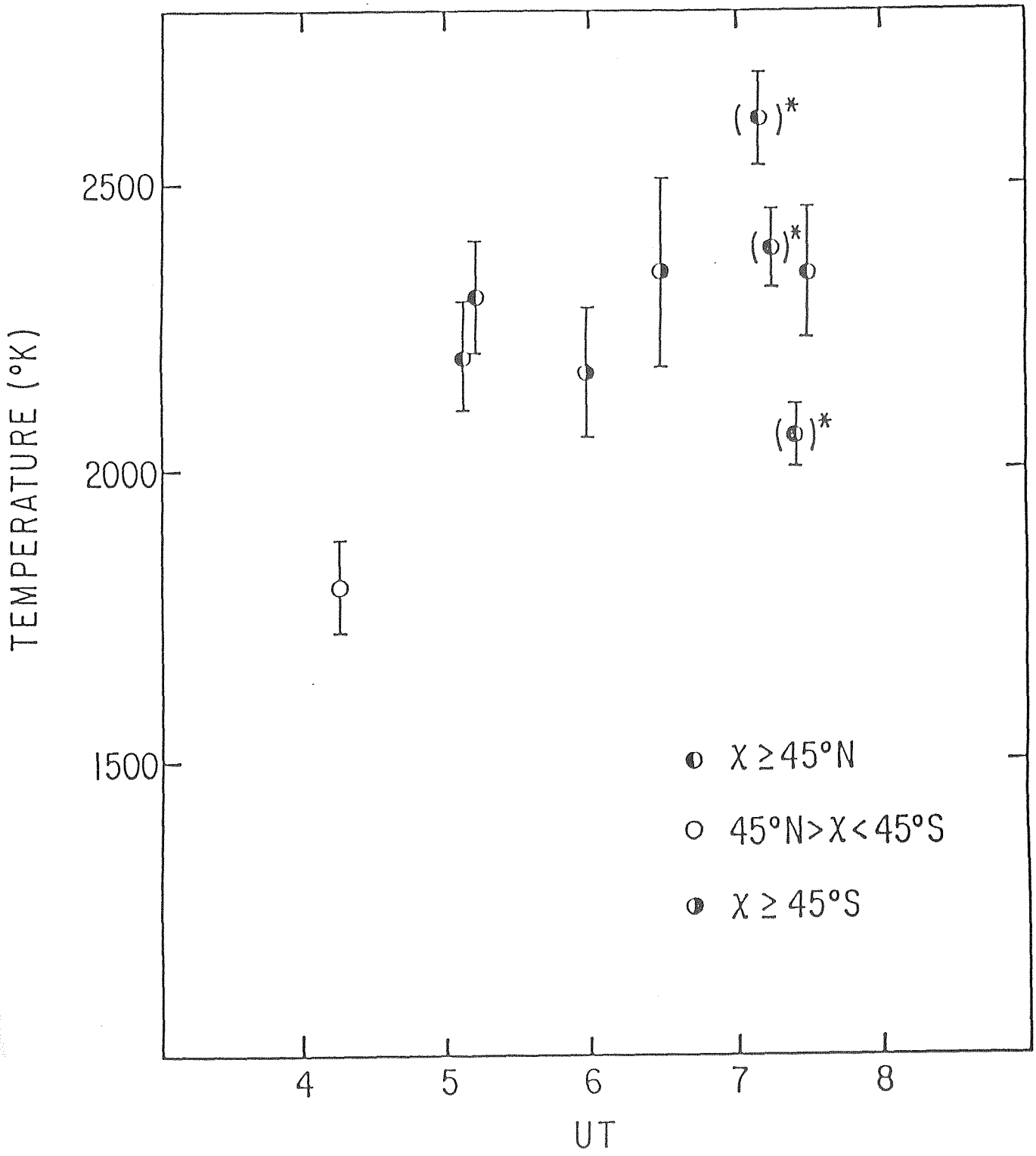

Figure 6-2 Temperatures derived from [OI] 630.0 nm Doppler line profiles during the geomagnetic storm periods on July 5, 1978 as a function of universal time. The open and half shaded symbols indicate the direction (zenith angle:χ) in which the measurements were made in the meridian plane.

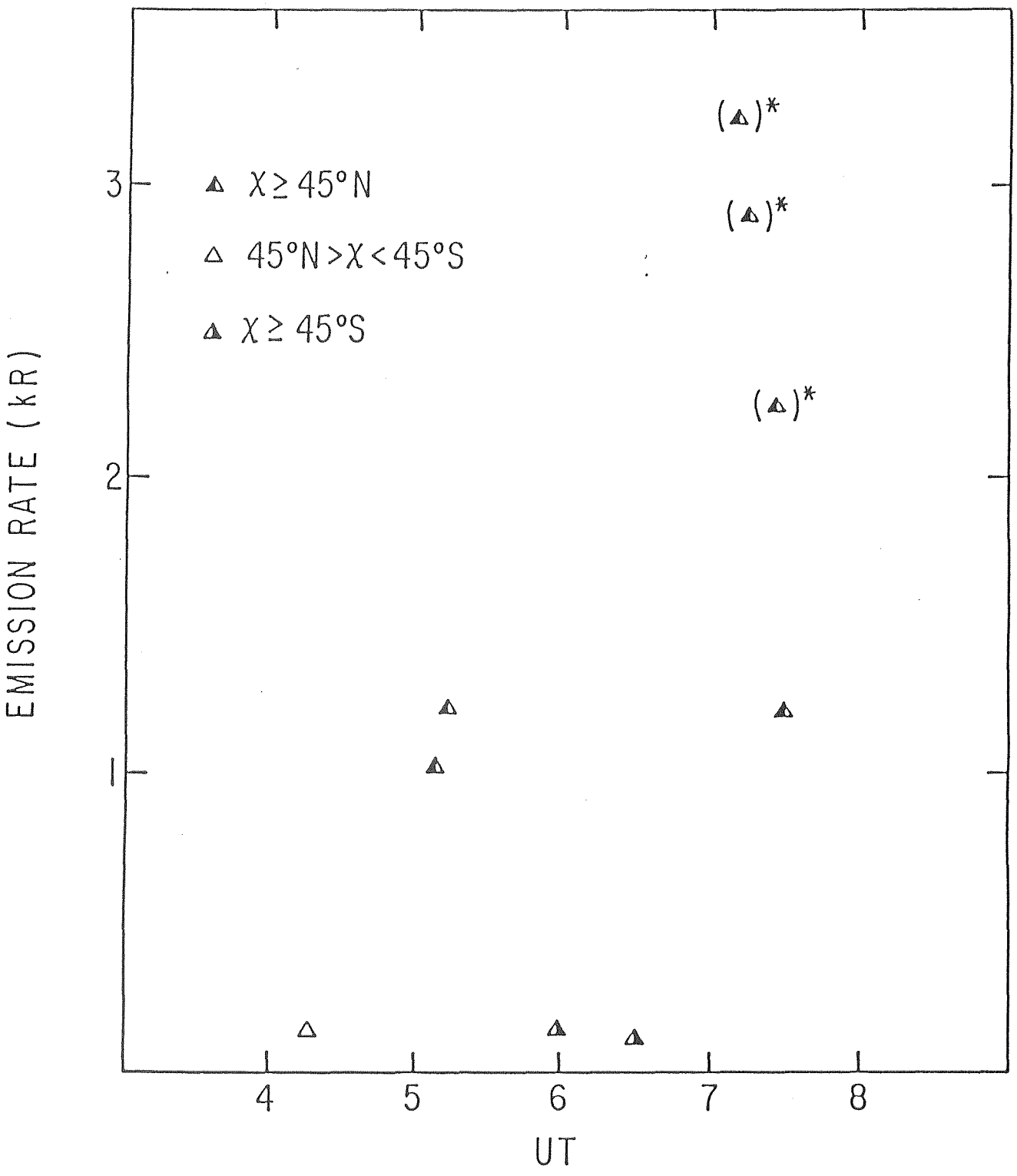

Figure 6-3 The emission rate of [OI] 630.0 nm line measured by the Fabry-Perot interferometer as a function of universal time on July 5,1978. The open and half shaded symbols indicate the direction (zenith angle:χ) in which the measurements were made in the meridian plane.

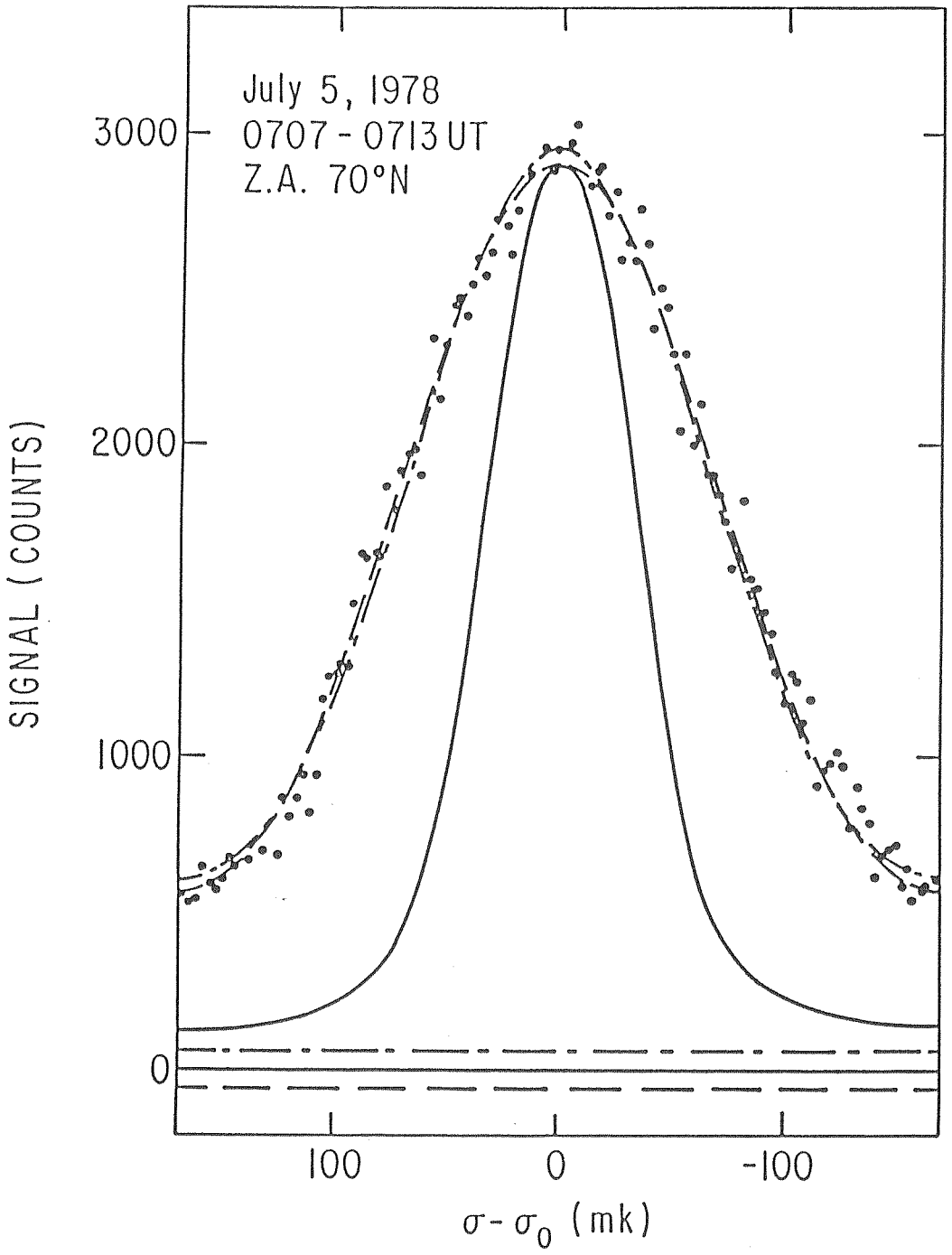

Figure 6-4 Observed 630.0 nm line profile at 0710 UT on July 5, 1978 is shown by dots. The inner-most solid curve is the instrument function of the interferometer. The dashed curve is the best-fit theoretical profile that is a convolution of the instrument function and the single Gaussian function corresponding to the source temperature of 2610° K. The background continuum obtained for this theoretical profile is negative (-54 counts) and is shown by the dashed line. The dash-dotted curve is the theoretical profile calculated from the convolution of the instrument function and the combination of the Gaussian function for a source temperature of 1800° K and the function for T' = 3900° K and k = 0.32. The background continuum obtained from this theoretical curve, 63 cps, is also shown by a dash-dotted line.

case, it is apparent that the single Gaussian source function cannot explain the observed profile, although it appears to be a good fit as seen in the figure. The background continuum for this case should be in the range of 20-70 counts, taking the gate time for this observation (1 sec) into account. Therefore, instead of a single Gaussian function, a combination of two Gaussian functions, each corresponding to a different source temperature, T and T', was taken as a source function. This new source function was used to provide a theorectical profile by a convolution with the instrument function.

In this attempt, it became obvious that a unique combination of two different Gaussian functions cannot be found unless one of them is given apriori. Therefore, we took here the value of T = 1800° K for the first component. The reasons for taking this value are: (1) the first observed profile on this night gives the temperature of 1800° K, along with a reasonable background continuum, and (2) such an elevated temperature could be realistic during a severe geomagnetic storm like the one reported here [e.g., Hernandez and Roble, 1978]. After one of the temperatures was fixed at 1800° K, values of R (T,T') the residual between the smoothed observed profiles and the theoretical profile, which is an integration for one period of the squares of difference between those two profiles, were calculated by changing the temperature, T', and the weight, k, of the second component.

As for the two component source, one at temperature T' with weight k and the other at temperature T with weight (1-k), the equations (2-43) and (2-44) are slightly modified into the form:

$$R(T,T') = \sum_{m=1}^{4} Y_m^2 - \frac{\sum_{m=1}^{4} A_m Y_m \exp\{-\frac{m^2}{4}\gamma(1-k)T\}\exp\{-\frac{m^2}{4}\gamma kT'\}}{\sum_{m=1}^{4} A_m^2 \exp\{-\frac{m^2}{4}\gamma(1-k)T\}\exp\{-\frac{m^2}{4}\gamma kT'\}} \qquad (6\text{-}1)$$

$$\text{and } I_o' = \sum_{m=1}^{4} A_m Y_m \exp\{-\frac{m^2}{4}\gamma(1-k)T\}\exp\{-\frac{m^2}{4}\gamma kT'\}[\sum_{m=1}^{4} A_m^2 \exp\{-\frac{m^2}{2}\gamma(1-k)T\}$$

$$\exp\{-\frac{m^2}{2}\gamma kT'\}]^{-1}$$

$$\text{and } C' = \frac{Y_{co}}{2} - A_o I_o' \qquad (6\text{-}2)$$

The results are shown in Figure 6-5. The solid curves shown in the figure indicate the variation of the residual, R(T,T') as functions of T' with fixed value of T = 1800° K and with k as a parameter. The hatched area in the figure indicates that the value of the background continuum, C' which was calculated from equation (6-2), is in the range 20-70 cps which is reasonable for our instrument. The right boundary of the hatched area gives values of the background continuum less than 20 cps, including negative values, while the left boundary gives values greater than 70 cps. The dash-dotted line in the figure connects points giving the minimum residual value at each weight. From the figure, it can be seen that

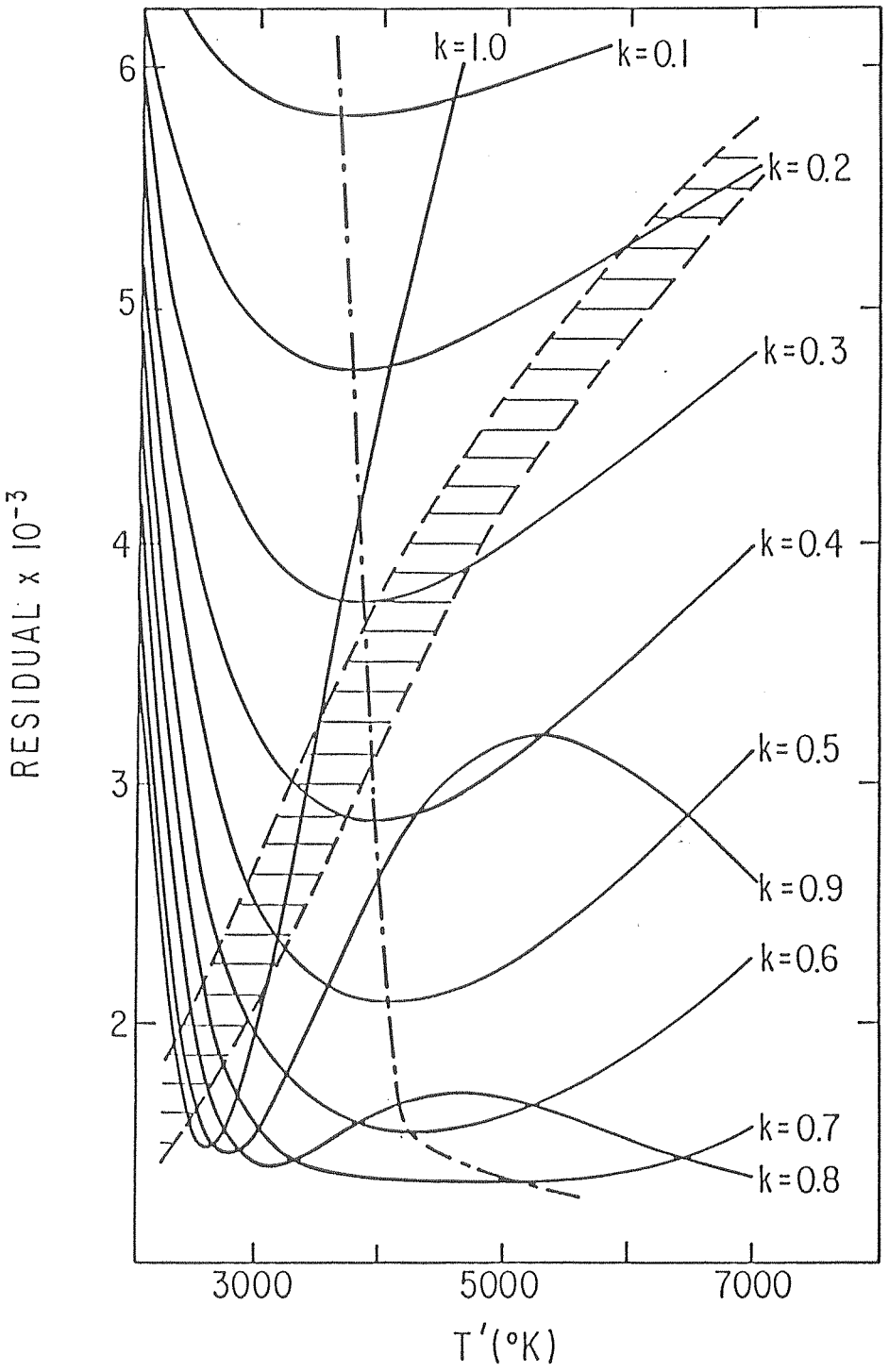

Figure 6-5 Calculated residual between the smoothed observed profile obtained at 0710 UT on July 5, 1978 and the theoretical profile. Residual is an integration for one period of the squares of difference between those two profiles. The theoretical profile is the convolution of the instrument function and a combination of two Gaussian functions, each corresponding to a different source temperature, T and T'. The residual is plotted as a function of the source temperature T' and the weight k of the second component. The source temperature of the first component is fixed at 1800° K. The dash-dotted line connects points giving the minimum residual value at each weight. The hatched area gives reasonable values for the background continuum, i.e., 20-70 counts per second.

a combination of the Gaussian function for a source temperature of 1800°K and the function for T' = 3900°K and k = 0.32 yields a minimum value of residue and also a reasonable value for the background continuum. Therefore, this combination of the two Gaussian functions explains the observed profile at 0710 UT satisfactorily. The theoretical curve calculated from the convolution of the above two-component Gaussian profile and the instrument function is shown in Figure 6-4 by the dash-dotted curve. The background continuum obtained from this theoretical curve, 63 cps, is also shown in the figure by a dash dotted line.

Discussion

The widths of some of the 630.0 nm line profiles observed during the July 5, 1978 storm period are unusually large. This can be easily recognized by comparing the observed data in Figure 6-4, and Figure 5-1. These figures also show that the instrumental width remained almost the same for these two measurements. The observed data shown in Figure 6-4, in addition to the rather large counting rates, show good symmetry, indicating that there is no distortion due to the emission intensity change during the scan. Therefore, we believe that the large width of the observed data is a real reflection of the source profile. However, as stated before, this observed profile gives the apparent temperature of 2610° K if a single Gaussian source function is assumed. Such a high thermospheric temperature seems unlikely. Furthermore, the analysis scheme using a single Gaussian source function gives the negative background continuum (Figure 6-4), indicating the analysis method is inadequate for this case.

In an attempt to explain the observed profile at 0710 UT which shows unusually large width (Figure 6-4), we used a combination of two different Gaussian functions as a source profile. Calculations show that a combination of the function for a source temperature of T = 1800° K and the function for T' = 3900° K = 0.32 yields a minimum value of residue and also a reasonable value for the background continuum (Figure 6-5). Therefore, this combination of the two Gaussian functions explains the observed profile at 0710 UT satisfactorily. This implies that the [OI] 630.0 nm profile obtained at 0710 UT during the geomagnetic storm of July 5, 1978 consists of two different components, each originating from a different source. In our calculations, we took T = 1800° K for the temperatue of the first component. If a different value was used as the temperature of the first component, a different value of the temperature and weight of the second component would result. In addition, it is not guaranteed that the second component has a Gaussian shape. The analysis reported here for the measurement at 0710 UT on July 5, 1978 should be considered exploratory. Nevertheless, it is indisputable that the observed data has unusually large width, and that a single Gaussian source function cannot explain the observed data.

As pointed out by Hernandez [1974 a], the possibility of the contamination of the 630.0 nm line by the nearby rotational lines of OH (9-3) band might complicate the temperature determination. However, for the measurements reported here, the possibility of apparent temperature increases due to OH contamination is rejected by the especially large enhancement of the 630.0 nm emission rate resulting from auroral activity. Also, with the

spacer of our interferometer, the effect of OH contamination would appear as a bump between the two consecutive 630.0 nm line profiles.

In view of the fact that visible auroral activities were seen in the northern sky during times of our observation, temperature enhancements might be caused by heating, as a result of precipitating energetic electrons as well as by Joule heating. However, our data show that large temperature enhancements were also seen at low elevation angle in the southern sky where no visible auroral activities were observed.

The energy flux of energetic O^+ ions (0.7-12 KeV) measured during geomagnetic storms was as great as 0.4 erg/cm^2 sec ster [Shelley et al., 1972], with 0.1 erg/cm^2 sec ster being frequently measured. The observations also showed that the nightside O^+ ion fluxes were 5-10 times larger than those on the dayside [Sharp et al., 1976 a]. The dynamic response of the thermosphere to energetic O^+ ion precipitation has been extensively investigated by Torr et al. [1982], using the O^+ ion flux as an input to the NCAR TGCM model. This input flux was scaled down by 2π from the one observed during the December 16/17, 1971 magnetic storm [Shelley et al., 1972]. The measured peak flux of 0.4 erg/cm^2 sec ster was so large that they had difficulty in carrying out the calculations smoothly. Even for this scaled down energy influx, the work by Torr et al. [1982] revealed that the maximum temperature increase due to O^+ heating can be as high as almost 800° K. Their results also showed that the production rate of energetic oxygen atoms produced by charge exchange and momentum transfer between energetic O^+ and ambient O peaks at around 500 km. According to Torr et al. [1974], a surface brightness of 630.0 nm emission amounting to 200 R

is expected for the energetic O^+ flux spectrum observed by Shelley et al. [1972], assuming that each charge exchange results in an excited oxygen atom that yields a 630.0 nm photon. Observational results also show that the latitudinal range of the flux of these fast O^+ ions overlaps and extends equatorward of the auroral electron region [Sharp et al., 1974; 1976 b]; indeed this is the latitudinal region where our observations were made. In addition, Yee et al. [1980] reported the existence of an atomic oxygen corona overlying the thermosphere during the solar maximum period from a series of twilight interferometric observations of the near infrared O^+ (^2P) doublets at 732 and 733 nm. They detected excessive amounts of emission at shadow heights above 550 km, and the scale height deduced from the vertical brightness profile showed a marked increase above 550 km, estimating the equivalent temperature to be 4000° K or higher. Additional evidence of such elevated equivalent temperature is seen in the interferometric profile of 732 nm emission line. By fitting a Gaussian, they deduced an equivalent temperature of 4300 ± 1500° K. It is apparent from these reports that there exists nonthermal O atoms above 500 km altitude region.

Therefore, we believe that the [OI] 630.0 nm profiles observed between 0710 and 0726 UT during the geomagnetic storm of July 5, 1978 consist of two different components, one originating from the F region and the other from the nonthermal O atams at an altitude greater than 500 km. Large intensities of the profiles observed during this period (Figure 6-3) also support this interpretation.

PART II Stable Auroral Red (SAR) Arc

CHAPTER VII

Photometric and Interferometric Observations of the SAR Arc Event of September 25/26, 1978

Since the discovery of stable auroral red arcs (SAR arcs) by Barbier [1958] during the IGY years, many workers have reported a number of SAR arc events covering the past two solar cycles. Rees and Roble [1975] summarized the results of observations and theories in their review paper.

From the observations spanning the past two decades, it seems clear that the frequency of occurrence of the SAR arc is positively correlated with solar activity [Slater and Smith, 1981]. During the solar cycle 20, the last event of the SAR arc was reported by Carman et al. [1976] on April 1/2, 1973; then the occurrence appeared to cease. A reappearance of the SAR arc had been strongly expected at mid-latitudes during geomagnetically disturbed periods as a new sunspot maximum approached.

On the night of September 25/26, 1978 a distinct SAR arc appeared. Although, an arc occurred earlier on April 30/May 1, 1978, the records indicate that the arc on September 25/26 was very distinct. Therefore, the results of the photmetric and interferometric measurements of the SAR arc observed on the night of September 25/26, 1978 are presented in this chapter.

Results

Both the photmetric and the interferometric observations were begun at 0000 UT on September 26, 1978. The sky condition was clear on that night. Until 0300 UT when auroral activities started in the northern sky, the intensity of [OI] 630.0 nm emission had been gradually increasing from its normal value. Following the appearance of auroral activities, the meridional photometer records of 630.0 nm indicated a bulge at a zenith angle of 51° north, superimposed upon the background slope due to northern auroral activities at 0450 UT. This bulge grew very rapidly to a well defined SAR arc in less than 20 minutes. The arc persisted throughout the rest of the night until observation was ceased due to morning twilight.

After the appearance of the SAR arc, northern auroral activities became quite visible but were well separated from the SAR arc, and also persisted throughout the rest of the night. The zenith angles of the position of the peak intensity and those of the position of the half-max intensity were measured on the photometer records, and plotted against universal time (Figure 7-1). There is a systematic equatorward movement throughout the period of observation. Assuming the altitude of the arc to be 400 km [Roach and Roach, 1963; Old et al., 1972; Smith et al., 1972], the average velocity of equatorward movement of the arc was 240 km/hr and the half-max intensity widths range from 150 km to 260 km. The positions of the peak intensity were transformed into L value intercepts at 400 km using the following relations

$$L = \frac{R_E + h}{R_E \cos^2 \lambda_m} \tag{7-1}$$

$$\lambda_m = \lambda_{mo} + \chi - \sin^{-1} \left(\frac{R_E \sin \chi}{R_E + h}\right) \tag{7-2}$$

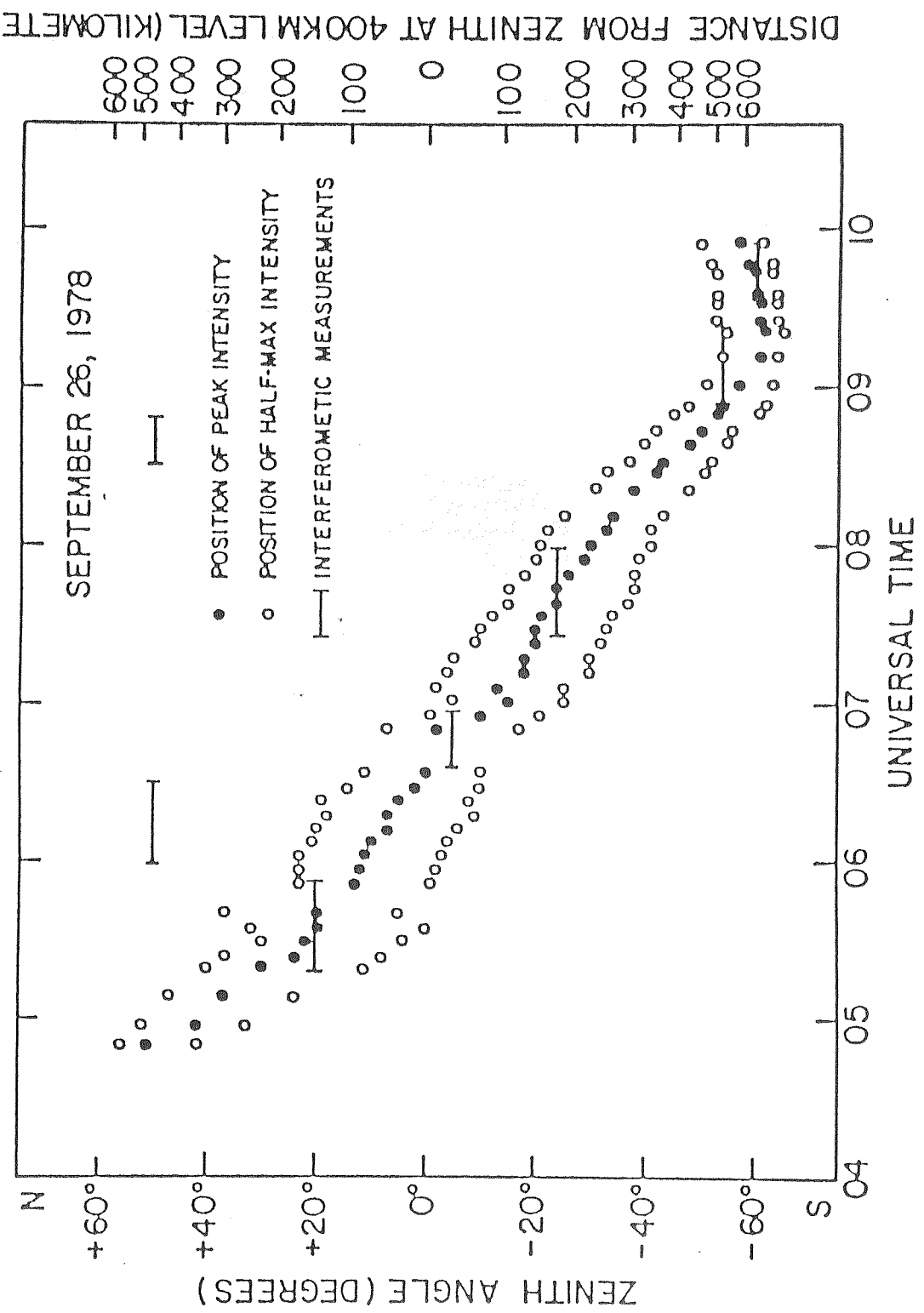

Figure 7-1 Zenith angles of the peak intensity, the half-maximum intensity and the interferometric measurement in the meridian plane as a function of universal time during the night of September 25/26, 1978.

where χ is the zenith angle of the peak intensity position of the arc (positive northward) in the geomagnetic meridian plane, λ_{mo} the geomagnetic latitude of the observing site, λ_m the geomagnetic latitude of the intercept of the line of sight at altitude h (assumed to be 400 km), and R_E the radius of earth in kilometers. In determining the 400 km L intercepts, potential errors may be caused by: (a) angular resolution of the photometer (±3°), (b) variation of the altitude of the peak intensity of the arc from the assumed 400 km (±50 km), and (c) the distortion of the actual field configuration from the field line given in equation (7-1). For the observed arc, the maximum values of errors in L value due to the combined causes (a) and (b) mentioned above was estimated to be $\Delta L \cong \pm 0.2$ at 0000 UT, decreasing to $\Delta L \cong 0$ at 0220 UT, and then again increasing to $\Delta L \cong 0.1$ at 0430 UT. We assumed that the field given by equation (7-11) provided a realistic representation of the field lines. Figure 7-2 displays the calculated L values of the peak intensity position of the SAR arc in the equatorial plane plotted as a function of local time. The L value varied from 3.6 at local midnight to 2.4 at 0420 local time. The average rate of change in L value was -0.28/hr.

The peak intensities, reduced to zenith values of the arc over the background 630.0 nm emission, were measured from the photometer records and plotted against universal time in Figure 7-3. Although the interferometer was primarily used for Doppler temperature measurements, its data could also provide the intensity of the arc. The cross checks between the intensities obtained from the photometer and the interferometer showed good

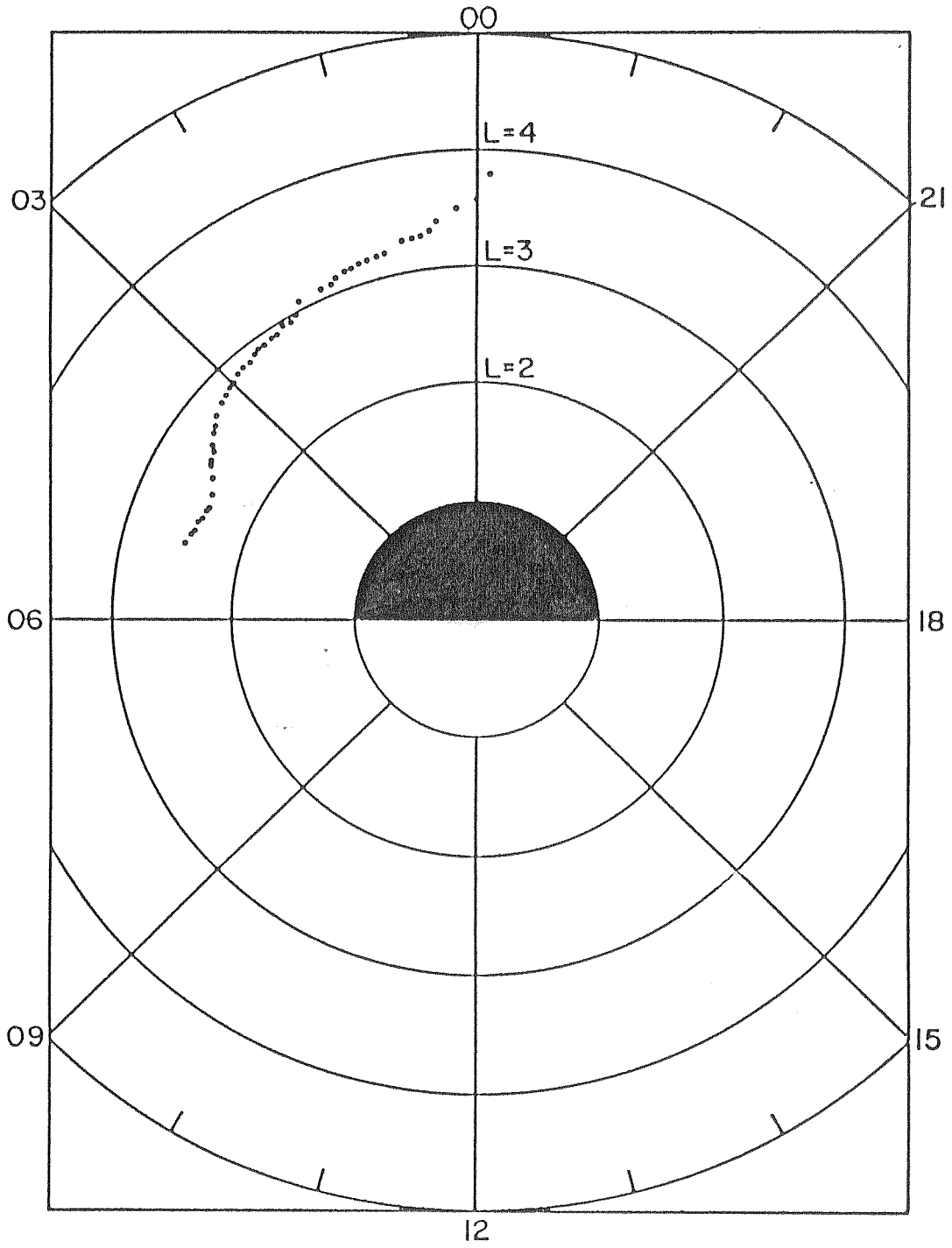

Figure 7-2 Calculated L values of the peak intensity position of the SAR arc in the geomagnetic equatorial plane as a function of local time.

agreement. As mentioned earlier, it can be seen from Figure 7-3 that the growth of intensity of the arc is very fast immediately after its appearance. The time constant of the increase in intensity is found to be 20 minutes before the intensity reaches its maximum value. After reaching its maximum value at around 0530 UT, the intensity decreased rather rapidly until 0700 UT. The rate of intensity change was still small enough to obtain reliable Doppler profiles, except during the growth period of the arc.

The temperatures measured on the night of September 25/26 are shown in Figure 7-4. The interferometer was looking at a zenith angle of either 70° north or 70° south in meridian plane before the appearance of the SAR arc. There is a decreasing trend during that period, and no significant change in temperature between the northern and southern skies was seen. After the appearance of the arc, the field of view of the interferometer was directed to either the position of peak intensity of the arc or outside the arc at a zenith angle of 50° north. The temperatures within the arc are plotted with full circles in Figure 7-4. They do not show any enhancement until 0700 UT but they do indicate an increase of about 200° K at around 0740 UT, that is, about 2.7 hours after the appearance of the arc. The temperatures within the arc again returned to normal values after 0900 UT.

Discussion

Since the SAR arc is generally believed to be located in L value near the position of plasmapause [Carpenter, 1971; Nagy et al., 1972], Figure 7-2 may provide the position of the plasmapause in equatorial plane during the

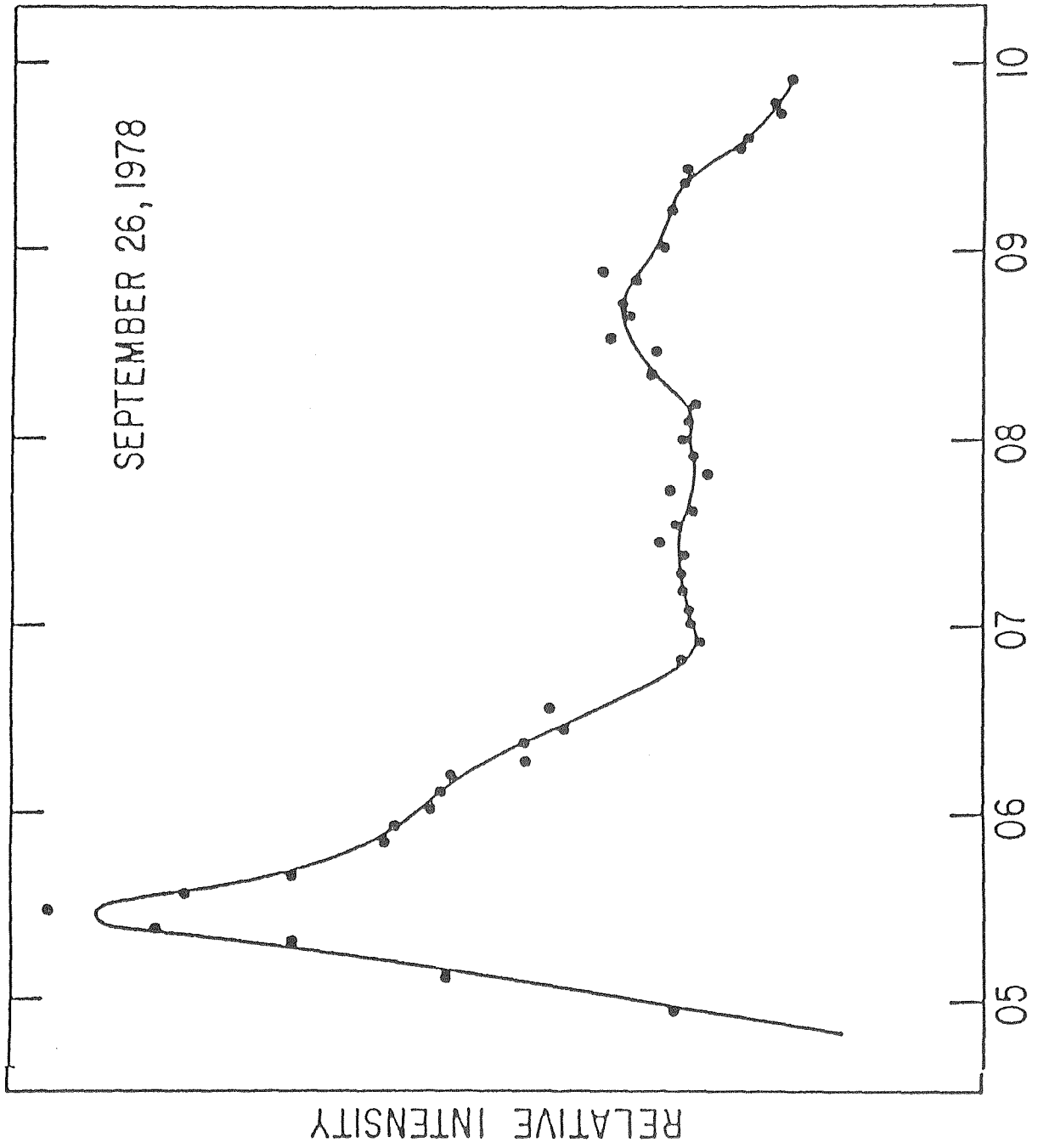

Figure 7-3 Peak intensities of the SAR arc reduced to zenith values over the background 630.0 nm emission as a function of time.

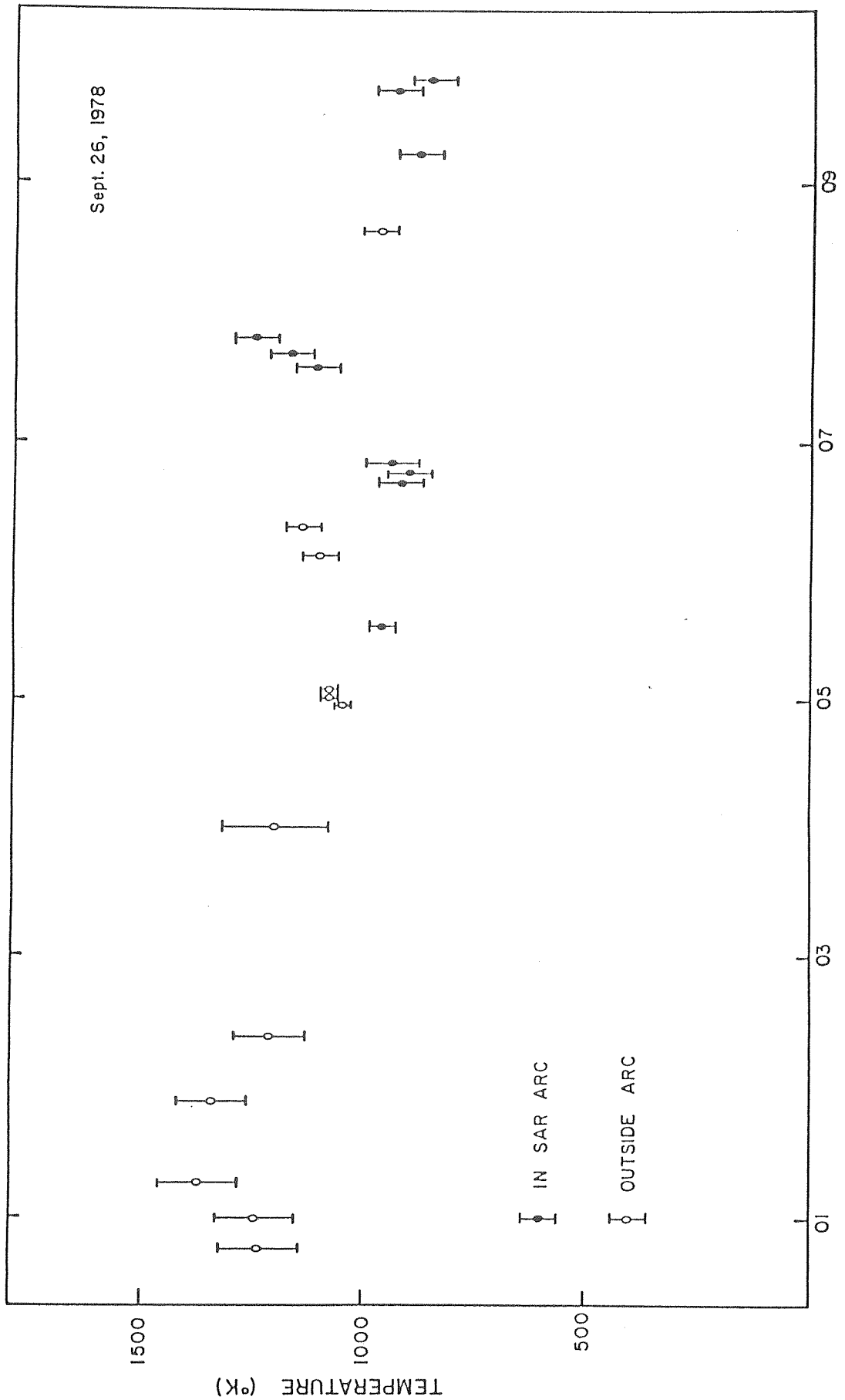

Figure 7-4 The neutral gas temperatures measured with a high resolution Fabry-Perot interferometer as a function of time. The open circles are for temperatures outside the SAR arc and the closed circles are for temperatures within the arc.

the event of the SAR arc on September 25/26 with a maximum uncertainty of $\Delta L \cong 0.2$. It is not clear whether the asymmetry seen in Figure 7-2 is due to the well established plasmapause asymmetry or due to the shrinking of the plasmapause during magnetically disturbed conditions.

The average velocity of equatorward drift of the arc, 240 km/hr or the average rate of change in L value, -0.28/hr is greater than the maximum value reported by Hoch and Smith [1971] for 13 events of the SAR arc during the solar cycle 20. Also, such a short time constant of 20 minutes for the growth period of the SAR arc has not been previously reported.

The temperature enhancement within the arc was found to be as great as 200° K. However, this temperature enhancement was variable in time and not consistently observed. Hays et al. [1969] observed no temperature enhancement within an arc of October 30 - November 1, 1968 within an experimental error of 75° K, while Hernandez [1972] reported a temperature increase of the order of 100° K for the arc of March 8-9, 1970. The latter observation also indicated the time variance of the temperature enhancement and seems to agree with our results. Although we cannot ascertain the altitude of the arc at this stage, Hernandez [1972] claimed that the heating within an arc can be variable with the altitude of an arc; that is , "the upper atmosphere near 400 km acts as a better heatsink than it does at about 500 km". This is one of the points which should be studied in detail during the SAR arc events in this solar cycle maximum.

CHAPTER VIII

SAR Arc and Concurrent Auroral Electrojet Activity

The SAR arc is usually observed with a concurrent visible aurora that occurs poleward of the arc, with a separation of several degrees in geomagnetic latitude [Craven et al., 1982]. Since both phenomena have their origin in the deep magnetosphere, it is apparent that a simultaneous study of the SAR arc and the concurrent auroral substorm should be useful in understanding the morphology and dynamics of the magnetosphere. However, very little work has been done on the study of the SAR arc and the concurrent auroral substorm [Ichikawa et al., 1969; Prasad et al., 1975].

In this chapter, results of the photometric observations of a SAR arc appeared on the night of September 25/26, 1978 (EST), which were already presented in the previous chapter, are studied in conjunction with the concurrent ground-based magnetometer observations of the auroral electrojet. A close relationship of the arc to the auroral electrojet was discovered through an analysis of the both optical and ground-based magnetometer data. The intensity and latitudinal positions of the concurrent auroral electrojets were obtained by the analysis of magnetograms from the IMS Fort Churchill maridian stations.

Intensities and positions (in zenith angle) of the arc were measured from the photometer record; and the latter were transformed into the positions in geomagnetic latitude, assuming the height of the arc to be 400 km.

In order to see auroral electrojet activity, if any was present at the same L-shell threading the arc, the positions of the arc were further

used to calculate the geomagnetic latitude of the intercept point of the magnetic field line threading the arc at an assumed auroral height of 110 km.

Magnetometer Data and Methods of Analysis

Magnetic data used in this study are the three-component magnetic records of 1-min averages from the IMS Fort Churchill meridian line of stations, listed in Table 4-1. The locations of magnetic observatories and Albany are shown in Figure 4-1. Baselines for these magnetic data were determined by choosing the quietest period closest to the onset of the substorm, using the published AE index [kamei and Maeda, 1981]. The selected time was 0030 UT on September 26, 1978.

The three component data were transformed into X_m (magnetic north), Y_m (magnetic east), and Z (downward) components using magnetic dipole coordinates; magnetograms for September 26, 1978 (UT) were then constructed (Figure 8-1). From Figure 8-1 we can see that a westward electrojet was centered between Gillam and Island Lake at 0520 UT. This is inferred from the positive ΔZ variations recorded at Gillam and at higher latitudes, and from the negative ΔZ variations recorded at Island Lake and at lower latitudes. In order to determine the position and intensity of the westward electrojet at 0520 UT on September 26, 1978, when the substorm activity had reached its maximum, ΔX_m and ΔZ values at 0520 UT from each station were plotted as in Figure 8-2 a. The best-fitted curves were drawn through ΔX_m and ΔZ data, respectively. The position of the center of the westward electrojet was located at the point where ΔZ values changed from positive to negative and the corresponding intensity of ΔX_m at that location was determined by

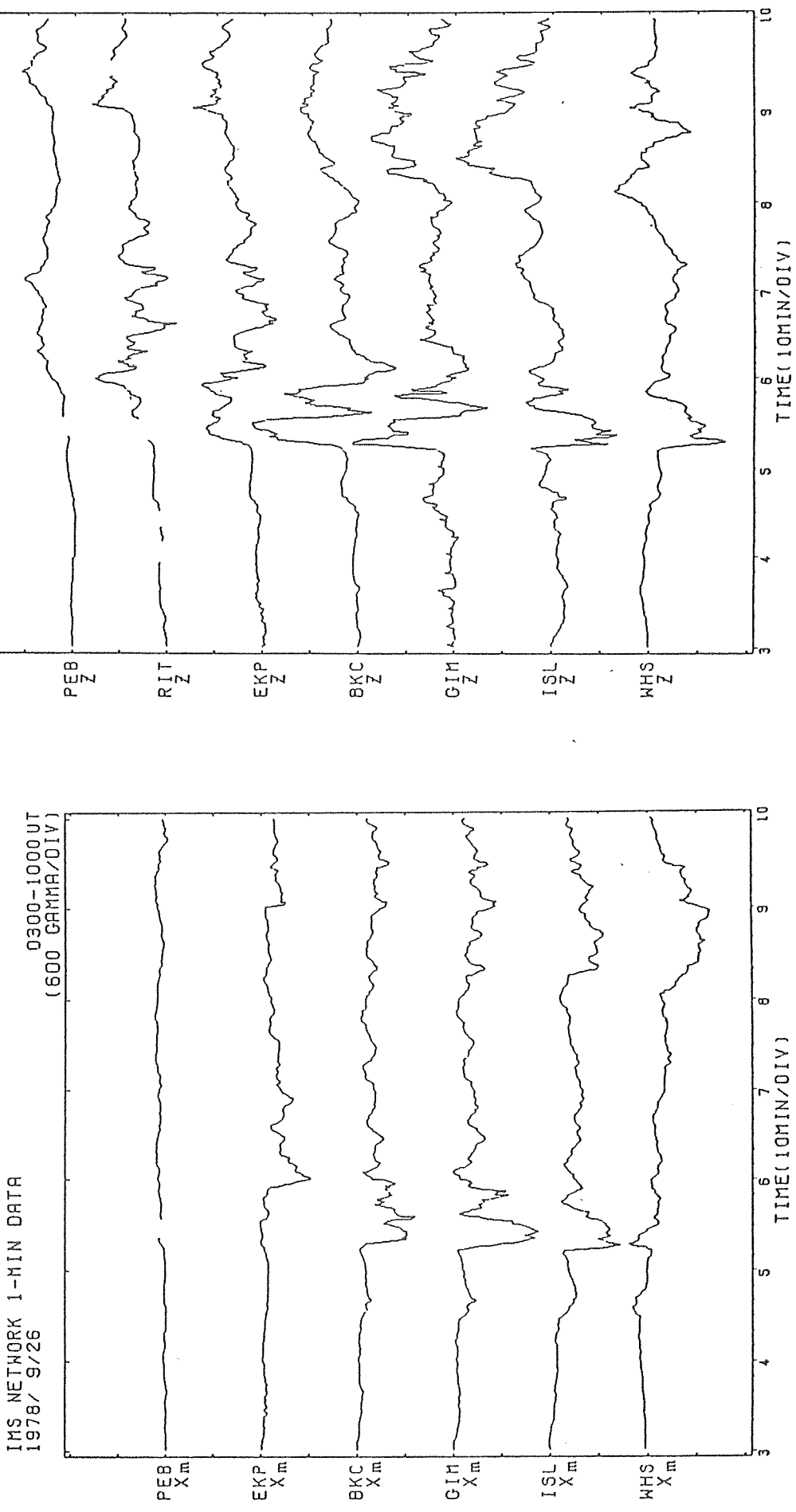

Figure 8-1 Plots of the one-minute averages of X_m (magnetic north) and Z (downward) components observed at stations in the Fort Churchill chain on September 26, 1978 (UT).

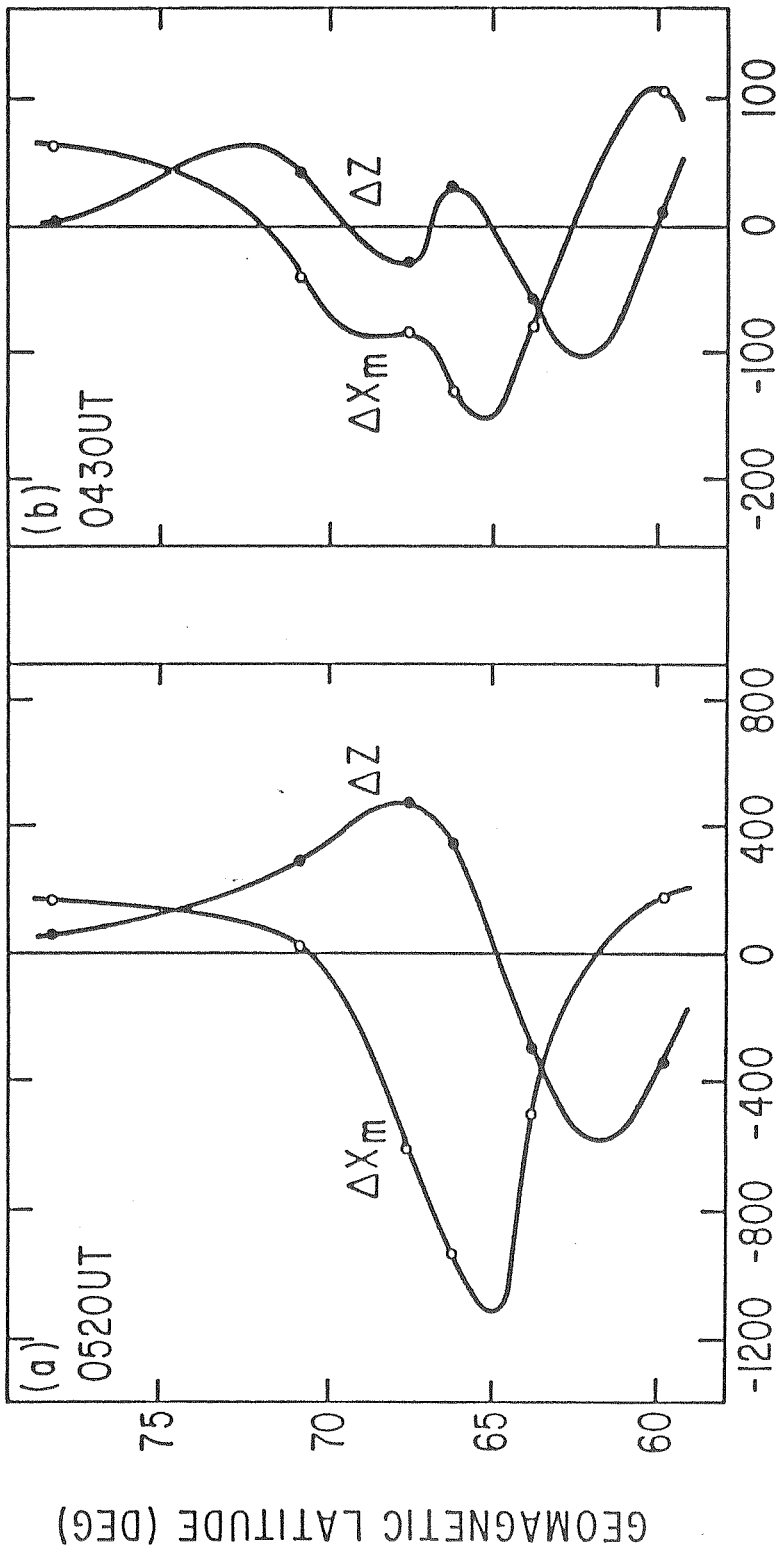

Figure 8-2 Latitudinal profiles of ΔX_m and ΔZ at two typical times: (a) 0520 UT, and (b) 0430 UT

measuring the maximum negative excursion of ΔX_m on the curve drawn through ΔX_m data. This was taken to be the measure of the electrojet intensity. In this manner, the positions and intensities of auroral electrojet at the Fort Churchill meridian were determined every 10 minutes, whenever it was possible. The method described above is well established for the determination of positions and intensities of the auroral electrojet [e.g., Kisabeth and Rostoker, 1971; Kamide et al., 1984]. This method has also been used for measurements of the thermospheric response to auroral activities described in Chapter 4.

Before 0440 UT, the presence of an eastward electrojet across the Harang discontinuity, equatorward of westward electrojet, is also indentified from the latitudinal profiles of magnetic records. An example at 0430 UT shown in Figure 8-2 b.

It should be noted that the magnetometer data are from the Fort Churchill meridian while the optical measurements are made along the Albany meridian. There is an approximate 30° difference in geomagnetic longitude between the two meridians, as seen in Figure 4-1. However, Craven et al. [1982] has confirmed, from observations made from the Dynamics Expolore-1 satellite, that SAR arcs extend continuously across the nightside of earth from terminator to terminator. Craven et al., [1982] further showed that the arc observed on October 21, 1981 was almost aligned along the same L-shell. Therefore, it is not unreasonable to compare our optical data with the magnetometer data, in spite of the longitudinal difference of 30° between the two meridians, assuming that the same variations of the arc were occurring at the Fort Churchill meridian.

Results

Figure 8-3 shows the combined results obtained from the analyses of optical and magnetic data that were described previously. From top to bottom, it shows the time variation of: (a) positions of the intercept points of the field line threading the arc at heights of 400 km (solid circles) and of 110 km (open circles); and locations of the concurrent auroral electrojets (both westward and eastward), all in geomagnetic latitude; (b) $|\Delta X_m^{max}|$, absolute values of the determined extremum in latitudinal profiles of ΔX_m; and (c) peak intensities reduced to the zenith values of the arc over the background 630.0 nm emission. Positions and intensities of the eastward electrojet and those of the westward electrojet are denoted by crosses and double circles, respectively (Figures 8-3 a and 8-3 b). In Figure 8-3 a, the height of the peak intensity of the arc was assumed to be 400 km.

The photometric observation commenced at 0000 UT on September 26, 1978, recording 630.0 nm emmission. The first appearance of the arc was noted on the photometer record at 0436 UT as a slight bulge on the background slope of the 630.0 nm emission due to intense poleward aurora.

The filter of the photometer was temporally switched to 557.7 nm from time to time in order to check whether the arc contained a conventional auroral feature. This was done at 0501 UT, 0512 UT, 0545 UT, 0639 UT, 0645 UT, 0817 UT, 0904 UT and 0915 UT. Each time no enhancement of the 557.7 nm emission was seen on the photometer record at the position of the arc. Thus, the confirmed spectral purity, together with the continuity

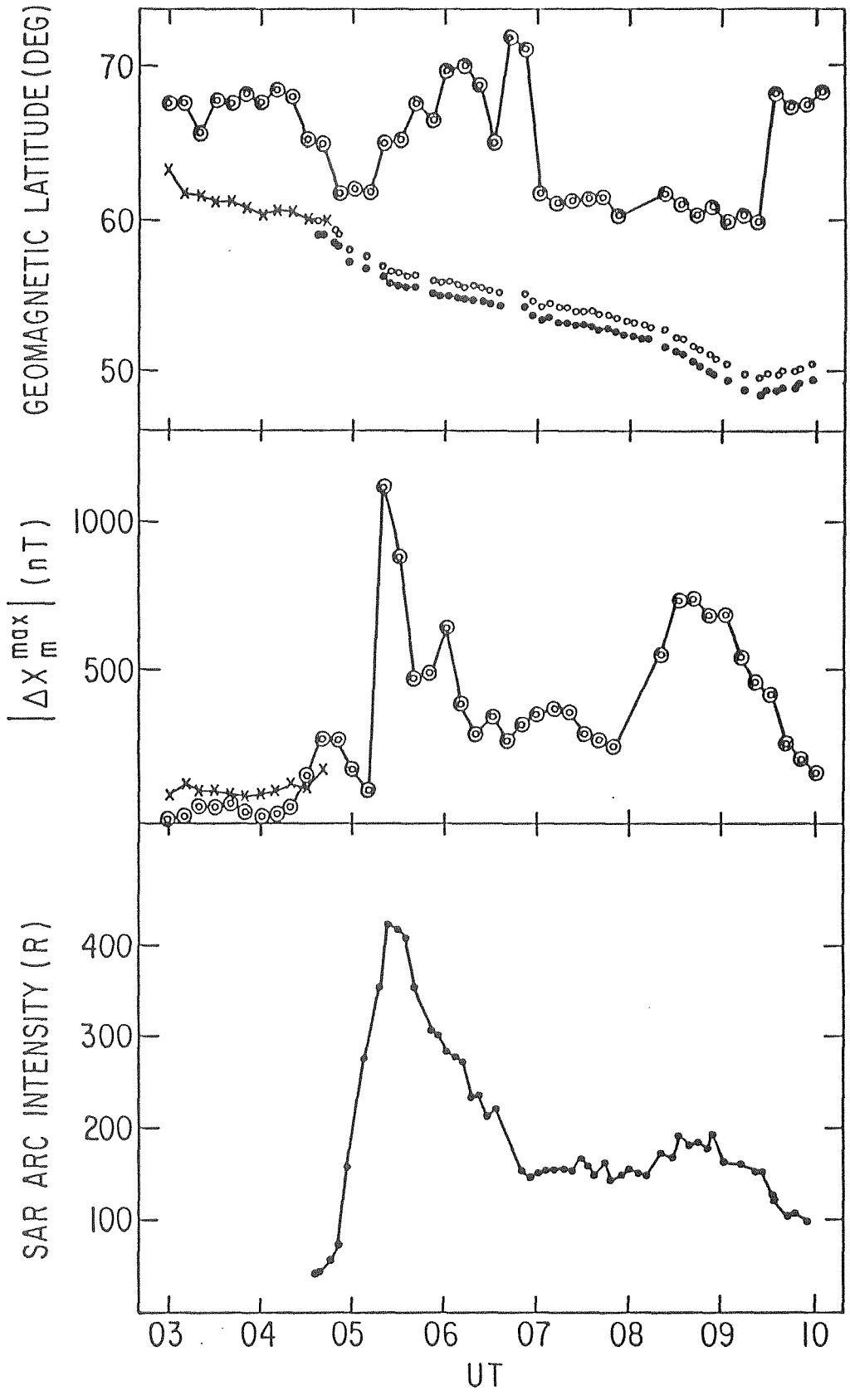

Figure 8-3 Time variations of, from top to bottom, (a) positions of the intercept points of the field line threading the arc at heights of 400 km (solid circles) and of 110 km (open circles), and locations of the centers of the concurrent westward (double circles) and eastward (crosses) auroral electrojets, all in geomagnetic latitude. The height of the peak intensity of the arc was assumed to be 400 km. (b) $|\Delta X_m{}^{max}|$, absolute values of determined extremum in latitudinal profiles of X_m, and (c) peak intensities reduced to the zenith values of the arc over the background 630.0 nm emission.

both in position and intensity of the arc, supports the fact that the arc observed on this night is indeed a SAR arc.

At the beginning, intensity of the arc was as low as (or even less than) 50R (Figure 8-3 c). It is noted that the geomagnetic latitudes of the intercept point at an auroral height of 110 km during the very beginning period of the arc and the peak in the eastward electrojet showed remarkable agreement. It is also seen that when the arc was first detected both eastward and westward electrojets were in their developing stages. After 0440 UT, the eastward electrojet faded out, at least within the latitudinal span of the magnetic stations used. After the eastward electrojet became undetectable, the intensity of the westward electrojet decreased until 0510 UT and then suddenly increased, reaching a maximum value of 1110 nT at 0520 UT. During the period 0440-0520 UT, intensity of the arc showed a rapid and monotonic increase. The maximum value of $|\Delta X_m^{max}|$ coincided with the highest intensity of the arc throughout the night (around 0520 UT). After the value of $|\Delta X_m^{max}|$ and the intensity of the arc reached their maximum values almost simultaneously, the time variations of the intensity of the arc appeared to be closely related to the intensity changes of the westward electrojet. We can see that a shoulder in the intensity of the arc around 0610 UT, a minimum around 0655 UT, a small maximum around 0730 UT and a second largest maximum around 0830-0850 UT coincided closely to those appearing on the curve of $|\Delta X_m^{max}|$ variation (i.e., a peak at 0600 UT, a minimum at 0640 UT, a broad but small maximum around 0710 UT and second largest maximum at 0830 UT; each with a time lag of 10-20 minutes,

respectively).

As for the geomagnetic positions of the arc, the field line threading the arc coincided with the positions of the eastward electrojet (at height of 110 km) at the onset of the arc, as described earlier. Thereafter, the arc moved generally southward throughout the remainder of the night. However, looking further into details of Figure 8-3 a, it is noted that when the westward electrojet moved equatorward (quite rapidly) at 0650-0700 UT, equatorward movement of the arc was also accelerated and followed by a slight poleward movement. It is also seen that when the westward electrojet showed a rapid poleward movement at 0920-0930 UT, the movement of the arc changed its direction to poleward.

Discussion

The positions of the intercept point, at an assumed auroral height of 110 km of the magnetic field line, threading the arc during the onset period at around 0440 UT coincided closely with the positions of the eastward electrojet center. Investigations on the geometrical configuration of a three-dimensional current system for the magnetospheric substorm [e.g., Kamide et al., 1976; Heikkila, 1978] have shown that the eastward electrojet is connected to the partial ring current through field-aligned currents. On the other hand, it has been well established that the SAR arc is located in L-values at the position of plasmapause [Rees and Roble, 1975]. Therefore, it appears that the eastward electrojet, the partial ring current and the plasmapause are all located in the same L-shell (L~4.0) at the beginning of the arc; this supports the well-known theory that the

SAR arc originates from an interaction between the ring current and the plasmapause [Rees and Roble, 1975]. At 0450 UT, the separation between the position of westward electrojet center and the position of the intercept point of the field line threading the arc at a height of 110 km was as small as 2.7° in geomagnetic latitude, amounting to $\Delta L \approx 0.68$. This implies that the plasmapause location in equatorial plane was very close at this time to the plasma sheet which is connected to westward electrojet through field-aligned currents [e.g., Heikkila, 1978]. Observations made from ISEE-1 and DMSP satellites [Horwitz et al., 1982] show that the plasmapause location often coincides to within $\Delta L \sim 0.1$-0.2, with both the plasma sheet inner boundary and the field line threading the equatorward boundry of the auroral oval.

Our data indicate that the rise and fall in the intensity of the arc, after the arc reached its maximum intensity at 0520 UT, closely resembled the variation of the intensity of the westward electrojet ($|\Delta X_m^{max}|$), with a time lag of 10-20 minutes. Since the primary cause for intensification of both the westward electrojet and the energy density of the ring current is the plasma injection into the plasma sheet and the ring current, respectively, it is conceivable that the substorm-associated plasma injection causes development of the westward electrojet as well as an increase of the SAR arc intensity that is believed to be related to the energy density of the ring current. The observed relationship between the intensity of the westward electrojet and that of the arc, therefore, also supports the theory that the energy source of the SAR arc is the ring current.

Recently, Moore et al. [1981] reported that they observed the 'substorm injection front' propagating earthward at velocities in the range of 10-100 km/s. Although it is not possible to deduce the propagation velocity of this injection front from our data without knowing changes of magnetic field configuration in the deep magnetosphere and the time required for transfer of the energy from equatorial ring current to the SAR arc, the observed time lag supports the concept that the injection front is propagating earthward. Before ~0520 UT the intensity of the westward electrojet experienced the first small intensification during the period 0420-0440 UT, and it was toward the end of this period when the arc appeared. The westward electrojet then subsided until 0510 UT, followed by quite a large intensification. On the other hand, the arc intensity showed a monotonic increase from its appearance until ~0520 UT. Obviously, the arc intensity variation did not correspond with that of the intensity of the westward electrojet during this period. These opposite variations during the period 0440-0510 UT may be explained by the following interpretation: the plasma injection occurred preceding the first small intensification of the westward electrojet, causing the colocation of the plasmapause and the ring current. This also caused an increase of the energy density of the ring current, thereby triggering the arc. While the energy injected into the plasma sheet is immediately exhausted by polar auroral processes that occur on the closed loop of the current system, the time constant of the decay of the ring current is considerably larger.

Therefore, the arc intensity may, at least, remain almost constant during the rapid decay of the westward electrojet if other factors which determine the arc intensity are kept unchanged. This also explains a lesser degree of variation in the arc intensity compared to that of the intensity of westward electrojet after ~0520 UT. Whether the reason for the increasing intensity of the arc during the period 0440-0510 UT was due to continuing development of the ring current and/or because of the time required for the arc to grow in the ionoshpere is not clear.

Finally, it should be noted that the periods when the intensity of westward electrojet and the intensity of the arc reached their maxima (0500-0600 UT and 0800-0900 UT) coincided with the periods of decreasing D_{st} values, indicating energetic plasma injection into the ring current. The hourly values of D_{st} at 04, 05, 06, 07, 08, 09 and 10 UT, respectively on September 26, 1978 were -40, -52, -59, -54, -52, -60, and -65 nT.

In summary, the optical observations of the SAR arc were compared with the concurrent ground-based magnetometer observations of the auroral electrojet activities. Results of the combined observations include:

1. At the beginning of the arc's appearance near local midnight, the positions of the intercept point, at an assumed auroral height of 110 km, of magnetic field line threading the arc coincided with the eastward electrojet center.
2. After around 0520 UT, during the period of general decay of the arc, the intensity variation of the arc followed closely that of the westward electrjet, with a time lag of 10-20 minutes.

3. The arc showed equatorward movement in general, however, during the periods when the westward electrojet moved rapidly for a great distance, the arc also moved in the same direction but with much less degree.

CHAPTER IX

Observations of a SAR Arc Associated with an Isolated Substorm

A weak but well defined SAR arc appeared on the night of September 26/27, 1979 (EST). The arc was photometrically observed from two ground stations; one at Albany, New York, and the other at Plattsburgh, New York (geographic latitude 44.69° N, longitude 286.47° E; geomagnetic latitude 56.3°). Triangulation from the two stations enabled us to measure movements of the arc as well as its height. Magnetograms obtained from stations in Canada showed that an isolated substorm occurred simultaneously poleward of the arc. This remarkable coincidence between the onset of the arc and of the isolated substorm suggests that an appearance of the arc may have a strong connection to the development of substorm-related currents although electrojet currents are not expected to flow within the ionosphere at the position of the arc.

Photometric Observations of the SAR Arc

The instrument used for photometric observations of the arc from Plattsburgh is a multicolor meridian-scanning photometer which is identical to the one located at Albany. The photometers swept the sky every 5.5 minutes between zenith angles of 75° N and 75° S in a vertical plane that contained Plattsburgh and Albany. The photometer at Albany has four narrow band interference filters centered at 630.0 nm, 557.7 nm, 610 nm, and 530 nm. The filters used in the photometer at Plattsburgh are centered at 630.0 nm 557.7 nm, 427.8 nm, and 415.0 nm. The field of view of the both photometers

is 4.7°.

The general condition of geomagnetic disturbances for the two-day period, September 26/27, 1979 (UT) are shown in Figure 9-1 in three different geomagnetic indices; an auroral electrojet index, AE; an hourly value of D_{st}; and a three-hourly value of planetary index, K_p. The photometric observations commenced at both stations around 0020 UT on September 27, 1979 and the scanning to the sky was made with 630.0 nm filters until detection of the arc was made first from Albany at 0307 UT; the intensity was barely detectable. Detection from Plattsburgh soon followed at 0317 UT. AE values during the period 0000-0300 UT on September 27, 1979 (Figure 9-1) showed moderate disturbances. However, the main contributing stations were Abisko and Leirvogur which are located far east of the North American continent [Kamei and Maeda, 1982]. As we will see later, the magnetograms obtained from Canadian stations showed substorm activities over Canada that were confined within the period 0300-0400 UT on September 27, 1979. As seen in Figure 9-1, when the arc was first detected, the hourly value of D_{st} was increasing from its minimum value (-34 nT) of the two-day period, and the value of K_p was maximum (5_) of the period. Visible aurora was seen at low elevation in the northern sky from Plattsburgh around the 0300-0330 UT period.

An example of chart records of the photometers is shown in Figure 9-2. As seen in the figure, the arc appeared as a bump over the background 630.0 nm emission. Throughout the entire period of the arc duration, the arc was seen to the north of zenith from Albany and to the

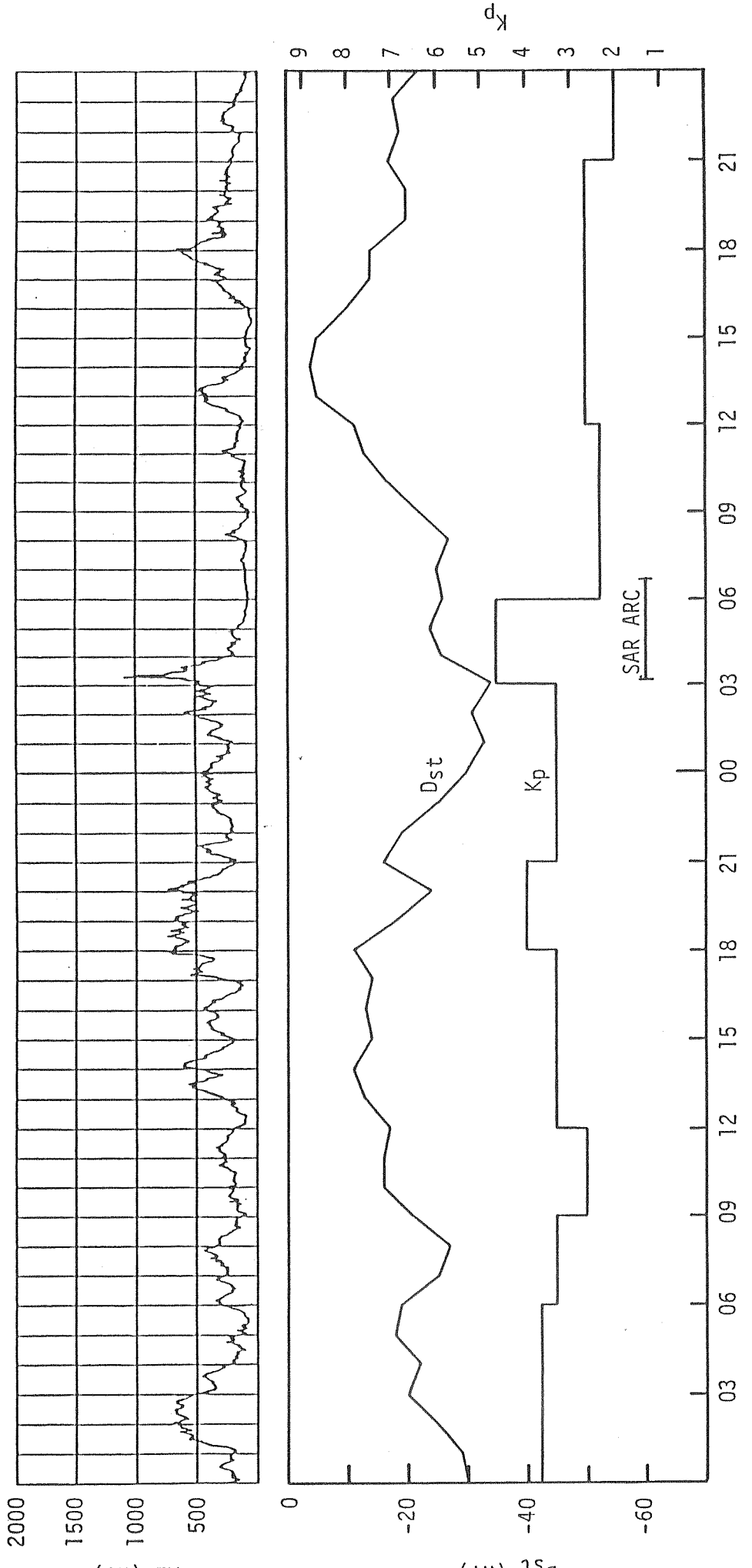

Figure 9-1 Variations of three geomagnetic indices; AE index, hourly value of Dst, and K_p during the two-day period, September 26-27, 1979 (UT). Observed SAR arc duration is indicated by a horizontal bar.

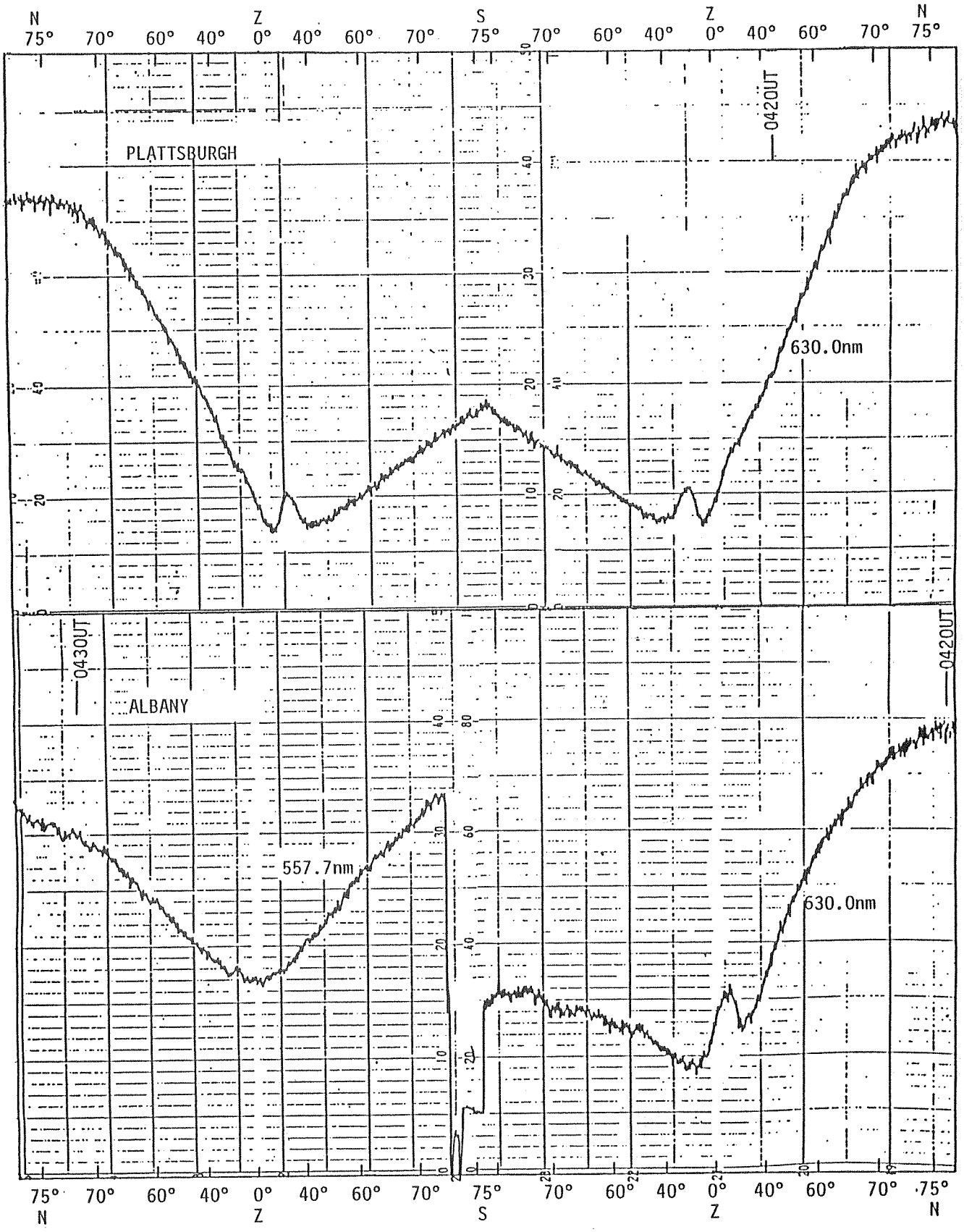

Figure 9-2 An example of raw data on chart record of the photometer.

south of zenith from Plattsburgh. The filter of the photometer was temporarily switched to 557.7 nm at Albany, and to 427.8 nm and 557.7 nm at Plattsburgh from time to time in order to check whether the arc contained conventional auroral features. Each time no enhancements of the 427.8 nm or 557.7 nm was seen on the photometer record at the position of the arc. Intensities and positions (in zenith angle) of the arc were measured from the chart records obtained at both stations. Figure 9-3 shows the time variations of the arc intensity observed from Albany and Plattsburgh, separately. The detection threshold for the arc and errors in emission rate for both stations are included in the figure. The arc intensity detected from Albany show a steep increase immediately after its appearance at 0307 UT and it reached its maximum around 0410 UT. Then the arc intensity decayed slowly and became undetectable after 0643 UT. The numbered tick marks in the upper part of Figure 9-3 are 10-minute time marks starting at 0320 UT. The maximum intensity positions (in zenith angle) of the arc were measured at both stations and smooth curves were drawn through data points in order to make triangulation of emission peak (integrated along the line of sight) position of the arc. At the times shown by the tick marks in Figure 9-3, emission peak positions of the arc in a vertical plane containing Albany and Plattsburgh were calculated using spherical trigonometry. The results are shown in Figure 9-4. The number of each data point in the figure corresponds to that of tick marks in Figure 9-3. For points 1, 4, 10, and 17, the areas of uncertainty arising from an error in zenith angle measurements ($\pm 1^\circ$) are shown by rhombuses. Projection of two magnetic field

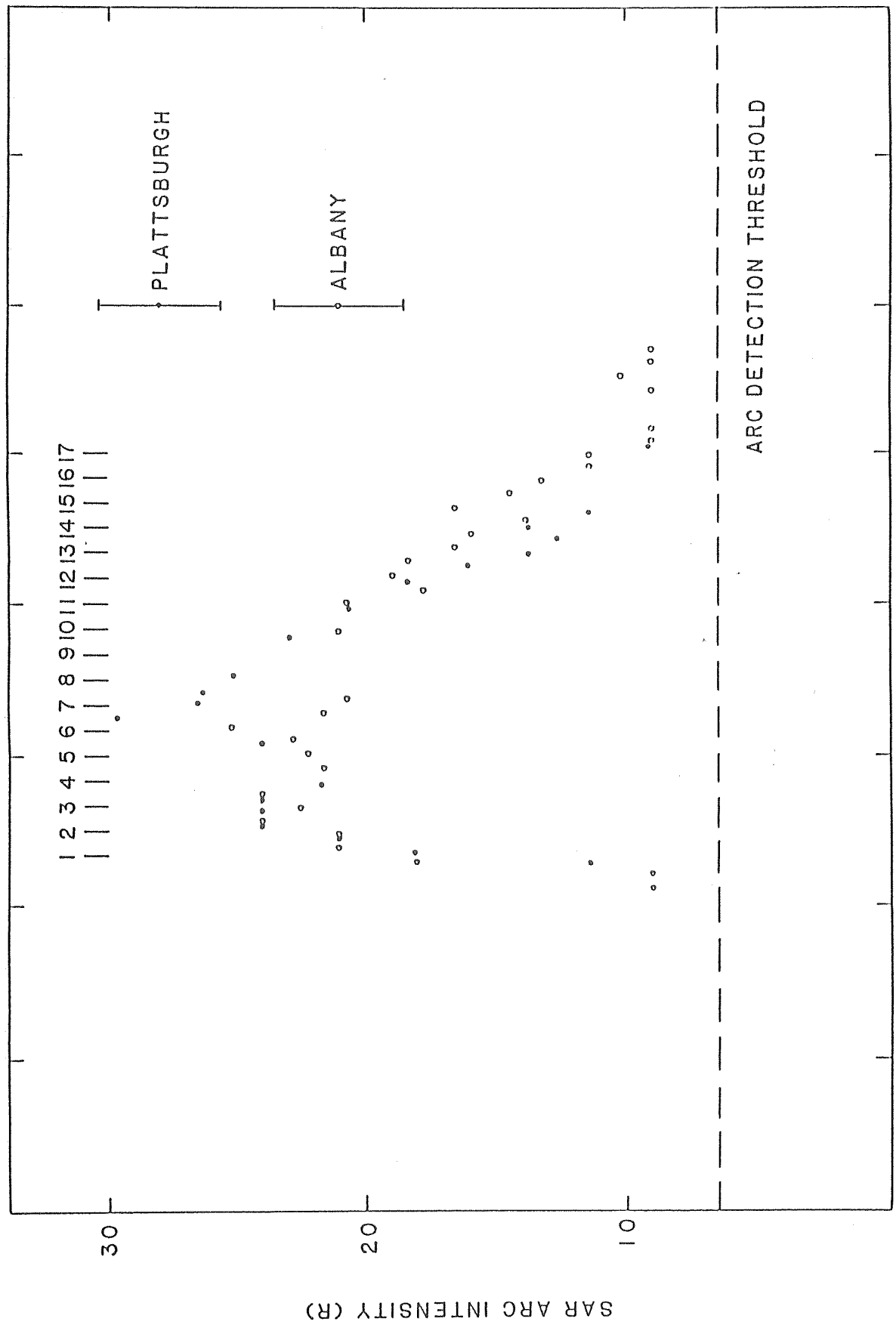

Figure 9-3 Variations of the SAR arc intensity from the two stations. Typical observational uncertainties for each station are indicated by error bars.

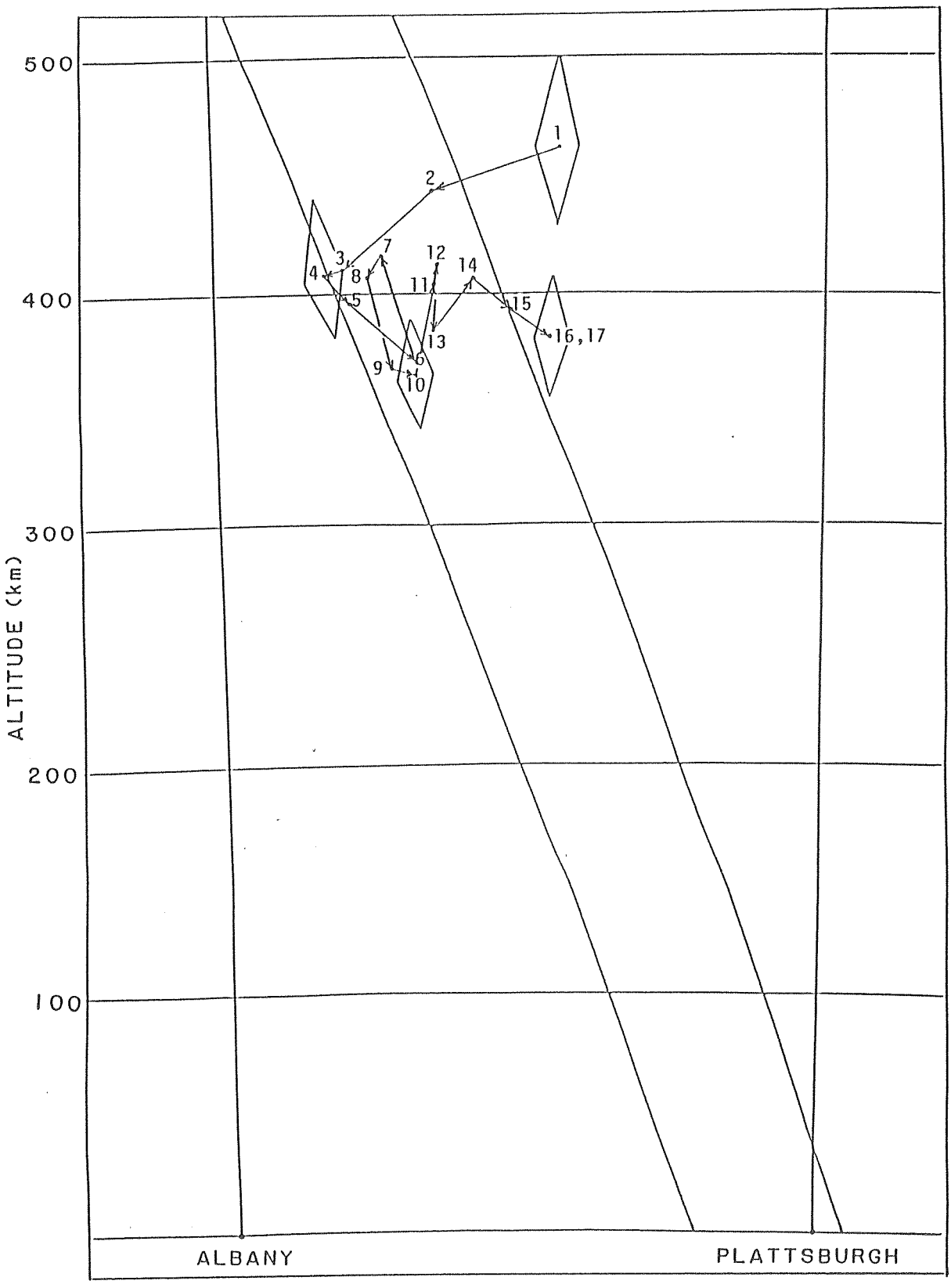

Figure 9-4 Movements of emission peak positions of the SAR arc in a vertical plane containing the two stations from which triangulation was made. The number of each point corresponds to that of the time marks in Figure 9-3. For points 1, 4, 10, 17 the areas of uncertainty arising from an error in zenith angle measurements (±1°) are shown by rhombus. Projection of field lines are also included.

lines which envelope the arc position on the plane are included in Figure 9-4. It is seen from both Figures 9-3 and 9-4 that the arc moved rapidly equatorward and downward during the period of steep increase of intensity. Thereafter, the arc reversed its direction and moved poleward while moving up and down around an altitude of 400 km along field lines. As seen in Figure 9-3 there is a considerable difference in arc intensity between the two stations around 0420 UT, the value for Plattsburgh being greater. This can be understood easily if the arc has a structure elongated along a field line. Since the direction of the arc seen from Plattsburgh is almost parallel to that of the field line, the integrated intensity of the arc would be greater for Plattsburgh if the arc had such field aligned structure. As seen in Figure 9-3, the arc on this night was considerably weak, with a maximum intensity of less than 30 R. However, the confirmed spectral purity, together with the characteristic height of this arc, supports that the arc observed on this night was indeed a SAR arc.

Magnetograms and Satellite Particle Data

Magnetograms obtained at 9 stations in Canada were used to study magnetic disturbances associated with the SAR arc. The locations of magnetic stations and the two stations used for the photometric observations are plotted in Figure 9-5 in geomagnetic coordinates and also given in Table 9-1. In Figure 9-5, a trajectory of DMSP-F2 satellite at the time of an isolated substorm is also shown. Figures 9-6 a and 9-6 b show variations of the horizontal component and the vertical component of

TABLE 9-1

Names, Code Names, and Locations of the Stations

Station	Code Name	Geographic Lat. (°N)	Geographic Long. (°E)	Geomagnetic Lat. (°N)	Geomagnetic Long. (°E)
East-West chain					
Norman Wells	NOW	65.03	233.00	69.35	276.94
Fort Simpson	FSP	61.75	238.77	67.20	287.16
Fort Smith	FSM	60.00	248.00	67.26	299.59
Lynn Lake	LYN	56.85	258.74	65.76	315.78
Fort Churchill chain					
Rankin Inlet	RIT	62.80	267.67	72.84	323.51
Back	BKC	57.69	265.77	67.65	324.39
Gillam	GIM	56.35	265.58	66.32	324.87
Albany meridian					
Great Whale River	GWC	55.30	282.25	66.80	347.30
Ottawa	OTT	45.40	284.45	57.00	351.54
Photometric Observation Stations					
Plattsburgh	PTB	44.69	286.47	56.34	354.19
Albany	ALB	42.68	286.18	54.33	353.92

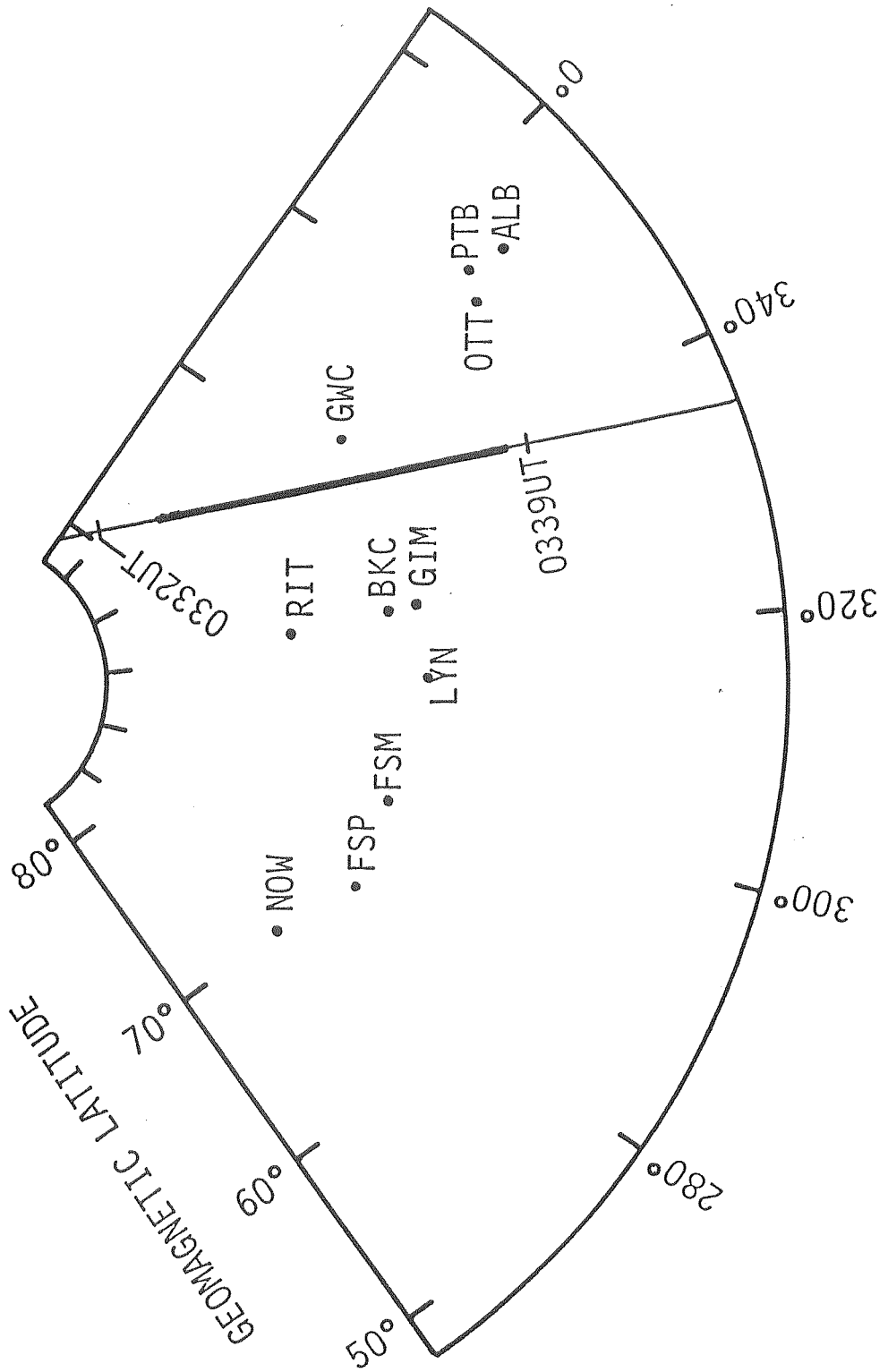

Figure 9-5 Locations of magnetic stations and the two optical stations in geomagnetic coordinates. Also see Table 9-1 for names and coordinates of the stations. A trajectory of DMSP-F2 satellite at ~0335 UT on September 27, 1979 is shown. Thick part of the trajectory indicates the extent of auroral particle precipitation.

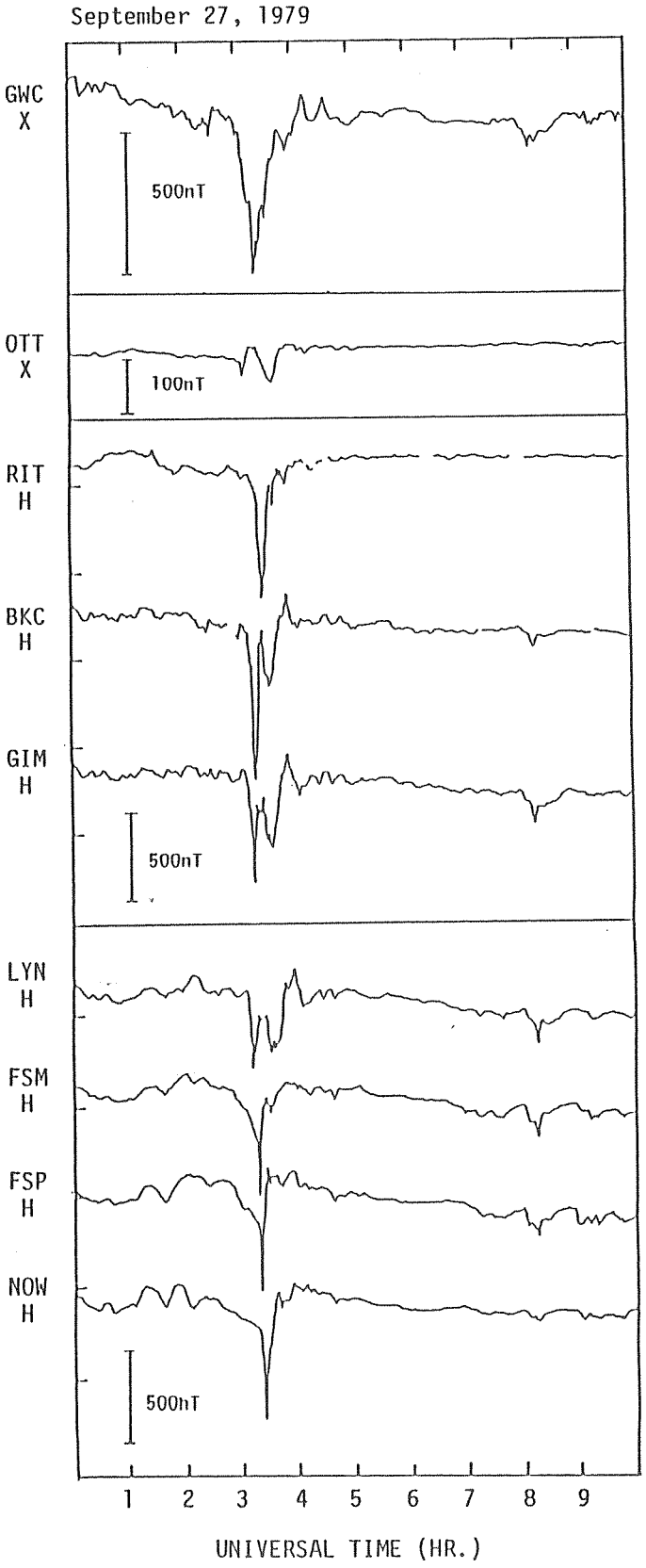

Figure 9-6a Stuck-up magnetogram of horizontal component observed at stations listed in Table 9-1 on September 27, 1979. Note that the data for GWC and OTT are geographical north component while the rest are local geomagnetic north component. Also note that scales are different for GWC and OTT.

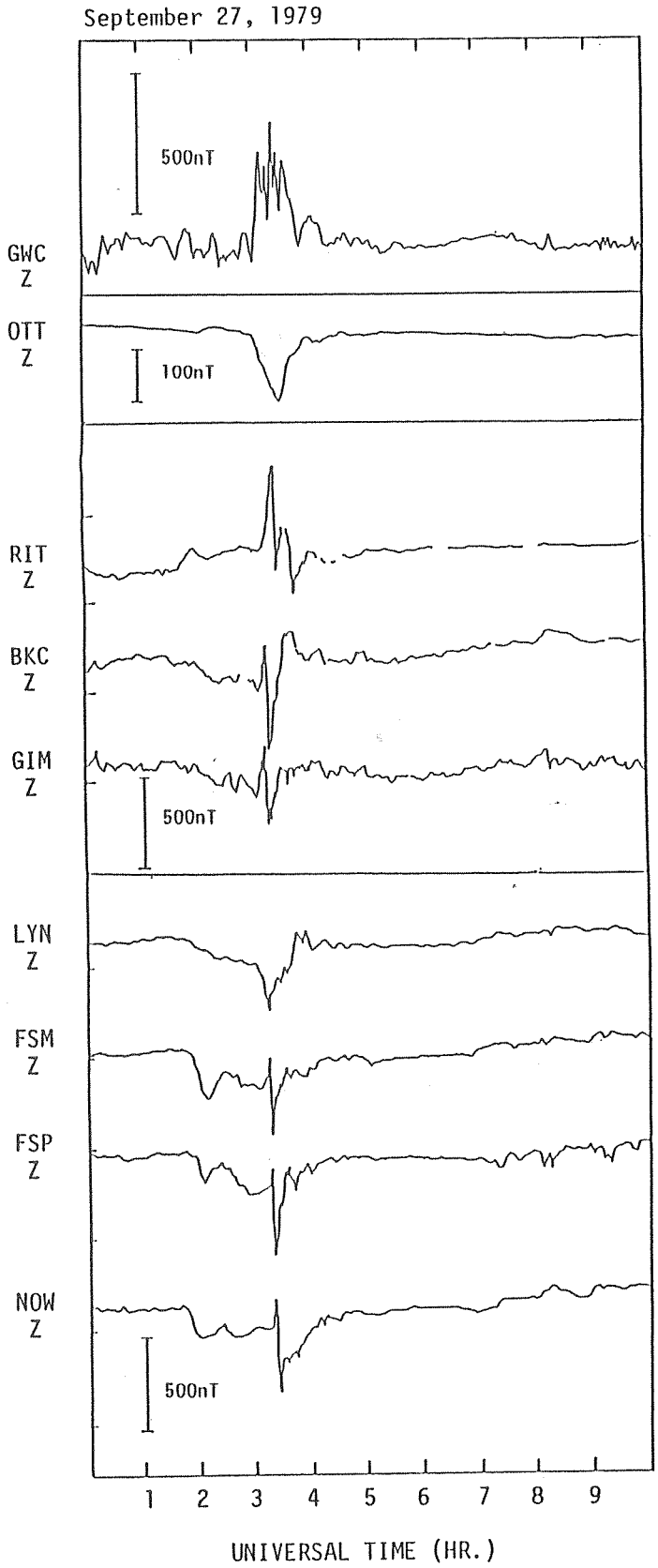

Figure 9-6b Stuck-up magnetogram of vertical component observed at stations listed in Table 9-1 on September 27, 1979. Note that scales are different for GWC and OTT.

magnetic field, respectively. Note that traces in Figure 9-6 a, for GWC and OTT are the geographic north component, X and those for the rest of the stations are the local geomagnetic north component, H. Unfortunately, it is impossible to determine the intensities and positions of the westward electrojet at either the Albany or Fort Churchill meridian [e.g., Kisabeth and Rostoker, 1971; Okano et al., 1985], because there were too few stations operating at either of the meridians. However, from Figure 9-6 a, we can see that an isolated substorm commenced around 0310 UT. We can infer from Figure 9-5 and Figure 9-6 a, that the substorm activity propagated poleward and westward. The first detection of the SAR arc was made at 0307 UT, indicating the appearance of the arc coincided with the onset of the substorm. As stated before, an arc located close to the zenith can only be detected by the meridian-scanning photometer every 5.5 minutes. Therefore, more exact determination of the onset time of the substorm using a method such as the Pi2 pulsation is meaningless in our case. From Figure 9-6 b, we can also infer that the westward electrojet center associated with this substorm is located between GWC and OTT at the Albany meridian, between RIT and BKC at the Fort Churchill meridian, and north of the East-West chain.

Figure 9-7 shows electron precipitation data measured by DMSP-F2 satellite. The three traces in the figure show, from top to bottom, the integrated electron flux (el/cm^2 sr s), the energy flux (ergs/cm^2 sr s), and the average energy (eV) between 50eV and 20keV. This data indicate that the auroral electron precipitation is bounded by 76.8° and 59.6° in

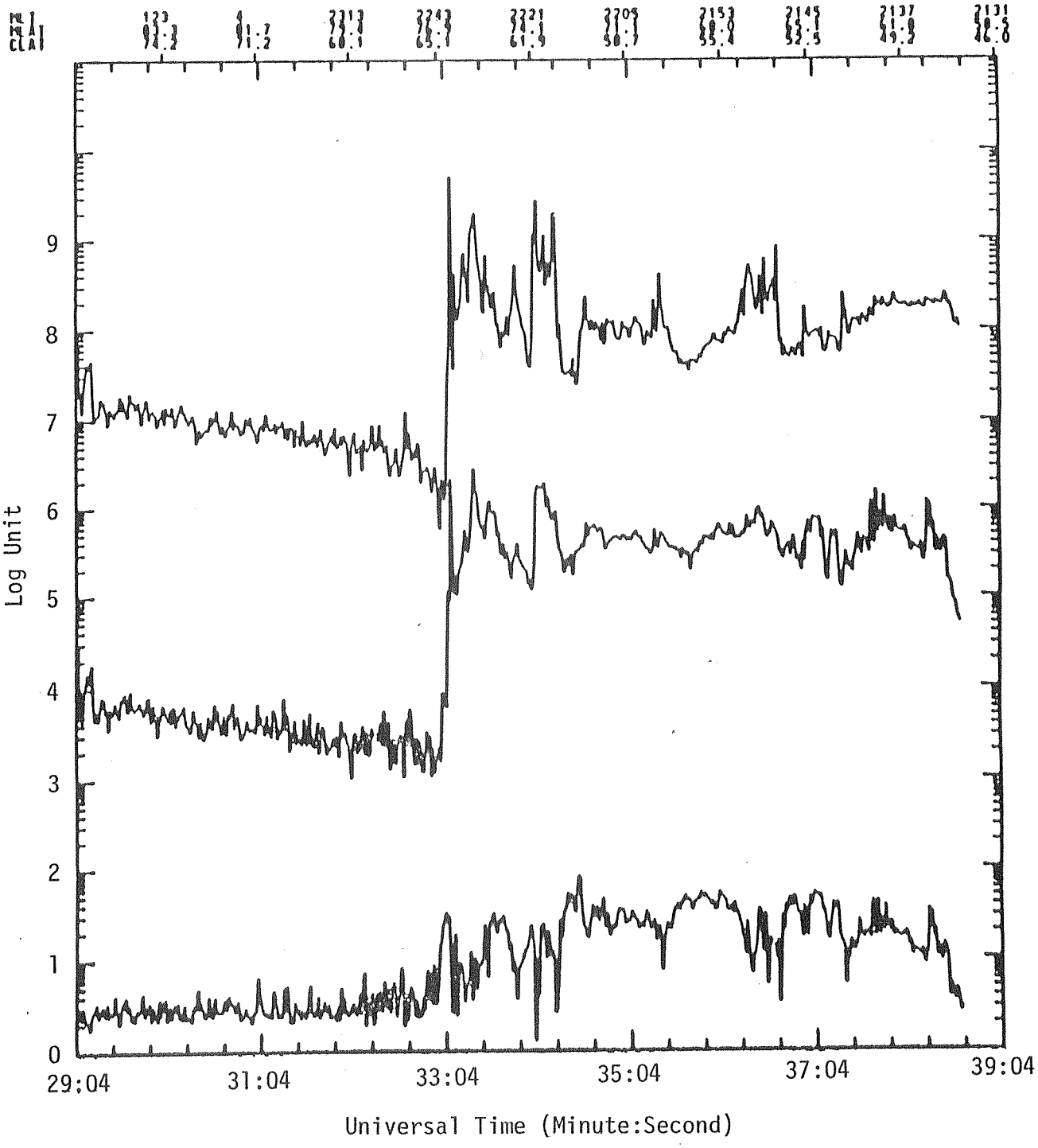

Figure 9-7 Observation of electron precipitation made from DMSP-F2 satellite. Three traces are, from top to bottom, the integrated electron flux (el/cm^2 sr s), energy flux (ergs/cm^2 sr s), and the average energy (eV) between 50 eV and 20 keV. The 1 erg/cm^2 sr s and 100 eV level are at log scale 6 and 0, respectively. The satellite trajectory in the magnetic local time (MLT), the geomagnetic latitude (MLAT), and the geographic latitude at 100 km altitude of the field line threading through the satellite (CLAT) is given above the panel.

geomagnetic latitude. The extent is shown by thick part of the satellite trajectory in Figure 9-5. The latitudinal extent of electron precipitation seems consistent with the location of the westward electrojet center inferred from the vertical component of magnetograms.

Discussion

The arc observed on the night of September 26/27, 1979 (EST) is believed to be a typical SAR arc, although its intensity is low, due to the observed spectral purity and its height (∿400 km). The poleward auroral activities were well separated from the arc, considering the location of the westward electrojet center which was inferred from the magnetograms and the satellite particle data.

Accepting the observed arc to be a real SAR arc, the coincidence of the onset of the substorm and the appearance of the arc within observational uncertainty is remarkable. Although it has been well established that the SAR arc is a phenomena closely related to geomagnetic storms, the relationship between SAR arcs and substorms have not been given much attention thus far. In the previous chapter, it was noted that the appearance of a SAR arc on the night of September 25/26, 1978 (EST) was during a period when the poleward electrojet intensity was increasing, and also when the intensity variation of the arc followed closely that of the westward electrojet, with a time lag of 10-20 minutes after the arc reached its peak intensity. In the case described in this chapter, the intensity variation of the arc does not have one-to-one correspondence with substorm activities; after the simultaneous onsets, substorm activities subsided within one hour while the

arc remained detectable until 3.5 hours after its appearance. Nevertheless, the coincidental occurrence of both phenomena strongly suggests that the coincidence was not a mere accident but that there must be some physical link between the SAR arc and the substorm, although its mechanism is not clear at present.

CHAPTER X

Observations of Soft Electron Flux during SAR Arc Event

Since the proposition of the soft electron flux hypothesis by Dalgarno [1964], there have been very few attempts directed towards investigation of this mechanism. Chandra et al. [1971] examined the integrated flux of suprathermal electrons (E>5eV) in an attempt to correlate them with an SAR arc event during the night of September 28/29, 1967. The arc was observed from the observatories at Richland, Washington and Fritz Peak at Boulder, Colorado, between L = 2.4 and 3.0 during the period 0506-1125 UT. The appearance of the arc was also noted by Ichikawa and Kim [1969] at Moscow, Idaho between the L shells 3.4 and 2.6 during the period 0300 UT to 0900 UT.

Chandra et al. [1971] used measurements from the ion trap experiment on the OGO 4 satellite that was orbiting at about 900 km and from the planar trap experiment on the EXPOLORER 31 satellite orbiting at about 2000 km to investigate this arc. From these two sets of photoelectron flux measurements, it is clear that the soft electron flux did not exceed 8×10^{7} cm^{-2} sec^{-1} at the location of the arc, during the entire period of observation of the arc. Thus the attempts made by Chandra et al. [1971] to test the validity of the soft electron hypothesis in the excitation of the arc on the night of September 28/29, 1967 were not successful.

Later, Nagy et al. [1972] correlated a low intensity arc of August 8/9, 1970 with some soft electron measurements obtained from OGO 6 satellite. The arc with an intensity of about 50 R was located at L = 3.1 during the period 0719 UT to 1019 UT. At about the height of the peak 630.0 nm emission, the

photoelectron flux found at the same L value amounted to about 6 x 10^{6} cm^{-2} sec^{-1}. Even as poleward as L = 4.0, the flux was found to be significantly less than 6 x 10^{7} cm^{-2} sec^{-1} during four different profiles obtained from four different orbits of OGO 6 from the retarding potential analyzer. In a subsequent report, Nagy et al. [1974] attempted to correlate soft electron flux with another arc event, again using data from the OGO 6 spacecraft. Unfortunately, they could only obtain flux measurements about 24 hours preceding and about 24 hours succeeding the observed life time of the arc. Also, there was no reported data for the period immediately preceding the time of the first appearance or for the period that immediately followed the disappearance of the arc to draw any inference concerning the relation of soft electron flux to the excitation of the arc. Recently Shepherd [1977] reported a strong flux of 20eV electrons associated with the arc on August 4, 1972. However, the detailed description of this measurement has not yet appeared in the literature.

Thus it is clear that if we were to consider the existence of coincident soft electron flux at the location of the arc itself, there exists only the case of September 28/29, 1967. But the measured flux values concurrent with the time of this arc observation are less than about 8 x 10^{7} cm^{-2} sec^{-1}. For direct excitation by precipitation in producing an arc of about 150 R, there should be a flux of 2.7 x 10^{8} cm^{-2} sec^{-1} at the topside ionosphere [Mantas and Walker, 1976], a requirement that is about three times more than what was recorded by Chandra et al. Thus the flux values detected on the night of September 28/29 are not adequate to excite the arc. In spite of

this seemingly unsuccessful correlative study, optimism has repeatedly been expressed on the role of soft electrons in the excitation of arcs [Hoch, 1973; Rees and Roble, 1975]. Indirect aeronomic effects attributed to the possible precipitation of the soft electrons [Hoch, 1973] and the availability of a sufficient amount of data from the soft electron measurements with the retarding potential analyzer aboard OGO 6 overlapping and close to the vicinity of an arc event, prompted us to make an independent investigation of the temporal and spatial build-up of soft electrons and their possible role in producing the SAR arc phenomenon.

Magnetic Activity on January 26/27, 1971

A planetary magnetic three-hourly index, K_p, was examined for the two days January 26 and 27, 1971 (Figure 10-1). It was noted that January 26 was an extremely quiet day with K_p for the day never exceeding 2_+. On the next day, K_p indices are 0_+, 5_-, 6_-, 4_+, 5_-, 5, 4, and 4. Thus the first three hours of January 27, 1971 happen to be a quiet period. During the next three hours, K_p went up to a value of 5_-.

SAR Arc of January 26/27, 1971

The geomagnetic disturbance of January 27 was found to develop at 0500 UT (Figure 10-1) as the mainphase made a negative excursion to reach a D_{st} of -46γ at 0900 UT. A small recovery phase then started at this point and lasted for about three hours, when further development of the mainphase occurred. During this small recovery phase of the storm, the presence of a stable auroral red arc was established by photometric observations made at

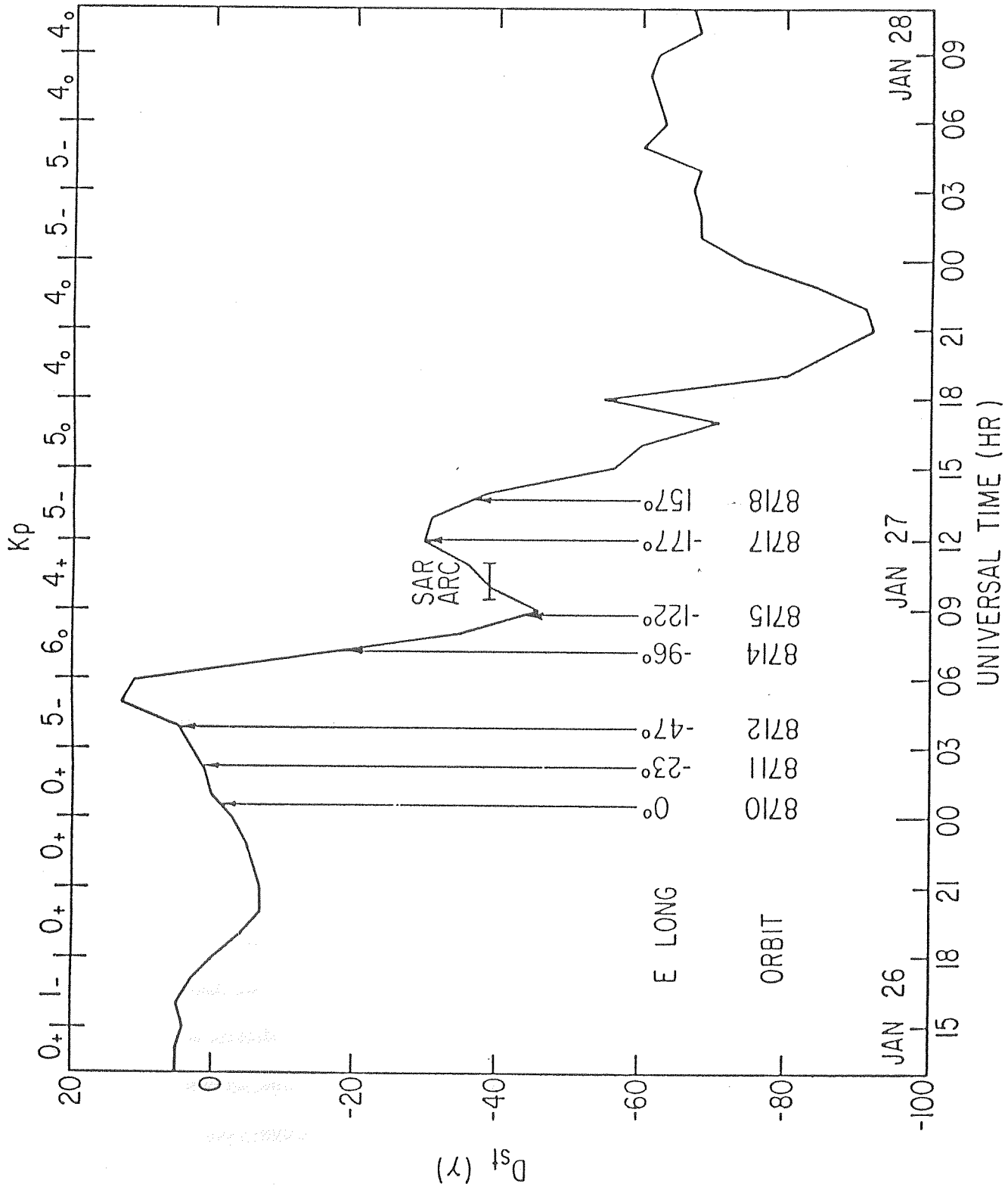

Figure 10-1 Geomagnetic storm of January 27/28, 1971

Richland, Washington (Lat. 46.4° N, Long. 119.6° W) at about 0930 UT [Hoch et al., 1973]. Subsequent observations of the arc were precluded by inclement weather. However, the initial photometric observation showed that the intensity of the arc was about 200 R. The almucanter scan made by the photometer revealed that the observed arc was approximately aligned to a fixed L shell.

When the position of the arc was mapped to an altitude of 400 km, it was found that the arc occurred between L shell intercepts 3.0 and 3.4 with a mean location at L = 3.2 at 0930 UT. The arc occurred during a period when K_p index was 4_+.

Soft Electron Flux

The OGO 6 satellite was orbiting in the altitude range 400-500 km for L values between 2 and 7 in the northern hemisphere near the time of occurrence of the arc. The satellite was south bound in polar orbit midnight with respect to local time position for the above spatial extent. A planar retarding potential analyzer [Hanson et al., 1970] on board the OGO 6 provided good measurements of integrated suprathermal electron flux of energy greater than 10eV from the series of orbits 8710-8718 on January 27, 1971. The soft electron fluxes obtained from each orbit were plotted against L value. They are shown in Figure 10-2 for orbits 8710-8715 and in Figure 10-3 for orbits 8715-8718. Universal times, local times and locations of the satellite at both ends of each profile in the figures are given in Table 10-1.

The soft electron flux data observed during the orbits 8710-8712, which are well before the occurrence of the arc, provide almost the same profiles

except for the locations of the steep gradients at lower L values (Figure 10-2). The sensitivity threshold of the instrument was about 6 x 10^{6} cm^{-2} sec^{-1}. The values did not exceed 5 x 10^{7} cm^{-2} sec^{-1} nor show any enhancement near the position of the arc. However, it is noted that the location of the steep gradient moves to smaller L values as the time proceeds. The data of orbit 8714, which was obtained about 2 hr 20 min before the birth of the arc, indicate some spike-like structures, and the flux values are much greater than 10^{8} cm^{-2} sec^{-1} above L equal to 3.7. However, the flux values in the vicinity of the position of the arc are still about 10^{7} cm^{-2} sec^{-1}.

The soft electron flux profile obtained from orbit 8715 is strikingly different from those obtained during the preceding orbits. From Figure 10-2 it can be seen that the soft electron flux exhibits three peaks occurring at L shells 4.1, 3.6, and 3.3. These peaks were obtained only 40 min before the occurrence of the arc. The southernmost peak is situated around the arc's location, and the soft electron flux value at this peak amounts to about 5.2 x 10^{8} cm^{-2} sec^{-1}. Furthermore, the longitudinal separation between the satellite and the Richland observatory at this time was only 2°. At the other two peaks, the values of flux are greater than 10^{10} cm^{-2} sec^{-1}. In spite of the fact that the fluxes are unusually high at these peaks, we do not attribute them directly to the excitation of the SAR arc. Such high flux could cause a significant enhancement of 557.7 nm emission compared to 630.0 nm emission, reflecting processes that are closely associated with the visible aurora rather than the SAR arc itself. Hoch [1973] reported

TABLE 10-1

Orbits of OGO 6 Satellite

	Orbit						
	8710	8711	8712	8714	8715	8717	8718
Universal Time	0030 0033	0210 0214	0350 0355	0708 0712	0847 0849	1200 1202	1338 1341
Local Time	2352 0019	0004 0031	0016 0043	0018 0038	0020 0030	2323 0001	2312 2357
Altitude (km)	416 435	422 453	433 491	437 481	441 459	411 425	410 423
Geographic Latitude	66.8 56.7	63.2 49.4	57.8 37.8	56.4 41.3	55.1 48.4	71.9 63.2	73.4 64.2
Geographic Longitude	-6.3 -0.2	-28.4 -22.5	-50.3 -45.0	-99.4 -95.2	-123.7 -121.6	-173.8 -177.3	146.6 157.2

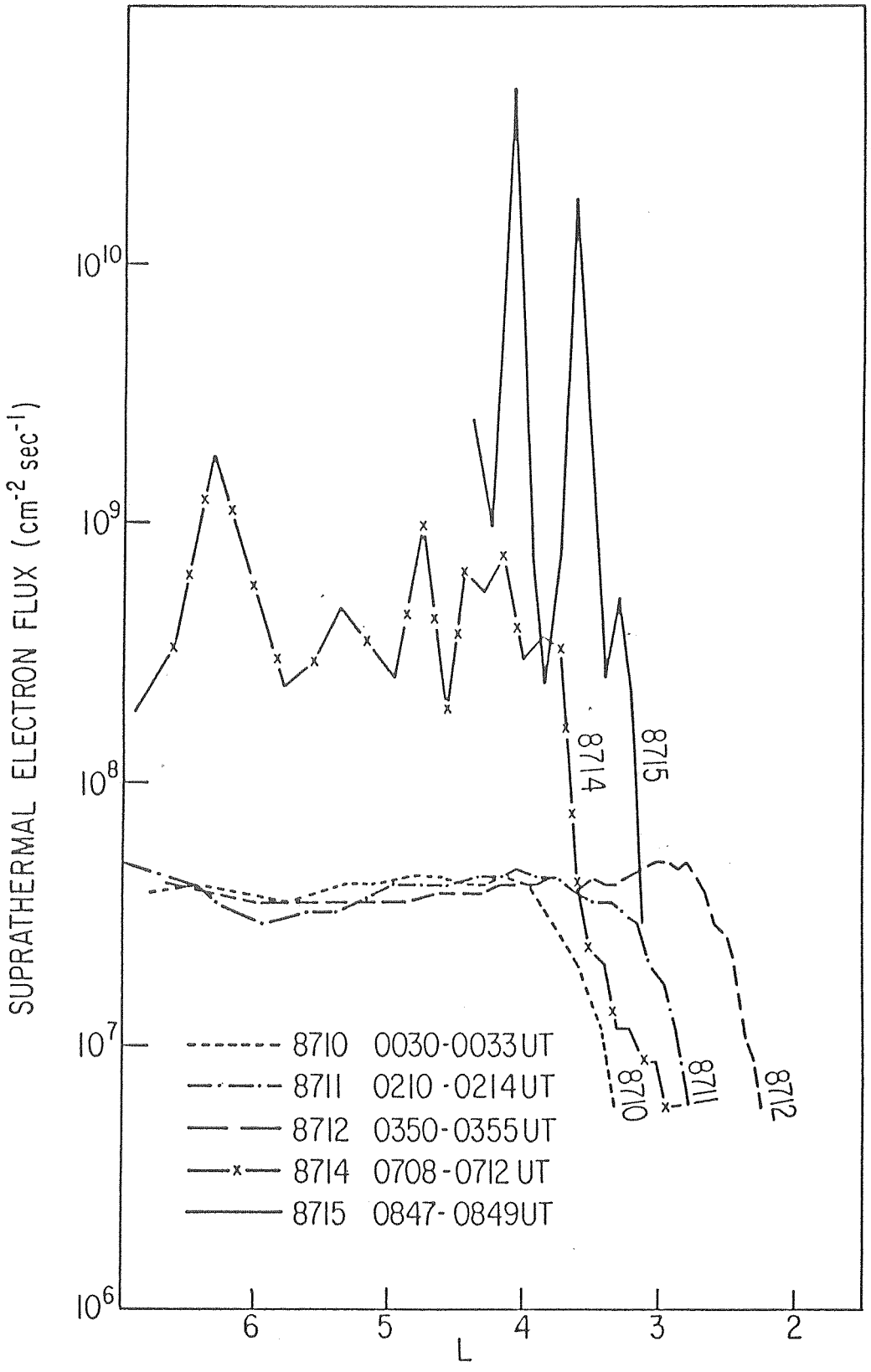

Figure 10-2 Profiles of soft electron flux obtained on orbits 8710-8715 on OGO 6 satellite on January 27, 1971.

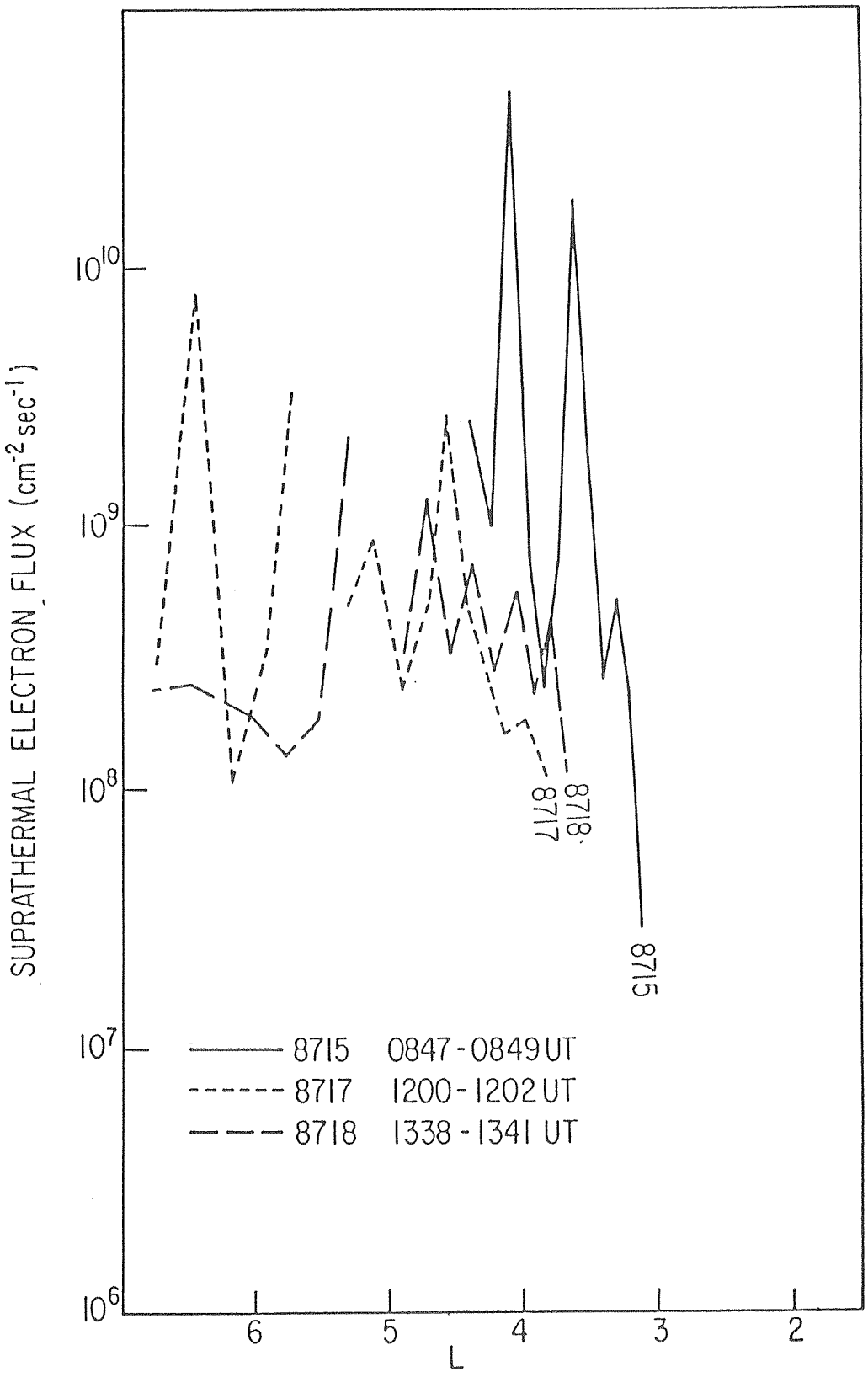

Figure 10-3 Profiles of soft electron flux obtained on orbits 8715-8718 on OGO 6 satellite on January 27, 1971.

that there had been no instance in which an arc was observed without a simultaneous poleward aurora. Also, from observations it is known that visible auroras move to mid-latitude during severe storms [Noxon and Evans, 1976]. From these considerations and from the fact that these two prominent peaks are situtated poleward of the observed location of the arc, these peaks appear to be more related to the visible aurora than to the SAR arc. On the other hand, the southernmost peak should be related to the SAR arc emissions for the following reasons: (i) the flux reaches a maximum at the L value of 3.3 which is almost the same as that of the SAR arc and at height characteristic of the arc 630.0 nm emission; (ii) the peak of the flux occurs at around 0850 UT which is within about 40 min of the arc observation itself; and (iii) the longitudinal separation between satellite measurements and ground observations is only 2°. Thus, owing to close coincidience of the arc and the soft electron flux peak, in both the temporal and the spatial sense, it is evident that the two phenomena are very likely to be related. The soft electron fluxes at the location of the arc after 1200 UT, that is 3.5 hours after the occurrence of the arc, were less than the sensitivity thrshold of the instrument (Figure 10-3).

Discussion

Soft electron fluxes (E>10eV) were measured for the consecutive orbits of OGO 6 satellite within L ranges in the vicinity of the SAR arc and for the period including the occurrence of the arc. The peak of the soft electron flux on orbit 8715 showed a strong relation to the arc in the sense of both space and time.

According to Mantas and Walker [1961], a soft electron flux of 1.8×10^8 $cm^{-2}sec^{-1}$ precipitating into the topside ionosphere (1000 km) can excite an arc of 100 R. They noted that the flux needed is almost independent of the energies of soft electrons ranging from 25 to 100 eV, and that the flux produces 1_D and 1_S oxygen atoms in a ratio of about 14 to 1 without considering the contribution of the energy to the arc from "hot" thermal electrons themselves. Provided that the intensity of an arc is proportional to the flux of soft electrons, a flux of 3.6×10^8 cm^{-2} sec^{-1} at the topside ionosphere is required to produce the observed intensity of the arc. Also Rees and Roble [1975] give the number of quanta of 630.0 nm emission per incident electron of specified energy. Considering the fact that collisional quenching of the excited state is not important above the altitude of the arc, their results show that a flux between 1.87×10^8 $cm^{-2}sec^{-1}$ and 1.75×10^8 $cm^{-2}sec^{-1}$ at the topside ionosphere, corresponding to electron energies of 30eV and 50eV respectively, is required to excite the observed intensity of the arc. The observed peak value of the soft electron flux, which should be related to the arc, was 5.2×10^8 cm^{-2} sec^{-1}, and this value was measured at the altitude of 457 km. The soft electron flux at the topside ionosphere may be greater than the values measured at lower altitude. Thus, the observed soft electron flux is more than adequate to meet the energy requirements for the excitation of the arc. Therefore, based on the above qualitative consideration along with the spatial structure and temporal development of

the observed soft electron flux, the soft electrons are most likely contributors to the excitation of the arc on January 27, 1971.

Thus, for the first time, observational support has been provided to the soft electron hypothesis in initiating an SAR arc. However, questions still remain as to whether or not the soft electron fluxes are able to sustain the arc for a prolonged period.

CHAPTER XI

Summary and Conclusions

Those items of this investigation that are significant are summarized in the following:

1. A 15-cm Fabry-Perot interferometer which utilizes a multiple zone aperture (MZA, with ten zones besides a central hole) was constructed and satisfactorily applied to the measurements of thermospheric temperatures. The measurements were largely helped by the gain of throughput due to the use of an MZA as shown in Chapter 2.
2. It was found also in Chapter 2 that there is a definite optimum aperture width for a certain combination of instrumental parameters in the measurements of temperatures of the upper atmosphere. An analytical method was presented to find an optimum aperture width which is unexpectedly large compared with those used previously by other workers.
3. It was established in Chapter 3 that the temperatures obtained from Doppler profile measurements of [OI] 630.0 nm nightglow emission during geomagnetically quiet periods are consistent within the range of experimental errors with the exospheric temperatures calculated from the MSIS model, which is primarily a magnetically quiet model.
4. Thermospheric temperature response to an isolated substorm was clarified in Chapter 4 from simultaneous measurements of the temperatures and concurrent auroral electrojet activities inferred

from geomagnetic records obtained from stations along a meridian close to the observation site of optical measurements.

5. From the temperatures measured during five geomagnetically disturbed periods and the longitudinal locations of the maximum intensity of an auroral electrojet (AEJ) inferred from the data of AE indices, it was shown in Chapter 5 that; (i) when the most intense portion of the westward AEJ is located at Great Whale River (GWC), which is in close proximity to the Albany meridian, observed temperature enhancement is large even if the intensity of the AEJ is moderate; and that (ii) when the most intense portion of the westward AEJ is located Narssarssuaq (NAQ) or Leirvogur (LRV), which is far away from the Albany meridian, the required intensity of AEJ to produce similar temperature enhancement, as in the previous case, is much larger. It is also noted that there is a definite time lag of an order of one hour between the intensification of AEJ and the temperature rise. Temperatures measured in the middle of aurora did not show a significant enhancement, indicating that heating due to particle precipitation is not as effective as the Joule heating.

6. It was shown in Chapter 6 that the [OI] 630.0 nm profiles observed around 0700 UT on July 5, 1978, which showed the most increased "apparent temperatures", could not be interpreted in terms of a single Gaussian source profile. Instead, a combination of two Gaussian source profiles satisfactorily explained the observed results. This, together with unusually high intensity at

the time of the observation, suggests that the [OI] 630.0 nm emission consisted of two different components, each being originated from a different source. A strong possibility is the precipitation of energetic O^+ ions, whose aeronomical effects were predicted by Torr et al. [1982] and seem to explain the observed results.

7. It was shown in Chapter 7 that the temperatures within a SAR arc which appeared on the night of September 25/26, 1978 (EST) showed an increase of about 200° K at around 2.7 hours after the appearance of the arc, while no other enhancement of the temperature was observed during the observation period.

8. In Chapter 8, the photometric observations of the SAR arc on the night of September 25/26, 1978 (EST) were compared with the concurrent ground-based magnetometer observations of the auroral electrojets. Results of the combined observations reveal that there is a close relationship of the arc to the concurrent electrojets. Specifically, it was found that; (i) at the beginning of the arc's appearance near local midnight, the position of the intercept point of the magnetic field line threading the arc at auroral height coincided with the eastward auroral electrojet center; (ii) the intensity variation of the arc followed closely that of the westward electrojet, with a time lag of 10-20 minutes after the arc reached its peak intensity; and (iii) the arc showed equatorward movement in general, however, during the periods when

the electrojet moved rapidly for a great distance, the arc also moved in the same direction but to a lesser degree.

9. Results of the two-station observation of a weak but well defined SAR arc on the night of September 26/27, 1979 (EST) were presented in Chapter 9. Triangulation from the two stations showed that the arc moved rapidly equatorward and downward during the period of steep increase of intensity. Magnetograms obtained from stations over Canada showed striking coincidence of the onset of the arc and that of an isolated substorm, suggesting some physical link between the two phenomena.

10. An examination of OGO 6 measurements of soft electron flux, which is almost concurrent with a SAR arc, was made in Chapter 10. In the case considered, the precipitation of the soft electron flux peaks at about the same location and time of occurrence as the SAR arc. The peak value is found to be 5.2×10^{8} cm^{-2} sec^{-1}, which is more than adequate to excite the observed arc.

In summary, this dissertation provides new observational results of the thermospheric temperature response to three types of magnetosphere-thermosphere energy coupling; Joule dissipation of electric fields, precipitation of energetic O^{+} ions, and the SAR arc. A new finding on the relationship of the SAR arcs to the auroral electrojet associated with substorms is also presented.

It seems now pertinent to discuss future directions in the line of this investigation to deepen our understanding of the relevent physics.

It is apparent from the results presented in this dissertation that the thermosphere clearly responds to the auroral electrojet activity through Joule heating. The behavior of the response has been clarified quantitatively to a considerable extent. Nevertheless, more comprehensive measurements appear to be desired. Measurements of electric fields, E and the Pedersen conductivity, σ_p in the ionosphere will make it possible to estimate the Joule heating rate Q_J through the relation $Q_J = \int \sigma_p E^2 dz$. This can be done with an incoherent scatter radar from the ground [e.g., Vickrey et al., 1982]. Therefore, coordinated observations by optical means and incoherent scatter radar will greatly advance the phenomenology. Due to the spatial structure of auroral particle precipitation, the Joule heating is also expected to have considerable small-scale structure. The results presented in Chapter 5 also suggest the localization of the Joule heating. In order to clarify the horizontal structure of the Joule heating effect, an instrument which is able to measure the two-dimensional field of both the temperature and wind of the thermosphere will be most helpful. Realization of such a concept has recently been reported by Rees et al. [1984] and Shepherd et al. [1984]. The instrument used by Rees et al. [1984] is a Doppler imaging system; a field widened Fabry-Perot interferometer which can simultaneously image a number of Fabry-Perot fringes using an imaging photon detector. Shepherd et al. [1984] reported the first results of measurements made with a Wide Angle Michelson Doppler Imaging Interferometer which utilizes a CCD (Charge Coupled Device) detector to map a two-dimensional image of the sky. Although the results of these two recent works are very preliminary, the concepts of the

instruments appear very promising. A network of optical stations at mid- and high latitudes and subsequent coordinated observations are also necessary to obtain a comprehensive view of the thermospheric response to a localized energy input.

From the theoretical side, a model which properly incorporates the various high-latitude processes which are highly structured both in space and time, such as the Joule heating, the heating by precipitating charged particles, and the momentum source due to ion drag associated with magnetospheric convection is urgently needed. Such a model has to be time-dependent since the variations of neutral composition due to the heating and the changes in ionospheric conductivities due to the ionization arising from the particle precipitation need to be taken into account. The most recent and sophisticated model along this line has been presented by Fuller-Rowell [1984], though it is two-dimensional.

The [OI] 630.0 nm line profiles which could not be interpreted in terms of a single Gaussian source profile, and an unusually large temperature enhancement were described in Chapter 6. These observational results are quite unique and have not been reported previously. The only possibility that can explain the observed results at present appear to be the precipitation of energetic O^+ ions, as predicted by Torr et al. [1982]. However, experimental confirmation of the aeronomical effects due to the precipitation of energetic O^+ ions will have to wait coordinated observations of such fluxes from satellites and of the thermospheric response from the ground. Also for the purpose of these ground-based optical

observations, a network of stations equipped with an imaging interferometer system like that mentioned above is desirable.

Observational results on the SAR arcs presented in this investigation lend to several new aspects which are difficult to explain properly in the context of the heat conduction as a formation mechanism. They include the enhancement of neutral gas temperature as high as $\sim 200^{\circ}$ K within an arc (Chapter 7), close correlation between the intensity of an arc and that of the westward auroral electrojet (Chapter 8), a remarkable coincidence of the onset of an arc and that of an isolated substorm (Chapter 9), and the soft electron flux measurements concurrent with an arc (Chapter 10). We will have to wait until the next solar maximum in which a more detailed analysis of a large ensemble of events should enable us to obtain a more complete understanding as to the formation mechanism of the SAR arc.

Bibliography

Appleton, E.V., and L. J. Inigram, Magnetic storms and upper-atmospheric ionization, Nature, 136, 548-549, 1935.

Barbier, D., The auroral activity at low latitudes, Ann. Geophys. 14, 334-355 1958.

Biondi, M.A., D.P. Sipler, and M. Weienschenker, Multiple aperture exit plate for field-widening a Fabry-Perot interferometer, Appl. Opt., 24, 232-236, 1985.

Carman, E.H., M.P. Heeran, and N.J. Skinner, SAR arc and 6300 Å emission by dissociative recombination of O_2^+ observed from Africa during severe magnetic storms, Planet. Space Sci. 24, 629-641, 1976.

Carpenter, D.L., Ogo 2 and 4 VLF observations of the asymmetric plasmapause near the time of SAR arc events, J. Geophys. Res. 76, 3644-3650, 1971.

Chabbal, R., Recherche des meilleurs conditions d'utilization d'un spectromètre photoeléctrique Fabry-Perot, J. Rech. Centre Nat. Rech. Sci., 24, 138-186, 1953.

Chandra, S., E.J. Maier, B.E. Troy, Jr., and B.C. Narasinga Rao, Subauroral red arcs and associated ionspheric phenomena, J. Geophys. Res. 76, 920-925, 1971.

Chapman, S., The heating of the ionosphere by the electric currents associated with geomagnetic variations, Terr. Magn. Atmos. Elec., 42, 355-358, 1937.

Cole, K.D., Stable auroral red arcs, sinks for energy of Dst main phase, J. Geophys. Res., 70, 1689-1706, 1965.

Cole, K.D., Electrodynamic heating and movement of the thermosphere, Planet. Space Sci., 19, 59-75, 1971.

Cornwall, J.M., F.V. Coroniti, and R.M. Thorne, Unified theory of SAR arc formation at the plasmapause, J. Geophys. Res., 76, 4428-4445, 1971.

Craven, J.D., L.A. Frank, and K. L. Ackerson, Global observations of a SAR arc, Geophys. Res. Lett., 9, 961-964, 1982.

Dalgarno, A., Corpuscular radiation in the upper atmosphere, Ann. Geophys. 20, 65-74, 1964.

Fuller-Rowell, T.J., A two-dimensional, high-resolution, nested-grid model of the thermosphere 1. Neutral response to an electric field "spike", J. Geophy. Res., 89, 2971-2990, 1984.

Greer, R.G.H., and G.T. Best, A rocket-borne photometric investigation of the oxygen lines at 5577Å and 6300Å, the sodium D-lines and the continuum at 5300Å in the night airglow, Planet. Space Sci., 15, 1857-1881, 1967.

Gurgiolo, C., D.W. Slater, J.D. Winningham, and J. L. Burch, Observation of a heated electron population associated with the 6300Å SAR arc emission Geophys. Res. Lett., 9, 965-968, 1982.

Hanson, W.B., S. Sanatani, D. Zuccaro, and T.W. Flowerday, Plasma measurements with the retarding potential analyzer on OGO 6, J. Geophys. Res. 75, 5483-5501, 1970.

Hasegawa, A., and K. Mima, Anomalous transport produced by kinetic Alfvén wave turbulence, J. Geophys. Res., 83, 1117-1123, 1978.

Hays, P.B., and R.G. Roble, A technique for recovering Doppler line profiles from Fabry-Perot interferometer fringes of very low intensity, Appl. Opt., 10, 193-200, 1971.

Hays, P.B., A.F. Nagy, and R.G. Roble, Interferometric measurements of the 6300 Å Doppler temperature during a magnetic storm, J. Geophys. Res. 74, 4162-4168, 1969.

Hays, P.B., A.F. Nagy, K.D. McWatters, and J.V. Evans, Comparison of radar and optical temperature measurements in the F region, J. Geophys. Res., 75, 4881-4882, 1970.

Hedin, A.E., J.E. Salah, J.V. Evans, C.A. Reber, G.P. Newton, N.W. Spencer, D.C. Kayser, D. Alcaydé, P. Bauer, L.C. Cogger, and J.P. McClure, A global thermospheric model based on mass spectrometer and incoherent scatter data; MSIS 1, N_2 density and temperature, J. Geophys. Res., 82, 2139-2147, 1977.

Heikkila, W.J., Electric field topology near the dayside magnetopause. J. Geophys. Res. 83, 1071-1078, 1978.

Hernandez, G., Analytical description of a Fabry-Perot photoelectric spectrometer, Appl. Opt., 5, 1745-1748, 1966.

Hernandez, G., Spectroscopic studies of the arc of March 8-9, 1970, Planet. Space Sci. 20, 1309-1321, 1972.

Hernandez, G., Contamination of the OI($^3P_2$-$^1D_2$) emission line by the (9-3) band of OH X ^{2}II in high resolution measurements of the night sky, J. Geophys. Res., 79, 1119-1123, 1974a.

Hernandez, G., Analytical description of a Fabry-Perot spectrometer. 3: Off-axis behavior and interference filters, Appl. Opt., 13, 2654-2661, 1974b.

Hernandez, G., and R.G. Roble, Observations of large scale thermospheric waves during geomagnetic storms, J. Geophys. Res., 83, 5531-5538, 1978.

Hernandez, G., and R.G. Roble, Thermospheric dynamics investigations with very high resolution spectrometers, Appl. Opt., 18, 3376-3385, 1979.

Hernandez, G., T.E. Van Zandt, V.L. Peterson, and J. P. Turtle, Comparison of optical and incoherent scatter measurements of nighttime exospheric temperature at magnetic equator, J. Geophys. Res., 80, 3271-3274, 1975.

Hoch, R.J., Stable auroral red arcs, Rev. Geophys. Space Phys. 11, 935-949, 1973.

Hoch, R.J. and L.L. Smith, Location in the magnetosphere of field lines leading to the SAR arcs, J. Geophys. Res. 76, 3079-3086, 1971.

Hoch, R.J., L.L. Smith, and R.W. Owen, Occasions of SAR arc observations at the Battelle observatory near Richland, Washington, J. Geophys. Res., 78, 7558-7559, 1973.

Horwitz, J.L., W.K. Cobb, C.R. Baugher, C.R. Chappell, L.A. Frank, T.E. Eastman, R.R. Anderson, E.G. Shelley, and D.T. Young, On the relationship of the plasmapause to the equatorward boundry of the auroral oval and to the inner edge of the plasma sheet. J. Geophys. Res. 87, 9059-9069, 1982.

Ichikawa, T. and J. S. Kim, Observations of M arc at Moscow, Idaho, U.S.A., J. Atmos. Terr. Phys. 31, 547-553, 1969.

Ichikawa, T., T. Old, and J.S. Kim, Relationship between a monochromatic auroral arc of 6300 Å and a visible aurora. J. Geophys. Res. 74, 5819-5821, 1969.

Jacchia, L.G., Corpuscular radiation and the acceleration of artifical satellites, Nature, 183, 1662-1663, 1959.

Kamei, T. and H. Maeda, World Data Center C2 for Geomagnetism, Data Book No. 4, Auroral Electrojet Indices (AE) for July-December, 1978, Kyoto Univ., Japan, 1981.

Kamide, Y., F. Yasuhara, and S.-I. Akasofu, A model current system for the magnetospheric substorm, Planet. Space Sci., 24, 215-222, 1976.

Kamide, Y., R.M. Robinson, S. -I. Akasofu, and T.A. Potemra, Aurora and electrojet configuration in the early morning sector. J. Geophys. Res. 89, 389-393, 1984.

Kirby, S.S., T.R. Gilliland, E.B. Judson, and N. Smith, The ionsphere, Sunspots, and magnetic storms, Phys Rev., 48, 849, 1935.

Kisabeth, J.L., and G. Rostoker, Development of the polar electrojet during polar magnetic substorms, J. Geophys. Res., 76, 6815-6828, 1971.

Mantas, G.P. and J.C.G. Walker, The penetration of soft electrons into the ionosphere, Planet. Space Sci. 24, 409-423, 1976.

Marovich, E., and F.E. Roach, Distribution of latitude of red arcs, J. Geophys. Res., 68, 1885-1888, 1963.

Meaburn, J., Scanning Fabry-Perot interferometers for nebular studies, Astrophys. Space Sci., 2, 115-127, 1968.

Meng, C.-I, R.H. Holzworth, and S. -I. Akasofu, Auroral circle-delineating the poleward boundary of the quiet auroral belt. J. Geophys. Res. 82, 164-172, 1977.

Moore, T.E., R.L. Arnoldy, J. Feynman, and D.A. Hardy, Propagating substorm injection fronts. J. Geophys. Res. 86, 6713-6726, 1981.

Nagy, A.F., R.G. Roble, and P.B. Hays, Stable mid-latitude red arcs: observations and theory, Space Sci. Rev., 11, 709-727, 1970.

Nagy, A.F., W.B. Hanson, R.J. Hoch and T.L. Aggson, Satellite and ground-based observations of a red arc, J. Geophys. Res. 77, 3613-3617, 1972.

Nagy, A.F., L.H. Brace, N.C. Maynard and W.B. Hanson, Is the red arc a good indicator of ionosphere-magnetosphere conditions? J. Geophys. Res. 79, 4331-4333, 1974.

Noxon, J.F. and J.V. Evans, Simultaneous optical and incoherent scatter observations of two low-latitude auroras, Planet. Space Scie. 24, 425-442, 1976.

Okano, S., J.S. Kim, and T. Ichikawa, Measurements of thermospheric response to auroral activities, Planet. Space Sci., 33, 841-845, 1985.

Old, T.E., M. Okuda, and J.S. Kim, Observation of an unusual multiple mid-latitude 6300 Å (OI) arc from two ground stations, Ann. Geophys. 28, 863-869, 1972.

Petersen, H., Über die Temperatur in den höheren Schichten der Atmosphäre, Z. Phys., 28, 510-513, 1927.

Prasad, J.S., T.E. Old, and J.S. Kim, The relation of a mid-latitude 6300 Å arc to substorm associated phenomena. Ann. Geophys. 31, 361-367, 1975.

Rees, D., A.H. Greenaway, R. Gordon, I. McWhirter, P.J. Charleton and Åke Steen, The Doppler imaging system: initial observations of the auroral thermosphere, Planet. Space Sci., 32, 273-285, 1984.

Rees, M.H., and S. -I. Akasofu, On the association between subvisual red arcs and the Dst (H) decrease, Planet. Space Sci., 11, 105-107, 1963.

Rees, M.H., and R.G. Roble, Observations and theory of the formation of stable auroral rec arcs, Rev. Geophys. Space Phys., 13, 201-242, 1975.

Roach, F.E. and J.R. Roach, Stable 6300 Å auroral arcs in mid-latitudes, Planet. Space Sci., 11, 523-545, 1963.

Roble, R.G., Dynamics of the earth's thermosphere, Rev. Geophys. Space Sci., 21, 217-233, 1983.

Roble, R.G., and R.E. Dickinson, Is there enough solar extreme ultraviolet radiation to maintain the global mean thermospheric temperature?, J. Geophys. Res., 78, 249-257, 1973.

Roble, R.G., P.B. Hays, and A. F. Nagy, Calculated [OI] 6300 Å nightglow Doppler temperatures for solar cycle minimum, Planet. Space Sci., 16, 1109-1113, 1968.

Sharp, R.D., R.G. Johnson, E.G. Shelley, and K.K. Harris, Energetic O^+ ions in the magnetosphere, J. Geophys Res., 79, 1844-1850, 1974.

Sharp, R.D., R.G. Johnson, and E.G. Shelley, The morphology of energetic O^+ ions during two magnetic storms: temporal variations, J. Geophys Res., 81, 3283-3291, 1976a.

Sharp, R.D., R.G. Johnson, and E.G. Shelley, The morphology of energetic O^+ ions during two magnetic storms: latitudinal variations, J. Geophys. Res., 81, 3292-3298, 1976b.

Shelley, E.G., R.G. Johnson, and R.D. Sharp, Satellite observations of energetic heavy ions during a geomagnetic storm, J. Geophys Res., 77, 6104-6110, 1972.

Shelley, E.G., R.G. Johnson, and R.D. Sharp, Morphology of energetic O^+ in the magnetosphere, in Magnetospheric Physics, pp. 135-139, D. Reidel, Higham, Mass., 1974.

Shepherd, G.G., Asymmetrical SAR arc event observed August 4, 1972 from ISIS-II, EOS, Trans. Am. Geophys., 58, 481, 1977.

Shepherd, G.G. W.A. Gault, R.A. Koehler, J.C. McConnell, K.V. Paulson, E.J. Llewellyn, C.D. Anger, L.L. Cogger, J.W. Haslett, D.R. Moorcroft, and R.L. Gattinger, Optical Doppler imaging of the aurora borealis, Geophys. Res. Lett., 11, 1003-1006, 1984.

Slater, D.W., and L.L. Smith, Modulation of stable auroral red (SAR) arc occurrence rates, J. Geophys. Res., 86, 3669-3673, 1981.

Smith, P.H., R.J. Hoch, R.W. Owen, G. Hernandez, and E. Marovich, Altitude of the λ6300-Å, λ5577-Å, and λ4278-Å emissions of the stable auroral red arcs of March 8-9, 1970, J. Geophys. Res., 77, 2987-2996, 1972.

Tohmatsu, T., and F.E. Roach, Morphology of mid-latitude 6300Å arcs, J. Geophys. Res., 67, 1817-1821, 1962.

Torr, M.R., J.C.G. Walker, and D.G. Torr, Escape of fast oxygen from the atmosphere during geomagnetic storms, J. Geophys. Res., 79, 5267-5271, 1974.

Torr, M.R., and D.G. Torr, Energetic oxygen: a direct coupling mechanism between the magnetosphere and thermosphere, Geophys. Res. Lett., 6, 700-702, 1979.

Torr, M.R., D.G. Torr, and P.G. Richards, The solar ultraviolet heating efficiency of the midlatitude thermosphere, Geophys. Res. Lett., 7, 373-376, 1980a.

Torr, M.R. P.G. Richards, and D.G. Torr, A new determination of the ultraviolet heating efficiency of the thermosphere, J. Geophys. Res., 85, 6819-6826, 1980b.

Torr, M.R., D.G. Torr, R.G. Roble, and E.C. Ridley, The dynamic Response of the thermosphere to the energy influx resulting from energetic O^+ ions, J. Geophys. Res., 87, 5290-5300, 1982.

Vickrey, J.F., R.R. Vondrak, and S.J. Matthews, Energy deposition by precipitating particles and Joule dissipation in the auroral ionsphere, J. Geophys. Res., 87, 5184-5196, 1982.

Yee, J.H., J.W. Meriwether, Jr., and P.B. Hays, Detection of a corona of fast oxygen atoms during solar maximum, J. Geophys. Res., 85, 3396-3400, 1980.